GLOBAL QUANTIFICATION OF LIGHTNING-INDUCED ELECTRON PRECIPITATION USING VERY LOW FREQUENCY REMOTE SENSING

A DISSERTATION

SUBMITTED TO THE DEPARTMENT OF ELECTRICAL ENGINEERING

AND THE COMMITTEE ON GRADUATE STUDIES

OF STANFORD UNIVERSITY

IN PARTIAL FULFILLMENT OF THE REQUIREMENTS

FOR THE DEGREE OF
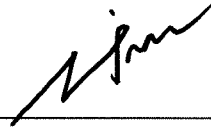
DOCTOR OF PHILOSOPHY

Benjamin R. T. Cotts

March 2011

This dissertation is online at: http://purl.stanford.edu/sv520xc1020

I certify that I have read this dissertation and that, in my opinion, it is fully adequate in scope and quality as a dissertation for the degree of Doctor of Philosophy.
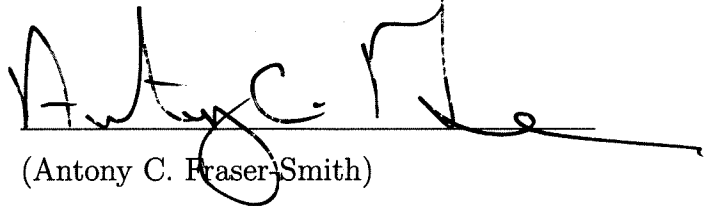
_____

(Umran S. Inan)   Principal Adviser

I certify that I have read this dissertation and that, in my opinion, it is fully adequate in scope and quality as a dissertation for the degree of Doctor of Philosophy.

_____

(Nikolai G. Lehtinen)

I certify that I have read this dissertation and that, in my opinion, it is fully adequate in scope and quality as a dissertation for the degree of Doctor of Philosophy.

_____

(Antony C. Fraser-Smith)

Approved for the University Committee on Graduate Studies

_____

iii

This dissertation is dedicated to my mother and father

Abstract

Observations of lightning-induced electron precipitation (LEP) events at three geographic regions show characteristics which systematically vary with both longitude and hemisphere. These observations are quantitatively interpreted with the use of a novel model of atmospheric backscatter designed to be used to predict the characteristics of LEP events at any longitude and mid-latitude L-shell by accounting for the effects of precipitating electrons which are backscattered from the atmosphere.

The new model of atmospheric backscatter (ABS) is based upon the calculation of ~16,000 individual atmospheric backscatter responses for monoenergetic, monodirectional electron beams with a single incident pitch angle using a Monte Carlo model of atmospheric interactions. The model tracks the full gyration of each individual precipitating electron around the magnetic field line as it enters the atmosphere, accounting for the dynamic friction force and angular diffusion as well as the production of new electrons via ionization. The ABS model includes the effects of the asymmetric magnetic field in calculations of the pitch angle of backscattered electrons entering the conjugate hemisphere and accounts for the different strength of the magnetic field at conjugate points of the same field line. This magnetic field difference causes the equatorial loss cone angle to vary greatly between hemispheres and with longitude, which results in significant and systematic differences in LEP signatures at various locations.

A realistic distribution of precipitating electrons is inserted into the ABS model by calculating the energy and pitch angle distribution, which results from the resonant interactions of a lightning-initiated magnetospherically reflecting whistler wave with trapped radiation belt particles. This calculation is accomplished by extensive

magnetospheric ray-tracing, accounting for Landau damping as well as spatial and temporal dispersion of the whistler wave.

This distribution of precipitating electrons is then inserted into the ABS model at three separate longitudes ($\varphi_1^{\mathbf{N}}$=260° **E/N**, $\varphi_2^{\mathbf{N}}$=290° **E/N**, and $\varphi_1^{\mathbf{S}}$=295° **E/S**, corresponding to the Central United States, the East Coast of the United States, and Palmer, Antarctica, respectively) and the deposition results are compared with VLF remote sensing data collected on nearly north-south great circle paths (GCPs) allowing for isolation of longitudinal effects on LEP. Results predicted by the model and confirmed by data indicate that all four primary LEP characteristics exhibit longitudinal and hemispheric dependencies which can be explained in terms of backscatter of precipitating electrons from the atmosphere. The mean observed LEP onset delay (Δt) exhibits a hemispheric dependence at these longitudes with events in the northern hemisphere delayed by one bounce period relative to direct precipitation and advanced by one-half bounce period in the southern hemisphere. The mean observed onset duration (t_{d}) exhibits a longitudinal dependence with events observed at $\varphi_1^{\mathbf{N}}$ and $\varphi_2^{\mathbf{S}}$ persisting for three bounce periods, and at $\varphi_2^{\mathbf{N}}$ for two bounce periods. The amplitude change (ΔA) and recovery time (t_{r}) also show a longitudinal and hemispheric dependence based upon the relative sizes of the loss cones at different longitudes. LEP events produced at $\varphi_1^{\mathbf{N}}$ have consistently larger perturbation magnitudes than at $\varphi_2^{\mathbf{N}}$, and observed recovery times at $\varphi_2^{\mathbf{N}}$ are longer than at $\varphi_1^{\mathbf{N}}$ which are still longer than at $\varphi_2^{\mathbf{S}}$. All of these results are explained in terms of backscatter of precipitating electrons from the atmosphere and the ABS model shows that by accounting for atmospheric backscatter it is possible to accurately predict all the observable characteristics of LEP events. Furthermore, by combining these effects with previously calculated radiation belt electron loss rates due to lightning at a single location, it is possible to estimate the global loss of radiation belt electrons due to lightning.

Acknowledgments

As my time at Stanford comes to an end and I complete the final pages of this dissertation I cannot help but reflect on all those who have helped me on this winding road to a Ph.D. Without support from so many people I would never have gotten to where I am today.

First I would like to thank my principle adviser, Dr. Umran Inan for letting me be a part of so many interesting projects and for all he has taught me during my time at Stanford. His unparalleled drive and enthusiasm for VLF is truly inspiring and I am grateful for all his support through the years. Thanks to Umran I have traveled to more interesting, beautiful and remote places than I could ever have imagined.

Next I would like to thank my second adviser, Dr. Nikolai Lehtinen, first for the Monte Carlo code upon which my work is based but more for the countless discussions, support and technical expertise he has given me during the most critical portions of my research. Nikolai's clarity of thought and willingness to help have made this research and dissertation significantly more rigorous, accurate and complete.

I would also like to thank Dr. Antony Fraser-Smith for reading this thesis in addition to all the enlightening, amusing and interesting discussions we have had over the years. Thanks also to Dr. John Gill III for agreeing to chair my defense committee. Additionally, I would like to acknowledge the generous help of Professors Martin Walt and Don Carpenter as well as that from Drs. Dave Lauben and Maria Spasojevic throughout my research.

The data in this work came from the HAIL array and I would like to thank the many hosts of our sites, including Dr. Joseph Sabutis, Manuel Lujan, Naomi Salaman, Paul Fechtmeister, Paul Anderson, Mike Lathrop, Jonathan Friedman, Raul Garcia

To my Dad and Terri: you have always been there for me and I cannot thank you enough for the love, life perspectives, hikes, camping trips, games and of course the turkey. To my mother: you are the kindest and most selfless and loving person I have ever known and it is impossible to overstate how much your love and support mean to me. Finally, to my beautiful and loving wife Claudia: thank you for your endless patience and steadfast love throughout this process. Du bist mein Engel und ich bin über beide Ohren in dich verliebt.

BENJAMIN R. T. COTTS

Stanford, California
March 11, 2011

Contents

List of Tables

List of Figures

xv

Chapter 1

Introduction

During the now infamous "Halloween Storm" of 2003 the near-earth space environment came under the most devastating solar effects in recorded history as the Sun hurled eleven X-class solar flares and three huge coronal mass ejections towards Earth. At the worst point one satellite failed entirely and more than 28 others were forced to temporarily cease operation, including most satellites whose specific purpose was to observe solar storms. Astronauts on the International Space Station had to retreat inside the heavily shielded storage module, the Federal Aviation Administration issued the first ever high radiation dosage alert for high-altitude aircraft, rerouting plane routes north of 57 degrees latitude, and a massive power failure blacked out much of the country of Sweden [*Webb and Allen*, 2004]. For nearly two weeks the flood of high energy electron radiation continued to wreak havoc on space-borne assets, compressing the Earth's geomagnetic field and shifting the location of the outer radiation belt to only ~10,000 km from the surface of the earth [*Baker et al.*, 2004].

Much of the attention the radiation belts have received is due to the devastating effects of this radiation on satellite electronics (especially over time) and because satellites are particularly vulnerable during periods of extreme geomagnetic activity (such as the Halloween storm) means that understanding the time-frame and mechanisms for removal of this radiation is increasingly important as the reliance on space-borne assets continues to rise.

The goal of this dissertation is to quantitatively investigate the global role of lightning in the removal of energetic radiation belt electrons using ionospheric remote sensing to detect the electrons as they are removed from the radiation belts. This approach requires understanding of both the ionosphere and magnetosphere, including electromagnetic wave propagation in collisional and collisionless plasmas, magnetospheric energetic particle motions, ionospheric ionization due to the impact of energetic particles and the scattering of waves due to the resultant ionospheric conductivity enhancements.

1.1 Scientific Background

1.1.1 The Ionosphere

The 'ionosphere' is a region of the atmosphere where a sufficient number of particles are ionized to form a collisional plasma. Beginning at ∼50 km altitude and extending several hundred kilometers above Earth, the ionosphere is so-named because the physical interactions within this region are dominated by the movement of free electrons and ions.

The ionosphere is formed because at these altitudes air is thin enough that the rate of ionization due to external sources in the atmosphere is faster than the rates of recombination. During the day the Sun provides sufficient radiation to photo-ionize significant portions of the atmosphere (down to ∼50–70 km altitude) while at night the ionizing effect of cosmic radiation maintains a somewhat depleted ionosphere (significantly less ionization) with the base of the ionosphere appearing at ∼80–85 km. In addition to the diurnal variation of the ionosphere, the ionosphere can also vary significantly with solar activity, season (primarily linked to the solar zenith angle [e.g., *Tascione*, 1988, Chapter 7]) and geographic latitude. Mid-latitude regions tend to exhibit the least amount of variation while high-latitudes are coupled to the magnetospheric tail (and hence linked to solar-driven geomagnetic activity) and low-latitudes are affected by the equatorial ring current and plasma instabilities [e.g., *Tascione*, 1988, Chapter 8].
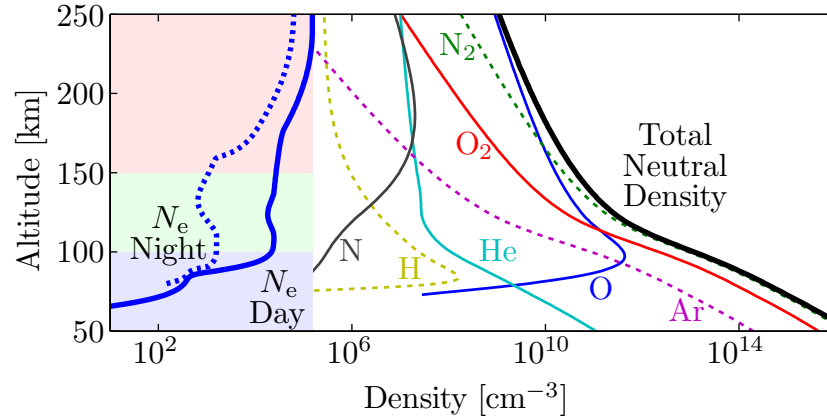
Figure 1.1: Neutral atmospheric constituents and electron density profiles with approximate location of D-, E-, and F-regions. (MSIS-E-90 Atmospheric Model and IRI-2007 Model profiles are available at http://omniweb.gsfc.nasa.gov/vitmo/).

As shown by the colored portions in Figure 1.1, the ionosphere is horizontally stratified into layers due to the different absorptive characteristics of neutral molecules at varying altitudes and because the density (as well as composition) of the atmosphere changes with height [*Tascione*, 1988, Ch. 7]. The exponentially-decreasing density of the neutral atmosphere leads to varying states of equilibrium between rates of ionization and recombination. The specific layers of the ionosphere progress upwards in altitude from 60-100 km (D-region), 100-150 km (E-region), and 150–400 km (F-region). The D-region in particular is of primary interest for this dissertation (as discussed further in the following section).

Subionospheric VLF Propagation

The D-region is particularly important for the current work because Very Low Frequency (VLF 3–30 kHz) electromagnetic waves are effectively reflected from the sharp gradient in the electron density (N_e) at its lower boundary. This property is important because the sharp reflection at the lower boundary of the ionosphere combined with the reflection of VLF waves from the surface of the Earth form a very efficient waveguide at VLF frequencies. The so-called Earth-ionosphere waveguide allows for the propagation of VLF waves to great distance [*Budden*, 1953]. On the bottom side

of the waveguide, the Earth represents a very good (though not perfect) conductor at VLF frequencies with ground conductivities typically ranging from 10^{-4} to 10^{-2} S/m and seawater at 4 S/m [*Morgan*, 1968]. The conductivity of the ionosphere on the other hand is much less ($\sim 10^{-5}$ S/m) and the wave properties are determined by the complex index of refraction. A full treatment of this process requires extended analysis [*Ratcliffe*, 1959; *Budden*, 1985], and only the primary characteristics are discussed here. The Appleton-Hartree equation

$$n^2 = 1 - \frac{X}{1 - jZ - \dfrac{Y^2 \sin^2\theta}{2(1 - X - jZ)} \pm \left\{ \left[\dfrac{Y^2 \sin^2\theta}{2(1 - X - jZ)} \right]^2 + Y^2 \cos^2\theta \right\}^{1/2}} \qquad (1.1)$$

describes the refractive index as a function of the wave frequency (ω), the electron density (N_e), the magnitude of the geomagnetic field (B_0) and the direction of wave propagation relative to the magnetic field (θ). In addition, X, Y, Z are frequently used plasma parameters [*Budden*, 1985] relating important physical phenomena to the wave frequency:

$$X = \frac{\omega_p^2{}^2}{\omega} \qquad \text{and} \qquad \omega_p^2 = \frac{q_e^2 N_e}{m_e \epsilon_0} \qquad (1.2a)$$

$$Y = \frac{\omega_H}{\omega} \qquad \text{and} \qquad \omega_H = \frac{|q_e| B_0}{m_e} \qquad (1.2b)$$

$$Z = \frac{\nu}{\omega} \qquad (1.2c)$$

where ω_p is the plasma frequency, ω_H is the electron gyrofrequency, ν is the electron-neutral collision frequency, q_e and m_e are respectively the charge and mass of an electron and ϵ_0 is the permittivity of free space. Electrons typically dominate the ionospheric conductivity, however ions can also represent a very important contribution to the total ionospheric conductivity especially at low altitudes [*Lehtinen and Inan*, 2007]. If the ionosphere were a collisionless plasma, the plasma frequency would represent the cutoff frequency of wave propagation and waves would reflect at an altitude where $\omega = \omega_p$ (or equivalently n=0). However, in the relatively dense

atmosphere of the D-region, ν is high enough that the plasma oscillations are disrupted by collisions with neutral molecules so that n never reaches zero. Instead, a VLF wave travels upwards until it reaches an altitude where $\mathrm{d}n/\mathrm{d}h$ becomes large [*Ratcliffe*, 1959, Ch.12]. At this altitude an excellent estimate for the reflection height (h_r) of VLF waves in the ionosphere can be calculated from:

$$X = Z \quad \text{or equivalently} \quad \omega_p^2 = \omega\nu. \tag{1.3}$$

At VLF frequencies the nighttime reflection altitude is $\sim$85 km [*Inan et al.*, 1985a] while during the daytime the reflection height is at $\sim$70 km [*Rasmussen et al.*, 1980]. With each reflection of the wave from the ground a finite amount of energy is lost due to the imperfect nature of the ground reflection. Additionally, with each reflection from the ionosphere (transmission) some percentage of energy leaks through the top of the ionosphere thus attenuating the wave [*Helliwell*, 1965; *Lehtinen and Inan*, 2009]. In addition to wave attenuation due to reflection and transmission at each boundary, the wave is also affected by the electron density below the reflection height. The motion of ionospheric electrons in response to the wave electromagnetic fields causes a transfer of wave intensity to thermal energy and the wave experiences absorption as it propagates through the ionosphere [*Ratcliffe*, 1959, Ch.5]. The absorption coefficient (χ) is the imaginary component of the refractive index (n) and the wave amplitude attenuates with distance x as:

$$\exp\left[-\frac{|\chi|\omega}{\mathrm{c}}x\right]. \tag{1.4}$$

The Earth-Ionosphere Waveguide

Though accurate and useful for describing the propagation of VLF waves in the Earth-ionosphere waveguide, application of the Appleton-Hartree equation shown in Equation (1.1) can be cumbersome for macroscopic wave properties. A more intuitive approach is to discuss the problem of wave propagation in terms of the properties of the Earth-ionosphere waveguide itself.

For short distances, the best approach to this problem is to treat each wave as a ray which reflects back and forth from the boundaries of the waveguide and to calculate the reflection and transmission coefficients as a function of incident angle for each ray. However, at long distances this approach becomes unwieldy as the number of required rays increases exponentially, and a better approach is to determine propagating modes.

Modes are most easily understood in terms of a simple example with two parallel plates (infinitely wide) and perfectly reflecting boundaries, separated by a distance h. The two types of modes which propagate in this scenario have an electric (magnetic) field transverse to the direction of propagation and are called TE (TM) modes.

The most intuitive derivation for the characteristics of the propagating waveguide modes comes by imagining each (TE or TM) mode to be the superposition of two uniform plane waves propagating upwards and downwards at an angle θ_m with respect to the normal of the waveguide boundaries (as shown in Figure 1.2 [*Inan and Inan*, 2000, p. 270]). The planes of constant phase for the uniform plane wave propagating downward are shown perpendicular to the direction of propagation with successive peaks (nulls) shown as solid (dashed) lines and separated by a distance of one free-space wavelength, λ (the constant phase fronts for the upward propagating plane wave are not shown). In order for the ray paths and phase fronts to be valid as depicted, the height of the waveguide must be an integer multiple of the vertical wavelength ($\lambda_h = \lambda/\cos\theta_m$), and the eigenangle satisfying this condition is

$$\theta_m = \cos^{-1}\left[\frac{m\lambda}{2h}\right], \qquad (m = 1, 2, 3...). \tag{1.5}$$

Of course the Earth-ionosphere waveguide is not a parallel plate waveguide with perfectly conducting walls as discussed here, but rather one with finitely conducting boundaries, one of which is also anisotropic. In addition, the curvature of the Earth and ionosphere means that the waveguide consists of concentric spheres rather than parallel plates. The spherical nature of the waveguide results in modes which are not entirely TE or TM but rather are labeled QTE_m or QTM_m where the 'Q' indicates
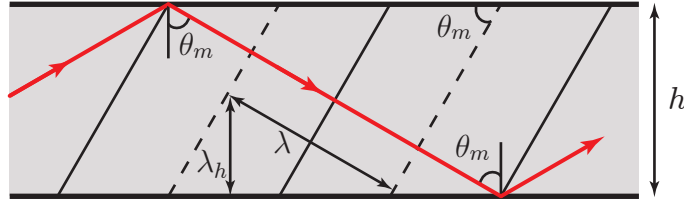
Figure 1.2: Propagating waveguide modes described as plane waves reflecting between parallel plates. Modified from *Inan and Inan* [2000, p. 270].

that the modes are quasi-transverse electric or magnetic. Each of these modes propagates down the waveguide with a different phase velocity and with different waveguide attenuation. At long distances the full electromagnetic wave can be decomposed into just a few (i.e., 4–5) separate waveguide modes.

VLF Remote Sensing

One important reason why remote sensing of the ionosphere is possible because of the presence of VLF communication transmitters operated by navies around the world. These VLF transmitter signals can propagate in the Earth-ionosphere waveguide over vast distances (>10 Mm) and can be used as reliable coherent sources with which to probe the D-region ionosphere. At long distances from the source, a VLF signal propagating in the Earth-ionosphere waveguide can be thought of as the superposition of just a few (primarily QTM_m) modes. Although the attenuation for low order TE_m modes is lower than some of the QTM_m modes, the relative excitation amplitude for QTM_m modes by VLF transmitters (specifically for QTM_2 and QTM_3) is quite high compared to other modes with similar attenuation [*Poulsen*, 1991, and references therein].

By placing a receiver some distance away from the transmitter as shown in Figure 1.3a, it is possible to effectively sample the properties of the waveguide because modification of the waveguide properties (and therefore a change in the characteristics of the propagating modes) manifest themselves in perturbations of the received VLF signal amplitude and phase. Since the conductivity of the Earth's surface is effectively constant with time, any observed changes in the signal amplitude/phase are the result

of changes in the ionospheric electron density profile. An example of a modification in the electron density profile is shown qualitatively in Figure 1.3a (and quantitatively in Figure 1.3d). As the signal passes under/through such an ionospheric disturbance region each mode is 'scattered' resulting in an altered amplitude and phase, and in some cases there is conversion from one mode to another [e.g., *Poulsen et al.*, 1993a].

The decomposition of the total received signal can be thought of in terms of an ambient signal (a superposition of waveguide modes) which propagates directly from the transmitter to the receiver, and a signal 'scattered' by the ionospheric disturbance which is itself the superposition of a number of modes (as shown in Figure 1.3b). The total received signal is then a phasor (vector) sum of the direct and scattered signals, each with an associated amplitude and phase. The total received signal can then be decomposed into two phasors (each with its own amplitude and phase) consisting of the direct and scattered signals.

A phasor representation is shown in Figure 1.3c where the direct signal is shown by the green vector (E_d), an example scattered phasor is shown by the red vector E_s1 and the total signal (E_t1) is shown by the blue vector. The associated amplitude and phase changes are shown as ΔA_1 and $\Delta \phi_1$, respectively. Notice that if the location of the disturbance region is shifted along the path between the transmitter and receiver the phase of the scattered signal will be altered while the amplitude will (likely) be similar. This shift leads to the scattered wave adding either constructively (as shown by E_t1) or destructively. The possible range of variations are highlighted by the yellow circle showing all possible constructive and destructive combinations of the direct phasor with a constant-magnitude phasor of varying phase.

1.1.2   The Magnetosphere

Above the ionosphere is a region around the Earth called the 'magnetosphere' which is a (nearly) completely ionized, collisionless plasma where physical interactions (including charged particle motions and electromagnetic wave dynamics) are dominated by the Earth's magnetic field. At lower altitudes, the influence of Earth's magnetic field gives way to the dynamics of the ionosphere as discussed above, while at the upper
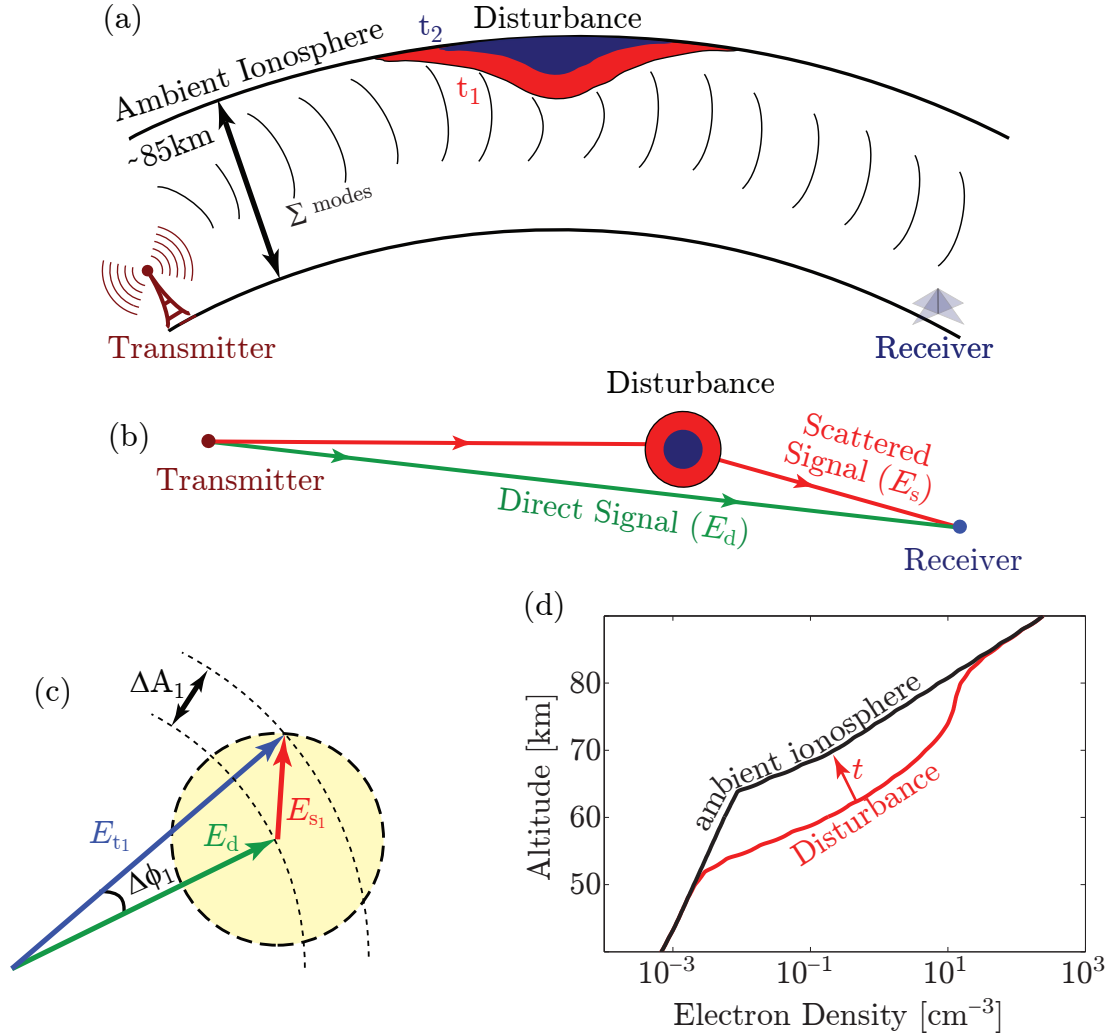
Figure 1.3: (a) VLF transmitter signal (sum of modes) propagating down the Earth-ionosphere waveguide and scattering off an ionospheric disturbance. (b) Top-view of waveguide showing the direct path from transmitter to receiver and the signal scattered towards the receiver by the disturbance region. (c) Vector (phasor) representation of the combination of the direct and scattered signal observed at the receiver. (d) Example ambient and disturbed electron density profiles.

boundary the sphere of influence for the magnetic field is determined by interactions with the solar wind. The solar wind is comprised of hot plasma ejected from the Sun's atmosphere and typically flows outward at a rate of ∼400–500 km/s [*Tascione*, 1988, Ch.3]. The force exerted by the solar wind on the geomagnetic field serves to compress Earth's magnetic field on the day-side magnetosphere and to elongate it significantly on the night-side, producing the general magnetospheric shape shown in Figure 1.4. The magnetosphere extends about 10–12 Earth radii (R_E) on the day side and as much as 60–$100R_E$ on the night side. The extent of the magnetosphere is defined by the magnetopause which is the surface where the force exerted by the solar wind is balanced by the combined pressures of the compressed magnetic field and the magnetospheric plasma [*Tascione*, 1988, Ch.5].

For the purposes of this dissertation the most important region of the magnetosphere is the inner magnetosphere where the magnetic field lines are 'closed' and which extends out to ∼6–$7R_E$. Within this portion of the magnetosphere there are two populations of charged particles which are important to magnetospheric dynamics. The first is known as the background or cold plasma and is comprised of low energy particles (typically less than 1 eV) at densities of 10–10^4 cm^{-3}. The cold plasma population determines wave properties within the magnetosphere and is characterized by a relatively slow decrease in density away from the Earth and a sudden drop in density at the so-called 'plasmapause' [*Carpenter*, 1963]. The location of the plasmapause can change drastically with geomagnetic conditions. The region inside the plasmapause, known as the 'plasma sphere' can fill with particles and extend out to ∼$7R_E$ during quiet periods and may be eroded so that the plasmapause moves to only ∼$2R_E$ during disturbed periods. The second population of particles are high-energy particles (or hot plasma) of ∼1 keV up to 10's of MeV which form what are known as the Van Allen Radiation Belts [*Walt*, 2005, p. 1] (illustrated in the expanded portion of Figure 1.4). Though this hot plasma constitutes only ∼1% of all magnetospheric particles, the particles within the radiation belts are the culprits causing much of the damage to space-borne assets discussed above and their removal mechanisms is thus the primary subject of this dissertation.
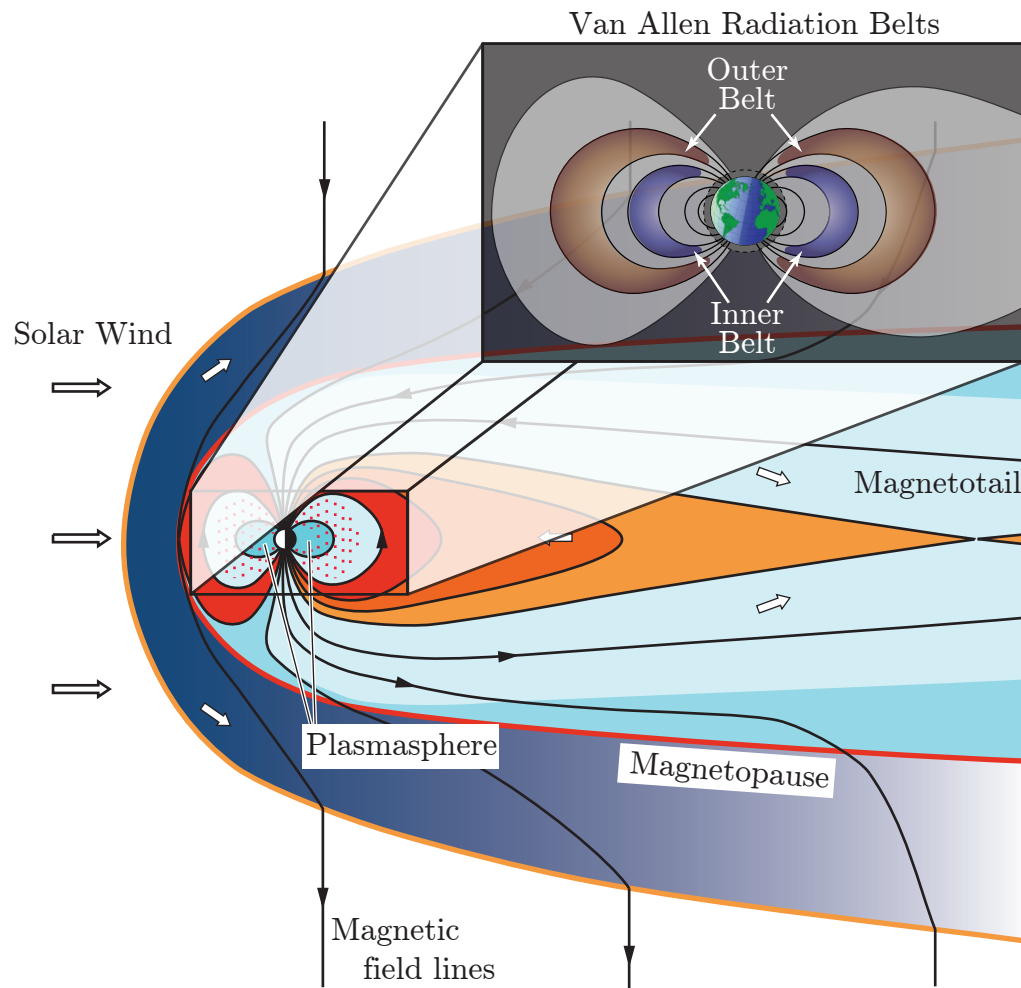
Figure 1.4: Illustration of the magnetosphere showing the interaction of the solar wind with the geomagnetic field and highlighting the plasma sphere and Van Allen Radiation Belts.
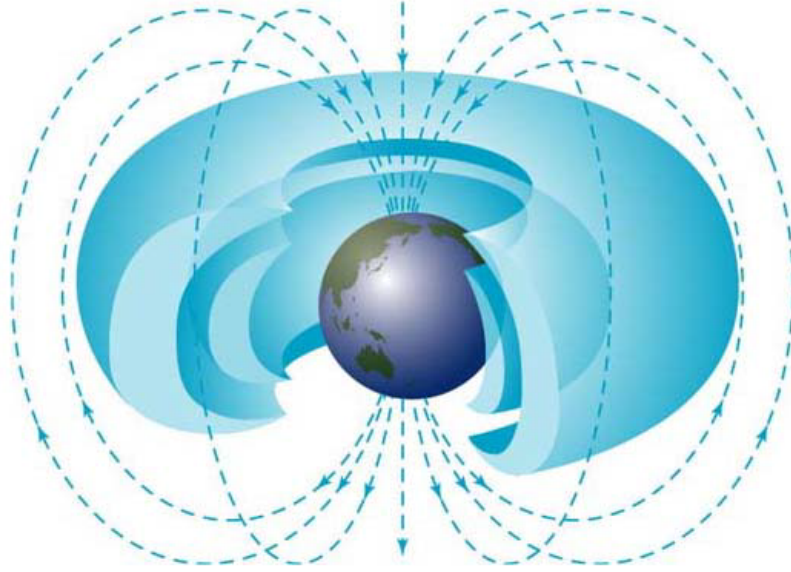
Figure 1.5: A 3-D graphical depiction of the Van Allen Radiation Belts and Earth's magnetic field. Figure courtesy of NASA.

Radiation Belts

The radiation belts consist of concentric toroidal belts of high energy particles (termed the inner and outer radiation belts) and are separated by a region of depleted electron fluxes known as the slot region (shown in Figure 1.5). Since their discovery by James Van Allen in 1958 [*Van Allen et al.*, 1959] there has been significant progress in understanding the replenishment, acceleration and loss processes for these high energy particles. New electrons and ions are constantly being injected into the outer boundary of the Earth's magnetosphere [e.g., *Li et al.*, 1997] by coronal mass ejections, solar flares and other solar events where they fall under the influence of the geomagnetic field, become trapped and diffuse radially inward, during which time they are accelerated by different processes to form the radiation belts.

The continuous filling and acceleration of the radiation belts is balanced with loss mechanisms which have been the subject of significant research aimed at understanding and predicting how electrons are removed from the radiation belts. There have been numerous studies of particle interaction with whistler mode waves from many

sources including plasmaspheric hiss [*Lyons and Thorne*, 1973], lightning generated whistlers [*Dungey*, 1963; *Abel and Thorne*, 1998a,b], anthropogenic VLF transmitters [*Abel and Thorne*, 1998a,b; *Inan et al.*, 2007; *Kulkarni et al.*, 2008] and electromagnetic ion-cyclotron (EMIC) waves [*Thorne and Kennel*, 1971]. Despite this wealth of research, consensus on the dominant factors involved has yet to be reached. Nevertheless, understanding the physical mechanisms involved in the removal of these electrons is of utmost importance for accurately predicting the lifetimes of the increasingly large number of orbiting satellites.

Earth's Magnetic Field

In order to discuss the motion (and removal) of radiation belt electrons it is first necessary to understand the medium in which they are located. The dynamics of magnetospheric plasma is dominated by the presence of Earth's magnetic field and though not completely understood, the origin of the Earth's magnetic field is thought to be due to electrical currents produced by Earth's slowly rotating liquid metallic outer core which acts as a self-exciting dynamo [e.g., *Walt*, 2005, p.25]. To zeroth-order, Earth's magnetic field can be approximated as a tilted centered dipole, the strength of which can be found by calculating the gradient of the magnetic potential [*Walt*, 2005, p.29] and then separating the magnetic field into radial (r) and latitudinal (λ) components. In doing so, it is possible to represent the magnetic field **B**, as:

$$B_r(r,\lambda) \;=\; -2B_0 \left(\frac{R_{\mathrm{E}}}{r}\right)^3 \sin\lambda \tag{1.6a}$$

$$B_\lambda(r,\lambda) \;=\; B_0 \left(\frac{R_{\mathrm{E}}}{r}\right)^3 \cos\lambda \tag{1.6b}$$

where r is measured from the center of the dipole field and λ is the geomagnetic latitude, R_{E} is the radius of the earth ($\sim$6370 km), and B_0 is the mean value of the magnetic field at Earth's surface along the equator ($\sim$3.12$\times$10^{-5} T). Given the two components, the total magnitude can be written:

$$B(r,\lambda) = \sqrt{B_r^2 + B_\lambda^2} = B_0 \left(\frac{R_{\mathrm{E}}}{r}\right)^3 \sqrt{1 + 3\sin^2\lambda}. \tag{1.7}$$

The L-shell Parameter

The above calculation is appropriate for illustrative purposes and for discussion of the basic properties of magnetospheric particle motion (discussed below) but a simple dipole model does not represent the true nature of the geomagnetic field and is insufficient for quantitative calculations. The methodology applied above is applicable to an arbitrary magnetic field and for the present work a full spherical harmonic expansion ($\geq$10 terms) of **B** is necessary, including corrections in the geomagnetic coordinate system [*Gustafsson et al.*, 1992; *Papitashvili et al.*, 1997].

The non-ideal nature of the geomagnetic field makes it difficult to discuss specific coordinates within the field (i.e., to determine the magnetic field at any location as described above) and the fact that the field strength varies continuously [*Fraser-Smith*, 1987] makes calculations still more difficult. To address these problems it is therefore necessary to adopt a different coordinate system for describing magnetospheric positions in the magnetosphere. Based upon the strength of the magnetic field and a function (I) related to the second adiabatic invariant (introduced in the following section), the best coordinate for this purpose is the McIlwain L-parameter [*McIlwain*, 1961].

The L-parameter specifies the set of points which form the locus of constant **B** and I. Particles which initially mirror at a specific **B** and I continue mirroring at the same **B** and I as they drift around Earth. In addition, the L-shell parameter also has a simple intuitive meaning. In a dipole field the L-shell corresponds to a magnetic field line which crosses the magnetic equator at L Earth radii, an intuition which also holds closely for the true geomagnetic field [*Walt*, 2005, p. 54].

Magnetospheric Particle Motion

With this basic understanding of the Earth's magnetic field it is possible to discuss the motion of charged particles located in the magnetosphere. Though the magnetosphere is permeated by many species of charged particles, high energy electrons are of primary interest to this work. The motion of any radiation belt electron is influenced by external electric and magnetic fields as well as any other force which causes

the electron to move in the presence of a magnetic field, such as gravity (though the direct effects of gravity are not considered here). The equation of motion for such an electron is governed by the Lorentz force shown below

$$\frac{d\mathbf{p}}{dt} = q_{e} \left\{ \mathbf{E} + \mathbf{v} \times \mathbf{B} \right\} \tag{1.8}$$

where $\mathbf{p} = \mathbf{v} m_{e} \gamma$ is the momentum vector of the electron (with rest mass m_{e} and charge q_{e}), $\mathbf{v} = d\mathbf{r}/dt$ is the particle velocity vector, $\mathbf{r}$ is the particle position vector, $\gamma = (1 - v^{2}/c^{2})^{-1/2}$ is the relativistic Lorentz factor and $\mathbf{E}$ and $\mathbf{B}$ are electric and magnetic field vectors influencing the electron.

In the magnetosphere under ambient conditions there is no electric field and so the electrons remain stably trapped in the magnetic mirror created by the Earth's magnetic field, experiencing three distinct periodic motions governed by Equation (1.8). First, electrons gyrate around the magnetic field with a gyrofrequency determined by the strength of the magnetic field. While doing so they traverse the magnetosphere along a single magnetic field line to an altitude at which they mirror and bounce back along the same field line. Finally, the electrons drift around the Earth.

Though the Lorentz force equation can be used to determine the motion of any magnetospheric charged particle, determining the long-term location of a particle would require numerical integration of Equation (1.8) over many inter-hemispheric bounces and spanning many degrees of longitude [*Walt*, 2005, p. 36]. In doing so, small deviations in the particle position are likely to compound into substantial errors which reduces the validity of this approach. The solution to this problem is the introduction of three 'adiabatic invariants' which are effectively constant during their respective particle motions (assuming that any force which changes their value varies very slowly) [*Walt*, 2005, p. 36]. The three adiabatic invariant paths are the gyration around the magnetic field line, the traverse of the magnetic field line in the magnetic mirror and the longitudinal drift around the Earth.

The three adiabatic invariants are easily separable based upon the time scales of their motion. For high energy electrons ($\gtrsim$50keV) the period of gyration is $\sim$$10^{-3}$ s, the bounce period is $\sim$0.1 s and the drift period is $\sim$$10^{3}$ s. In the absence of external

forces, each of these motions remain constant within their respective periodicities and the associated invariants are found by integrating the canonical motion of the electron around the respective orbit path [*Walt*, 2005, p.39]:

$$J_n = \oint (m_{\mathrm{s}}\mathbf{v} + q_{\mathrm{s}}\mathbf{A}) \cdot \mathrm{d}\ell, \qquad (n = 1, 2, 3) \tag{1.9}$$

where the integration is over the respective cycle, $\mathbf{A}$ is the vector magnetic potential, $m_{\mathrm{s}}\mathbf{v} + q_{\mathrm{s}}\mathbf{A} = \mathbf{p}$ is the canonical momentum, $\mathrm{d}\ell$ is an element of the path around the particle orbit and other variables are as defined above. Most important to the current work is the mirroring altitude of trapped electrons, which is determined by the first adiabatic invariant. The first adiabatic invariant (often referred to as the magnetic moment) is derived by integrating Equation (1.9) around the particle gyration orbit.

$$J_1 = \frac{p_{\perp}^2}{2m_{\mathrm{e}0}B} \propto \frac{\sin^2 \alpha(\mathbf{r})}{B(\mathbf{r})} = \mathrm{constant} \tag{1.10}$$

where $p_{\perp}$ is the component of the electron momentum perpendicular to the magnetic field, $m_{\mathrm{e}0}$ is the rest mass of the electron, B is the magnitude of the magnetic field and α is a parameter known as the pitch angle ($\alpha = \tan^{-1}[v_{\parallel}/v_{\perp}]$), where $v_{\parallel}$ and $v_{\perp}$ are (respectively) the components of the particle velocity parallel and perpendicular to the magnetic field. The pitch angle parameter is widely used in magnetospheric physics and using Equation (1.10) it is apparent that given a particle pitch angle and location it is possible to calculate the pitch angle at any other location provided the magnetic field strength as a function of location is known. The location which is chosen as the typical reference point for magnetospheric electrons is the equatorial pitch angle (α_{eq}), which is the pitch angle at $\lambda = 0°$, i.e., the geomagnetic equatorial plane.

The Equatorial Loss Cone ($\alpha_{\mathrm{eq}}^{\mathrm{lc}}$)

It is clear based upon Equation (1.10) that as the electron travels down the magnetic field line and the strength of the magnetic field increases, the pitch angle of the electron also increases. At some altitude (h_{m}) the magnitude of the geomagnetic

field becomes large enough such that α=90° and the electron 'mirrors' and begins to travel in the opposite direction, returning to the magnetosphere. The altitude at which this mirroring occurs is of critical importance for the removal of electrons from the radiation belts because as the electron progresses down in altitude along a given field line, at some altitude the neutral density is high enough that a downward-traveling (precipitating) electron likely impacts a neutral atom before mirroring. In such a collision, the energy of the electron is converted into heat, ionization, x-rays and other atmospheric losses, so that the electron is thus lost from the radiation belts. The altitude at which this loss is typically assumed to occur [e.g., *Walt*, 2005; *Peter and Inan*, 2007] is at ~100 km because the density of the neutral atmosphere increases exponentially (scale height of only ~6 km [*Salby*, 1996, p.9]) with altitude compared with the relatively small spatial scales of precipitating electrons (gyroradius ~10's of meters).

Relating this altitude back to the equatorial pitch angle (α_{eq}) then gives a useful and quantitative metric for determining the current status of any radiation belt electron. The equatorial loss cone angle (henceforth designated α_{eq}^{lc} or to designate the loss cone angle at an arbitrary altitude: α_{lc}) can be calculated by noting that if R_0 is the distance from the center of the Earth to the point where the field line intersects the equatorial plane then:

$$r = R_0 \cos^2 \lambda \tag{1.11}$$

The equatorial pitch angle can be simply calculated from the ratio of B_{eq} and B_{m} using Equation (1.10). This ratio can in turn be found from Equation (1.7) by setting $r = R_E + h_m$ at B_m and $r = R_0$ at B_{eq}. Combining the results with Equation (1.11) yields:

$$\sin \alpha_{lc} = \left[\varsigma_m^3 \sqrt{1 + 3(1 - \varsigma_m)} \right]^{1/2} \quad \text{where} \quad \varsigma_m = \frac{R_E + h_m}{R_0}. \tag{1.12}$$

The important utility of the quantity α_{lc} with respect to radiation belt electron loss is that it constitutes a single parameter which describes all of the physical variables necessary to determine the fate of a magnetospheric electron. As can be seen pictorially in Figure 1.6, the loss cone angle demarcates the line between precipitating
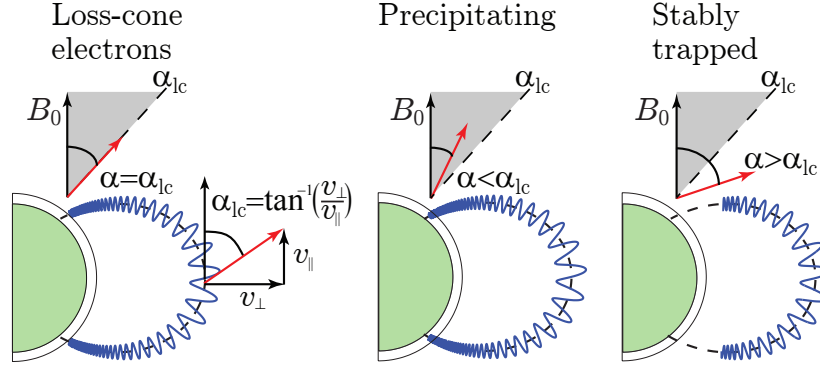
Figure 1.6: Relationship between the mirror height and the loss cone angle.

and stably trapped electrons. An electron with equatorial pitch angle $\alpha_{\mathrm{eq}} < \alpha_{\mathrm{eq}}^{\mathrm{lc}}$ penetrates to an altitude $\leq h_{\mathrm{m}}$, likely impacts a neutral atmospheric molecule, and is said to 'precipitate' out of the magnetosphere (constituting radiation belt electron loss). Conversely, an electron with $\alpha_{\mathrm{eq}} > \alpha_{\mathrm{eq}}^{\mathrm{lc}}$ mirrors at an altitude above the dense portion of the neutral atmosphere and remains stably trapped in the magnetosphere. It is typical to broadly classify electrons as either precipitating or stably trapped because in the absence of external forces (a good approximation in most cases) any electron which is initially trapped remains trapped indefinitely while any electron which is precipitating impacts a neutral atom and is removed from the radiation belts.

Additionally, electrons which have a pitch angle $\alpha_{\mathrm{eq}} \simeq \alpha_{\mathrm{eq}}^{\mathrm{lc}}$ are termed 'near loss cone' electrons and are important because they mirror at an altitude above, but still very near (with an atmospheric density scale height of $\sim$6 km, the term 'very near' literally means on the order of a few kilometers) to the dense portion of the neutral atmosphere. In an ideal scenario these electrons would be no different than any other stably trapped electron because the first adiabatic invariant dictates that the ratio of the pitch angle and the magnetic field is constant. However, in practice the first adiabatic invariant can be violated by external forces and the pitch angle of an electron can be altered such that it can cross the boundary between stably trapped and precipitating.

1.1.3 Wave-Particle Interaction

Many of the primary phenomena which are involved in altering magnetospheric electron pitch angles are interactions with electromagnetic waves (from various sources) which propagate throughout the magnetosphere. Some examples of these waves are plasmaspheric hiss [*Lyons and Thorne*, 1973], lightning generated whistlers [*Dungey*, 1963; *Abel and Thorne*, 1998a,b], anthropogenic VLF transmitters [*Abel and Thorne*, 1998a,b; *Inan et al.*, 2007; *Kulkarni et al.*, 2008]. In each of these cases the electromagnetic energy propagates in the form of what is known as a whistler-mode wave which can affect trapped radiation belt particles through wave-particle interactions. Similar to the motion of charged particles in the Earth's magnetic field, the interaction of charged particles with external (wave) electromagnetic fields is described by the Lorentz force equation. This equation, modified to include the presence of electric ($\mathbf{E}^{\mathrm{w}}$) and magnetic fields ($\mathbf{B}^{\mathrm{w}}$) due to an electromagnetic wave, is

$$\frac{\mathrm{d}\mathbf{p}}{\mathrm{d}t} = q_{\mathrm{e}} \left\{ \mathbf{E}^{\mathrm{w}} + \mathbf{v} \times [\mathbf{B}^{\mathrm{w}} + \mathbf{B}_0(\mathbf{r})] \right\}. \tag{1.13}$$

Under typical conditions in the magnetosphere the whistler-mode is the only wave which can propagate at VLF frequencies and therefore the ($\mathbf{E}^{\mathrm{w}}$) and ($\mathbf{B}^{\mathrm{w}}$) field components in Equation (1.13) correspond to whistler-mode fields. Sometimes also called an electron-cyclotron mode, a whistler mode wave propagating with k-vector in the direction of the magnetic field is a right-hand circularly polarized wave with electric and magnetic fields which are transverse to the direction of propagation. Furthermore, whistlers propagate only at frequencies below the electron gyrofrequency (ω_H) and above the proton gyrofrequency and with very low group velocity (much less than the speed of light) [*Helliwell*, 1965, Sec. 3.3]. Though discussed in limited fashion beforehand, the origin and characteristics of whistlers were discovered by *Storey* [1953, and references therein] and since that time the interaction of a whistler-mode wave with magnetospheric electrons has been the topic of countless studies and investigations [e.g., *Dungey*, 1963; *Helliwell et al.*, 1973; *Inan et al.*, 1978; *Dingle and Carpenter*, 1981; *Chang and Inan*, 1985; *Omura et al.*, 1991; *Johnson et al.*, 1999; *Dowden et al.*, 2001; *Peter and Inan*, 2007; *Gibby et al.*, 2008; *Gołkowski et al.*, 2008].

In the present work the most important aspect of this investigation is the pitch-angle scattering of electrons which is caused by interaction with whistler-mode waves launched by lightning. The complicated set of equations describing this pitch angle scattering due to whistlers propagating at oblique angles to the magnetic field was originally developed by *Bell* [1984] and is beyond the scope of this dissertation. However the key result of this work can be summarized through the resonance condition relating the angle, η, between the whistler wave magnetic field ($\mathbf{B}^{\mathrm{w}}$, with propagation constant k) and the component of the particle velocity parallel to the geomagnetic field ($v_\parallel$). For the non-relativistic case the resonance condition can be expressed as:

$$\frac{\mathrm{d}\eta}{\mathrm{d}t} = m\omega_H - \omega - k_\parallel v_\parallel \simeq 0. \tag{1.14}$$

The physical meaning of Equation (1.14) is that in the electron frame of reference, if the Doppler-shifted frequency of the whistler wave is equal to the electron gyrofrequency (or an integer multiple thereof) then the wave magnetic field appears stationary to the electron and the wave can redirect the momentum of the electron (through the Lorentz $\mathbf{v} \times \mathbf{B}^{\mathrm{w}}$ force), thereby altering the electron pitch angle (also termed pitch angle deflection or pitch angle scattering). Due to the rapid variation of the magnetic field strength with distance (which determines ω_H) this resonance is most effective near the geomagnetic equator where the geomagnetic field is roughly constant over a large latitude range. Additionally, changes in the pitch angle of an electron are generally referenced to the equatorial value, α_{eq}, for consistency.

The electrons with corresponding resonant velocity (v^{res} or equivalently the resonant energy $\mathcal{E}^{\mathrm{res}}$) can be found from Equations (1.14) and (1.10) through simple algebraic manipulation. This resonance condition can occur for an electron of any pitch angle, i.e., stably trapped far above the loss cone or just slightly above the loss cone. However, because a typical wave-particle interaction results in an equatorial pitch angle change of only a fraction of a degree [e.g., *Chang and Inan*, 1983; *Bortnik et al.*, 2006a,b] only those electrons near the loss cone are scattered sufficiently to reduce their pitch angle below the loss cone thus removing them from the radiation belts.

1.2 Lightning-induced Electron Precipitation

Having now discussed the scientific background necessary for understanding the removal of radiation belt electrons by whistler mode waves and their subsequent observation using VLF remote sensing, it is now possible to discuss the coupling between the ionosphere and magnetosphere in the form of lightning-induced electron precipitation (LEP). This method of *D*-region remote sensing using subionospherically propagating VLF signals has long been used as a tool in studying and quantifying the loss of radiation belt electrons due to LEP [e.g., *Helliwell et al.*, 1973; *Inan et al.*, 1985b; *Dowden and Adams*, 1988; *Lauben et al.*, 1999; *Peter and Inan*, 2004]. It has been predicted that LEP is the dominant natural loss process for electrons in the range $2 < L < 3$ [*Abel and Thorne*, 1998a,b], and its complete understanding is thus needed in order to quantify the loss of electrons from the radiation belts.

1.2.1 The LEP Process

The entirety of the LEP process is shown qualitatively in Figure 1.7 and begins when a lightning discharge occurs, emitting a large electromagnetic pulse which (much like VLF transmitter signals) is guided efficiently in the Earth-ionosphere waveguide. In the near-field region around the lightning flash the wave energy can be thought of in terms of rays which reflect back and forth between the Earth and the ionosphere. At each reflection from the ionosphere, a small portion of the wave energy leaks through the ionosphere and enters the magnetosphere as a whistler-mode wave, and is shown propagating up the magnetic field line in Figure 1.7a.

Upon entering the magnetosphere the whistler-mode wave propagates out to the equatorial region and interacts with the high energy radiation belt electrons in a wave-particle interaction. As discussed in Section 1.1.3 this interaction occurs when the Doppler-shifted frequency of the whistler-mode wave equals the gyrofrequency of a trapped radiation-belt electron [*Helliwell et al.*, 1973]. In this situation a cyclotron resonance occurs whereby the momentum of the electron is redirected through interaction (over several gyro-periods) with the wave magnetic field. The result of this interaction can change the electron pitch angle sufficiently to reduce it below the loss
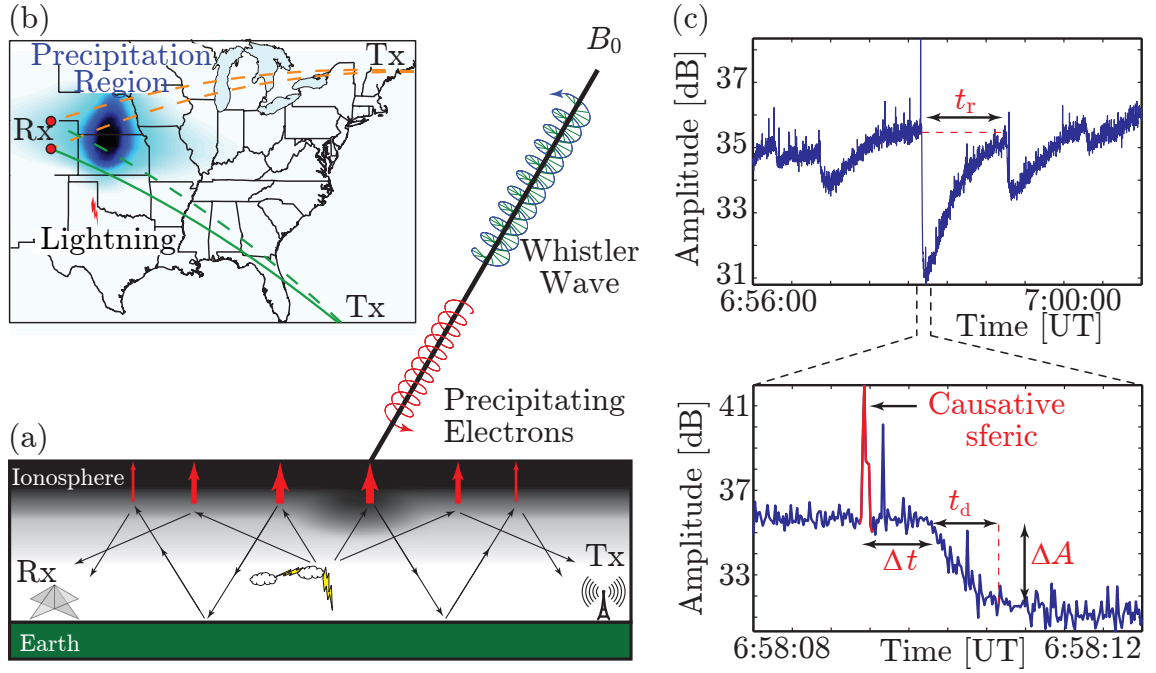
Figure 1.7: Description of the LEP process. (a) Earth-ionosphere waveguide with transmitter and receiver on the ground, lightning EMP coupling through the ionosphere and propagating up the field line as a whistler-mode wave, and precipitating electrons coming down the field line creating an ionospheric disturbance. (b) Example lateral extent of an ionospheric disturbance region due to LEP with four transmitter-to-receiver paths passing through or near the ionospheric disturbance. (c) Subionospheric VLF signal perturbation associated with LEP, highlighting the four primary LEP event characteristics: onset delay (Δt), onset duration (t_d), amplitude change (ΔA) and recovery time (t_r).

cone, causing the electron to impact the ionosphere and precipitate as shown at the base of the field line in Figure 1.7a.

Precipitating electrons produce one electron ion pair for each 35 eV of deposited energy [*Rees*, 1963] and for precipitating electrons with energy on the order of keV, the amount of secondary ionization produced results in a large disturbance region in the ionosphere as shown at the base of the field line in Figure 1.7a. When the secondary ionization produced by these precipitating electrons is sufficient to cause an appreciable percentage change in the ambient D-region conductivity, the disturbance can be observed remotely using subionospherically propagating VLF transmitter signals as discussed in Section 1.1.1.

At the time when they were first observed [*Helliwell et al.*, 1973], the conclusive link between lightning and perturbations of VLF signals had not yet been established, however the signal perturbations were (correctly) hypothesized to be due to secondary ionization produced by pitch-angle scattered energetic electrons near the VLF reflection height and were (eventually) named lightning-induced electron precipitation events [*Inan and Carpenter*, 1987]. In the years since there has been extensive experimental evidence for the existence of LEP events observed on rockets [e.g., *Goldberg et al.*, 1987], balloons [e.g., *Rosenberg et al.*, 1971] and via subionospheric VLF remote sensing [e.g., *Johnson et al.*, 1999; *Peter and Inan*, 2007], but the most conclusive evidence came from the satellite measurements of *Voss et al.* [1984] who observed bursts of precipitating electrons associated on a one-to-one basis with individual lightning-generated whistlers. Further analysis by *Voss et al.* [1998] indicated that a single LEP burst could precipitate ∼0.001% of the radiation belt electron population trapped along a specific field line. Direct in-situ satellite measurements are the most enlightening; however, the transient and localized nature of LEP events render satellite/rocket/balloon observations very difficult while hundreds of LEP bursts can be measured on a single night with VLF methods [e.g., *Lev-Tov et al.*, 1995; *Peter and Inan*, 2004].

1.2.2 Defining Characteristics of LEP Events

By monitoring the amplitude and phase of VLF transmitter signals for characteristic sudden perturbations with relatively long recoveries, VLF signal perturbations can be used as a proxy for the occurrence of LEP. An example disturbance region is shown in Figure 1.7b over the Central United States, with great circle paths (GCPs) from VLF transmitters located in in Maine and Puerto Rico and with end points (receivers) located in Wyoming and Colorado. When an LEP event occurs, the recorded VLF signal amplitude exhibits a sudden change followed by a slow recovery back to the ambient level. Figure 1.7c shows the characteristic signature of an LEP event and highlights the four defining characteristics.

- The magnitude of amplitude or phase change (ΔA or $\Delta \phi$) is the total amount of change observed in the transmitter signal.

- The onset delay (Δt) is the time from when the causative lightning flash occurs to when the amplitude of the signal begins to change.

- The onset duration (t_d) is the time over which the amplitude of the signal continues to change.

- The recovery time (t_r) is the time it takes for the amplitude of the transmitter signal to return to the pre-event level it would have exhibited in the absence of the disturbance.

Finally, by observing multiple transmitter signals at multiple locations, as shown by the map in Figure 1.7b, it is possible to determine the spatial extent of the precipitation region [*Johnson et al.*, 1999; *Peter and Inan*, 2004].

More important in terms of quantifying radiation belt electron loss is that the observed event characteristics are related to the number, energy and temporal signatures of precipitating electrons. Understanding the complexity (and quantification) of this relationship is thus a major goal of VLF remote sensing.

1.3   Motivation

Due to the indirect connection between VLF measurements and the parameters of interest (i.e., number, energy and duration of electrons removed from the radiation belts), quantification of the process is by nature a forward-modeling inversion problem. Previous work using this methodology has produced good agreement between the observed amplitude of LEP events and a comprehensive model of the LEP process [*Peter and Inan*, 2007]. However, one major discrepancy between previous modeling work and observation is a consistently shorter predicted onset delay (by ∼300 ms) than that observed in data [*Inan et al.*, 1988a; *Lauben et al.*, 1999; *Peter and Inan*, 2007].

It has been suggested [*Voss et al.*, 1998; *Peter and Inan*, 2007] that this discrepancy can be attributed to the effects of electrons which are incident upon the atmosphere at 'grazing incidence' i.e., $\alpha \simeq \alpha_{\mathrm{lc}}$. Such electrons are only slightly inside the loss cone and only briefly interact with the atmosphere before returning to the magnetosphere with slightly less energy and slightly changed pitch angles. These electrons are considered to be 'backscattered' from the atmosphere. An electron can backscatter from the atmosphere if in the course of the random scattering process the local pitch angle is altered such that it becomes $\geq 90°$. When this condition is satisfied the magnetic mirroring force resulting from the convergence of magnetic field lines causes the electron to return to the magnetosphere before depositing all its energy into the atmosphere.

The process of atmospheric backscatter can explain the discrepancy in modeled versus observed onset delay as follows. Suppose a distribution of precipitating electrons is incident upon the atmosphere (in the Northern Hemisphere) at grazing incidence (i.e., $\alpha_{100\mathrm{km}}$=90°). A small percentage of these electrons deposit all their energy into the atmosphere with many atmospheric interactions while the majority undergo only a few (or zero) atmospheric interactions, losing only a small amount of energy before backscattering. The net effect is that the pitch angle distribution of the backscattered electrons is slightly broadened, e.g., with pitch angles ranging from

$\alpha_{100km} \simeq 80°$–$90°$. In a dipole magnetic field these electrons then return to the magnetosphere, traversing the magnetic field line to the conjugate point in the Southern Hemisphere where they are again incident upon the atmosphere with the same range of pitch angles ($80°$–$90°$). The same atmospheric backscattering process occurs there except that because some of the incident electrons are now deeper inside the loss cone (i.e., penetrate to lower altitudes) a larger portion of the total energy is deposited and the electron distribution is made more isotropic in pitch angle (e.g., with electron pitch angles now ranging from $\alpha_{100km} \simeq 70°$–$90°$). The remaining electrons again traverse the magnetic field line back to the Northern Hemisphere and are incident once again on the atmosphere therein. The incident electrons are now deeper inside the loss cone and deposit more of their energy into the atmosphere. If this deposition results in the production of sufficient secondary ionization to significantly scatter the subionospheric VLF transmitter signal then the effect is observed as an LEP event with an onset delay time which is increased by one bounce period ($\sim$300–450 ms for 0.1–0.3 MeV electrons) from the initial estimate.

Under this scenario, it is also important to recognize that a significant percentage of electrons which are initially backscattered from the Northern Hemisphere and which are then incident upon the Southern Hemisphere deposit their energy in the southern hemisphere atmosphere. To determine the location (i.e., hemisphere), time (i.e., atmospheric interaction number), and amount of deposited energy from a particular precipitating electron distribution requires knowledge of both the incident energy ($\mathcal{E}_0$) and pitch angle (α_0) of the precipitating electrons. In the present work, these distributions have been determined by creating a model of the atmospheric backscatter response using a Monte Carlo model of atmospheric interactions with energetic particles based upon the work of *Lehtinen et al.* [1999].

1.4   Contributions of this Research

1. First prediction and verification of all LEP event characteristics through the inclusion of electron backscattering from the atmosphere.

2. First identification of longitudinal and hemispheric dependence of onset delay between causative lighting strike and LEP observation.

3. Identification, modeling and statistical verification of hemispheric and longitudinal dependence of LEP onset duration time.

4. Identification and modeling of differences in LEP recovery time resulting from a longitudinal and hemispheric dependence of electrons backscattered from the atmosphere.

5. Quantification of the effect of hemispheric dependence of LEP, demonstrating that the relative precipitation flux at conjugate points of the same field line is linked through the backscatter processes and hemispheric differences can vary by a factor of as much as 300.

1.5   Organization of the Dissertation

The Dissertation is organized into 6 chapters:

Chapter 1 describes the problem of radiation belt remediation and the scientific background necessary for addressing it, including discussion of the ionosphere, the magnetosphere and wave-particle interactions. It continues by describing LEP events, the primary natural loss process for radiation belt electrons in the $2 < L < 3$ region. The chapter then motivates the current research by describing discrepancies between the predicted and observed characteristics of LEP events found in past research. The chapter finishes with a description of how these discrepancies can be addressed by including the effects of electrons backscattered from the atmosphere and discusses the specific scientific contributions made while pursuing this goal.

Chapters 2–4 introduce the theoretical end-to-end model of the lightning-induced electron precipitation process and its effects in the D-region. This process follows a reverse causative order, i.e., starting with the later effects and proceeding to causative mechanisms and processes.

Chapter 2 continues the discussion of LEP events by further describing the event characteristics and their relationship to physical quantities. It then elaborates on the Chapter 1 discussion of the geomagnetic field with respect to the magnetic field asymmetry and how this asymmetry can affect LEP characteristics at different locations when combined with the effects of atmospheric electron backscatter. The chapter finishes with three case studies of LEP observations at different geographic locations which can be used to observe differences in LEP event characteristics in the context of atmospheric backscatter.

Chapter 3 describes the Atmospheric Backscatter (ABS) model used to predict the characteristics of LEP events at different longitudes. The model description begins with an overview of the Monte Carlo model upon which it is based and then discusses the atmospheric deposition response and atmospheric backscatter response to various monoenergetic beams of electrons at a single pitch angle $(\mathcal{E}_0, \alpha_0)$. The chapter then discusses how these individual atmospheric responses can be combined to describe the deposition profile and backscatter distribution for any arbitrary distribution of electrons incident upon the atmosphere and concludes with a simple example of the evolution of a backscattered distribution in conjugate hemispheres and at different longitudes.

Chapter 4 discusses the methodology for predicting the longitudinally-varying characteristics of LEP events. The chapter begins with an overview of a comprehensive Whistler-Induced Particle Precipitation (WIPP) model previously developed [*Bortnik et al.*, 2006a,b] which is used to calculate a realistic distribution of precipitating electrons for input into the ABS model. The chapter continues by discussing how this input distribution evolves at different longitudes and concludes by predicting the LEP event characteristics at the three locations described in Chapter 2.

Chapter 5 compares the predicted characteristics of LEP events from Chapter 4 with statistical observations of LEP events at locations described in Chapter 2 and demonstrates that by including the effects of electrons backscattered from the atmosphere it is possible to predict the characteristics of LEP events at any mid-latitude location. The chapter then concludes with a comparison of the predicted evolution of backscattered electrons with in-situ measurements of electrons backscattered from the atmosphere as they multiply reflect between hemispheres and show that the ABS model can further be used to predict the in-situ characteristics of backscattered electrons.

Chapter 6 summarizes the results presented in Chapters 2–5 and concludes with suggestions for future work and a description of how the ABS model can be used to quantify the loss of radiation belt electrons on a global scale.

Chapter 2

VLF Remote Sensing and LEP Event Signatures

2.1 Physics of LEP Event Characteristics

As introduced briefly in Section 1.2, each of the characteristics of observed LEP events (shown in Figure 1.7c) can be used to determine important information about the number and energy of precipitating electrons as well as the spatial and temporal profile of the precipitation region. To get a better understanding of this relationship each LEP characteristic is discussed separately in terms of its relationship to physical parameters. Each section below begins with a definition of the observed parameter and continues into a discussion of variables which can affect the observed characteristics.

LEP event characteristics can be separated into ionospheric and magnetospheric dependencies based upon where the physical interactions take place and are discussed below in this context. The perturbation magnitude and recovery time are determined primarily by physical interactions in the ionosphere while the onset delay and onset duration are primarily determined by magnetospheric interactions. In fact, prior to the work discussed herein, the ionospheric effects on onset delay and duration had not been considered in any depth.

2.1.1   Perturbation Magnitude (ΔA or $\Delta \phi$)

The perturbation magnitude (encompassing both amplitude and/or phase changes) is defined as the maximum deviation from the ambient signal level (either positive or negative) observed during the event and is measured in dB and degrees for amplitude and phase, respectively. The most obvious factor affecting both perturbation amplitude and phase is the amount of secondary ionization introduced by the precipitating electrons (discussed below); it is not, however, the most important factor. Even more important than the amount of secondary ionization created is the location of the disturbance region relative to the GCP between the transmitter and receiver.

The simplest case occurs when the ionospheric disturbance is directly on top of the GCP and in this situation the problem simplifies to the waveguide problem shown in Figure 1.3a. If the disturbance region does not change the waveguide properties significantly over wavelength-sized scales, i.e., if the conductivity changes are 'slowly varying' (a good assumption for LEP events), there is no conversion from one mode to another. For instance, the scattering of a QTM$_2$ mode from the disturbance region will not excite a QTE$_2$ mode or any other mode. The assumption involved here involves the well-known W.K.B. approximation (named for the authors who developed it concurrently: Wentzel, Krarners, and Brillouin), which has been used in many studies of subionospheric wave propagation [e.g., *Budden*, 1985, Ch.7].

When the disturbance is directly on top of the GCP, the treatment of the amplitude and phase perturbations can be simplified to a dependence on the wave absorption and reflection altitude, respectively. Recalling the definition of absorption from Equation (1.4), the amplitude of the wave attenuates by a factor:

$$\int_0^\ell \int_0^{h_\mathrm{r}} \exp\left[-\frac{|\chi|\omega}{\mathrm{c}}x\right]\,\mathrm{d}h\mathrm{d}\ell$$

where h_r is the VLF reflection height, —calculated from Equation (1.3)— ℓ is the distance between the transmitter and receiver, x is related to h and ℓ by the specific ray trajectory and χ is a function of both height and distance. Physically this equation is simply a statement that the amplitude of the wave attenuates due to absorption at all altitudes and over the entire distance between the transmitter and the receiver.

The phase perturbation, on the other hand, is relatively unaffected by the change in ionization as a function of altitude; rather the phase of the signal depends on the total path-length difference between the disturbed and undisturbed ionospheric propagation path. Recall from Equation (1.3) that for fixed wave and collision frequencies, the reflection altitude varies with $\sqrt{N_e}$. The difference in path length before and after precipitation is then due to the change in reflection altitude of the VLF signal. If the portion of the precipitation near the reflection altitude is significant then there is a measurable phase perturbation.

The second case considers a precipitation region which is not directly over the GCP between transmitter and receiver, as discussed in terms of direct and scattered phasors in reference to Figure 1.3b and 1.3c. While the above observations regarding the amplitude and phase of the signal still apply, in this case it is necessary to separately account for the amplitude and phase of both the direct signal along the GCP and the signal scattered from the precipitation region. It may seem logical that more secondary ionization results in a correspondingly larger LEP perturbation magnitude, but an equally important factor is the size and location of the disturbance region relative to the GCP. If the scattering creates a signal which is in-phase with the direct signal then the observed magnitude is positive, whereas if the scattered signal from the same disturbance region is observed in another location where it is out of phase with the direct signal then the observed amplitude change is negative. Therefore, complete characterization of the relationship between the observed event perturbation magnitude and the precipitation region is determined both by the amount of secondary ionization created and also the location of the ionization relative to the transmitter-receiver GCP.

The most easily visualized approach to this problem is to calculate the propagating modes as a function of distance under ambient ionospheric conditions and then to calculate the scattering of each mode from a disturbance region. The total signal is then just the vector sum of the contributions from each (direct and scattered) signal as illustrated in Figure 1.3c. Using the MODEFNDR code developed by Naval Ocean Systems Center (NOSC) [*Pappert and Snyder*, 1972; *Ferguson and Snyder*, 1987], this approach has long been used to investigate the effects of ionospheric modification on

subionospherically propagating VLF signals [*Dowden and Adams*, 1988, 1989; *Cummer and Inan*, 2000; *Moore et al.*, 2003] including a 3-D treatment by *Poulsen et al.* [1993a,b].

A more advanced approach to the problem is to solve Maxwell's equations on a finite difference grid in either the time or frequency domain (FDTD or FDFD, respectively) which provides a full solution for the propagating signal as a function of altitude and distance. This approach has been applied by *Chevalier et al.* [2007] to measure variations in the D-region over diurnal and seasonal durations, as well as during geomagnetic storms. The newest approach is to use a full-wave method to determine the properties of the waveguide, and while specifically applied to the study of direct-effects of lightning on the ionosphere, the methodology of *Lehtinen et al.* [2010] is directly applicable to the case of LEP events.

Most relevant for the current work is the application of the FDFD approach to determine amplitude and phase perturbations due to LEP by *Peter and Inan* [2007]. In this work a comprehensive model of electron precipitation due to lightning showed that the VLF amplitude and phase of an observed LEP event can be related to either the number of electrons removed from the radiation belts or the amount of secondary ionization created in the ionosphere. Following this same approach, it is possible to calculate the expected amplitude change due to any ionization source in any location. However, as a computationally efficient first-order estimate, the integrated line density enhancement (N_{ILDE}) metric [*Peter and Inan*, 2007] is an excellent alternative. N_{ILDE} is a single number which characterizes —for the purpose of estimating ΔA or $\Delta \phi$— the total integrated ionization created between the transmitter and the receiver and between the altitudes of 80 km and 85 km. While the N_{ILDE} metric is technically only valid for the exact path for which it was calculated, the linear relationship between ionization and amplitude implies that a similar (linear) relationship should also exist between LEP events observed on similar GCPs (such as the Northern Hemisphere locations discussed in Section 2.3). Though this approach does not address the contribution of ionization due to 'off-path' ionization (Figure 1.3b) the FDFD approach has been shown to successfully reproduce the amplitude characteristics of observed LEP events and is more than sufficient for a first-order estimate.

2.1.2 Recovery Time (t_r)

After a perturbation due to the factors described above, the signal level gradually returns to the level it would have exhibited in the absence of an ionospheric disturbance. This parameter is the recovery time and is defined as the time between maximum deviation from the pre-event level (i.e., where the perturbation magnitude is maximum) and when the signal returns to within 10% of the pre-event level.

This recovery is determined by the time it takes for ionospheric chemical equilibrium in the disturbed region to be re-established, and depends on the ion chemistry of the atmosphere. There have been many approaches to addressing this problem, from an exceptionally simple model consisting only of electrons [*Rodger et al.*, 1998], to an exceptionally complicated model involving 63 ion species, 13 neutral species and hundreds of rate coefficients relating the various species [*Turunen et al.*, 1996; *Verronen et al.*, 2002]. Ionospheric conductivity is typically dominated by electrons due to their high mobility. However, the simple model involving only electrons cannot be effectively used throughout the D-region because of the significant concentration differences of different ion species at different altitudes [*Mitra*, 1981; *Ferguson*, 1979; *Reid*, 1979] which leads to different conductivity lifetimes at various altitudes as described below.

- Altitude range $\gtrsim$85 km: The simplest region in terms of ionospheric chemistry is $\gtrsim$85 km because the negative ion concentration is less than that of electrons, and because the positive molecular ions O_2^+, and NO^+ recombine in a straightforward dissociative recombination process with free electrons (e^-).

- Altitude range $\sim$82–85 km: This range is known as the 'ledge' region, and is characterized by a disappearance of positive water cluster ions $H^+(H_2O)_n$, also called hydrated protons, where the subscript n is an integer and indicates that there are several species of water-cluster ions, each with a different number of water molecules clustered around a proton.

- Altitude range $\sim$70 km–82 km: Just below the 'ledge' is the region where the dominant positive ion species are the water cluster ions $H^+(H_2O)_n$. Negative

ions in this region consists primarily of NO_3^- and HCO_3^- with additional contributions from O_2^- and O^-. However, these latter two species are typically intermediate products in chemical reactions and while important, are typically short-lived.

- Altitude range 50–70 km: Here the population of negative ions increases and surpasses the concentration of electrons with ions such as NO_3^-, and associated negative cluster ions $NO_3^-(HNO_3)_n$, $NO_3^-(H_2O)_n$, and $NO_3^-(HCl)(HNO_3)_n$ [*Arnold and Henschen*, 1978]

Situated between the oversimplified electron-only approach and the complete description of atmospheric ion chemistry are those approaches which reduce the number of constituents by using only dominant species or by combining several ions into a representative effective species. *Mitra and Rowe* [1972] proposed one such 7-species model of D-region chemistry consisting of only e^-, NO^+, O_2^+, O_4^+, $H(H_2O)_n^+$, O_2^-, and a heavy negative ion presumed to be $NO_3^-(H_2O)_n$. Going a step further *Glukhov et al.* [1992] developed a 4-species model for D-region chemistry which combined all ion species into one of three categories: light positive ions (the density of which is written N^+ and which is comprised mostly of O_2^+ and NO^+), light negative ions (N^-, consisting mostly of O_2^- and O^-), heavy positive ions (N_x^+ such as the hydrate clusters of the species comprising N^+) and electrons (N_e). *Pasko and Inan* [1994] showed that this approach can be successfully used to predict the recovery signatures from most LEP events because the precipitating electrons typically deposit their energy at higher D-region altitudes (discussed in detail in Section 3.2) where the electron density dominates all chemical interactions.

However, precipitating MeV electrons deposit their energy at lower altitudes (e.g., 40–70 km) and other work [*Inan et al.*, 1988b] has predicted that the recovery signature due to these electrons is significantly shorter than for typical LEP events. Because the 4-species chemical model tends to overestimate electron densities at altitudes $\lesssim$70 km, *Lehtinen and Inan* [2007] added a fifth species of heavy negative ions (N_x^- such as NO_3^- and its hydrate clusters $NO_3^-(HNO_3)_n$) to extend the validity of the chemistry model to stratospheric altitudes.
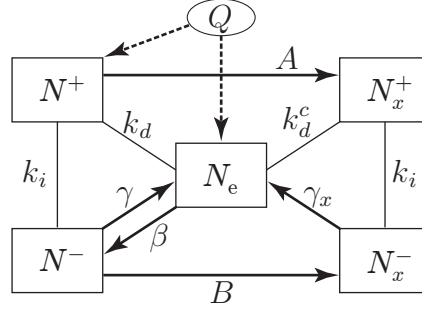
Figure 2.1: Schematic representation of the D-region ion chemistry considered in this dissertation, consisting of five different charged particle species and interactions among them.

The relationships among these species are determined by effective coefficients representing the rates of various chemical reactions as shown in Figure 2.1, and the density of each species is determined by the set of coupled differential equations shown below.

$$\frac{dN_e}{dt} = Q - \beta N_e + \gamma N^- + \gamma_x N_x^- - (k_d N^+ + k_d^c N_x^+)N_e \tag{2.1a}$$

$$\frac{dN^-}{dt} = \beta N_e - \gamma N^- - k_i(N^+ + N_x^+)N^- - A_1 N^- \tag{2.1b}$$

$$\frac{dN_x^-}{dt} = -\gamma_x N_x^- - k_i(N^+ + N_x^+)N_x^- + A_1 N^- \tag{2.1c}$$

$$\frac{dN^+}{dt} = Q - k_d N_e N^+ - k_i(N^- + N_x^-)N^+ - A_2 N^+ \tag{2.1d}$$

$$\frac{dN_x^+}{dt} = -k_d^c N_e N_x^+ - k_i(N^- + N_x^-)N_x^+ + A_2 N^+ \tag{2.1e}$$

The species are as defined above. $Q = Q_0 + Q(t)$ is the total ionization source comprised of the steady state ionization due to cosmic radiation, Q_0, and the production of secondary ionization by precipitating electrons, $Q(t)$. The effective electron attachment rate is β while γ and γ_x are the electron detachment rates from N^- and N_x^-, respectively. Furthermore, k_d is the effective coefficient of dissociative electron recombination with N^+, k_d^c is the effective recombination coefficient of electrons with

N_x^+, and k_i is the effective coefficient of mutual neutralization between the various ion species. Note that in contrast to past work, all recombination/neutralization coefficients are represented by the variable k in favor of α to avoid confusion with the electron pitch angle. Finally the conversion rates from light to heavy ions (i.e., hydration and other clustering processes) are A_1 and A_2 for negative and positive ions respectively. Note that these variables are chosen in favor of A and B (as used in previous work) to avoid confusion with the magnetic field strength.

There is some significant variability in the rate coefficients above and not all of the coefficients are well known due to the difficulties of making measurements in the D-region. However, the following rates have been used with success in past work for stratospheric and D-region ionization [*Glukhov et al.*, 1992; *Pasko and Inan*, 1994; *Lehtinen and Inan*, 2007].

The three-body attachment rate β (describing reactions $e^- + O_2 + N_2 \rightarrow O_2^- + N_2$ and $e^- + 2O_2 \rightarrow O_2^- + O_2$) is taken [*Rowe et al.*, 1974] to be:

$$\beta = 10^{-31} N[O_2] N[N_2] + 1.4 \times 10^{29} \left(300/T\right) e^{-(600/T)} N[O_2]^2 \qquad [s^{-1}] \qquad (2.2)$$

where $N[N_2]$ and $N[O_2]$ are atmospheric number densities of molecular nitrogen and oxygen (as a function of height) and T is the electron temperature. In the presence of an electric field there is an additional detachment term involving a two-body chemical reaction [*Pasko et al.*, 1997] which is disregarded in the current study.

The electron detachment rate is far less certain than the attachment rate and can vary by as much as a few orders of magnitude with small variations in neutral temperature T_n [*Pasko and Inan*, 1994]. Based upon the work of *Kozlov et al.* [1988] and *Alexandrov et al.* [1997], the detachment coefficient is approximated as:

$$\gamma \simeq 8.6 \times 10^{-10} e^{-(6000/T)} N + 2.5 \times 10^{-10} N_{ac} + \gamma_p \qquad [s^{-1}] \qquad (2.3)$$

where N is the total atmospheric neutral density and N_{ac} is the combined neutral density of oxygen, nitrogen, and singlet delta oxygen (molecular oxygen with an electron in a specific excited energy state): $N_{ac} = N[O] + N[N] + N[O_2(a^1\Delta_g)]$. The first term in Equation (2.3) is determined by the O_2^- electron affinity of 0.43 eV

[*Herzenberg*, 1969] and it is this dependence which makes γ uncertain to within a few orders of magnitude [*Pasko and Inan*, 1994]. The second term is most important above $\sim$70 km and involves the singlet delta oxygen molecule detaching an electron from either O^- or O_2^-. Finally the third term, γ_p, is due to the photo-detachment of electrons due to solar radiation and has a constant value taken to be $\sim$0.44 s^{-1} [*Lehtinen and Inan*, 2007, and references therein], but is disregarded in this study as all observations of LEP events occur at night. Likewise, solar radiation is the only source of ionization strong enough to detach an electron from the highly electronegative N_x^- species (e.g., the electron affinity of NO_3^- is 3.91 eV) and γ_x takes a constant value of 0.002 s^{-1} during the daytime [*Reid*, 1979] and $\gamma_x = 0$ s^{-1} at night. Finally, A_1 takes a value between $3 \times 10^{-20} N$ s^{-1} and $10^{-18} N$ s^{-1} [*Lehtinen and Inan*, 2007] and the counterpart for positive ions is A_2 which takes the value of $A_2 = 10^{-31} N^2$ s^{-1} [*Mitra*, 1975].

The calculation of the chemical relaxation is necessary but not sufficient to determine the recovery time of an observed LEP event. The observed recovery can in general depend on many factors including those described in Section 2.1.1 with regard to the magnitude of VLF amplitude and phase perturbations. A determination of the full recovery characteristics would require the full FDFD or full wave modeling effort required for finding the event magnitude at each time-step of recovery and is thus beyond the current global/statistical study.

An alternative is to use waveguide mode theory to calculate the electric field profile of each propagating mode and then calculate the absorption to determine the recovery time as in *Lehtinen and Inan* [2007]. However because the data comparison herein is statistical in nature this approach is not suited to the current work because the recovery time depends significantly on the ambient ionospheric density profile, and because the location of the ionospheric disturbance region is not known a priori. To mitigate the unknown location of the ionospheric disturbance the best solution method is to calculate the change in electron density relative to the ambient electron density profile (i.e., $\Delta N_e / N_{e0}$). This solution method is the best approach because it is independent of disturbance location or modal composition and determines, to first order, the recovery time of the LEP event [*Pasko and Inan*, 1994].

Since the recovery time is so strongly dependent on the relative change in ionospheric conductivity, the recovery time is determined by calculating $\Delta N_\mathrm{e}/N_\mathrm{e0}$ between the altitude where $\Delta N_\mathrm{e}/N_\mathrm{e0}$ is maximum to 5 km above this altitude.

2.1.3 Onset Delay (Δt)

The onset delay is defined as the time between when the causative lightning flash occurs to when the amplitude/phase of the signal begins to change (the 10% change point). Physically, the onset delay is the time required for the lightning-generated EMP to propagate in the Earth-ionosphere waveguide, couple through the ionosphere into the magnetosphere, propagate as a whistler mode wave, interact with a distribution of trapped radiation-belt electrons (at or near the magnetic equator), for the electrons to finish traversing the magnetic field line, impact the ionosphere where they cause secondary ionization.

In contrast to the previous two characteristics (ΔA and t_r) where the deposition of ionization into the atmosphere was just the first step in determining the LEP characteristic. Provided there is sufficient ionization to perturb a subionospherically propagating VLF signal, determination of the onset delay does not require any modeling beyond determining when the ionization is initially incident upon the atmosphere. Past work undertaking this calculation [*Inan et al.*, 1988a; *Lauben et al.*, 1999; *Bortnik et al.*, 2006a,b] and its application [*Johnson et al.*, 1999; *Peter and Inan*, 2007] have consistently underestimated the onset delay by ∼0.3 s, and the inclusion of atmospheric backscatter (described in subsequent chapters) discusses how this discrepancy can be addressed.

2.1.4 Onset Duration (t_d)

The onset duration is defined as the time between the 10% and 90% change in amplitude and is determined by the time over which the precipitating electrons continue to impact the ionosphere, causing secondary ionization. Initial modeling estimates for the onset duration are also shorter than observed LEP characteristics (0.3 s compared to 0.6 s [e.g., *Inan et al.*, 1988b]). This discrepancy was attributed to the cold

plasma density variation, the trapped particle distribution energy spectrum and the whistler frequency spectrum. However atmospheric backscatter can also account for this discrepancy as discussed in subsequent chapters.

2.2 Additional LEP Event Properties

In addition to the properties discussed in the previous section there are some parameters which have not been sufficiently addressed in past work and which are critical for determining the global contribution of lightning to radiation belt electron loss. These dependencies are the primary subject of the contributions of this research and are introduced below.

2.2.1 Grazing Incidence vs. Deep Incidence

In this dissertation electron pitch angles are quoted at various altitudes: 100 km, 150 km, and 200 km as well as at the geomagnetic equator. To differentiate between these locations, the pitch angle indicates the location (altitude) as a subscript. For example an electron with an equatorial pitch angle of 13° is written $\alpha_{\mathrm{eq}}{=}13°$, while (at some longitude) at a 200 km altitude the same electron may be represented as $\alpha_{200\mathrm{km}}{=}78°$, or at 100 km as $\alpha_{100\mathrm{km}}{=}90°$. If no altitude is indicated or if the pitch angle is written α_0 (for the initial pitch angle), then it is assumed that the altitude is 200 km. Although earlier work recognized the importance of atmospheric backscatter and crudely modeled it [*Imhof et al.*, 1985; *Inan et al.*, 1989], the inclusion of the effect of atmospheric backscatter has been ignored for simplicity in recent modeling work [e.g., *Peter and Inan*, 2007] where it was assumed that at 100 km the atmosphere is sufficiently dense that if an electron reaches this altitude it is precipitated [e.g., *Walt*, 2005].

The problem with this assumption is that it treats all electrons inside the loss cone as the same regardless of the actual pitch angle. This situation is shown qualitatively in Figure 2.2 and is an incorrect assumption because an electron which mirrors

at exactly 100 km (i.e., $\alpha_{100\text{km}} = 90°$) likely loses very little energy due to atmospheric interactions compared to an electron which is deeper inside the loss cone (i.e., $\alpha_{100\text{km}} = 70°$). The physical reason for this difference is that the loss of an electron from the radiation belts is based on the probability of that electron experiencing a sufficient number of inelastic collisions with atmospheric constituents such that it loses all of its energy. An electron which mirrors at 100 km only briefly interacts with the dense portion of the atmosphere while an electron which has a pitch angle of 70° at 100 km ($\alpha_{100\text{km}} = 70°$) penetrates much deeper into the atmosphere and therefore experiences many atmospheric interactions. Each atmospheric elastic scattering interaction results in only a small pitch angle deflection [*Lehtinen et al.*, 1999] so that it takes many interactions before the electron can have a high enough pitch angle to mirror and return to the magnetosphere. Furthermore, numerous elastic scatterings also imply numerous inelastic scatterings. Although the inelastic scatterings are less frequent and the fractional energy loss in each inelastic scattering is small, they may (but not always, as discussed in Chapter 3) accumulate and thus lead to a significant total energy loss and an isotropization in pitch angle. While both example electrons ($\alpha_{100\text{km}} = 90°$ and $\alpha_{100\text{km}} = 70°$) can be considered lost from the radiation belts, the time (i.e., which atmospheric interaction) and location (i.e., which hemisphere) that the electrons deposit their energy is a strong function of the incident pitch angle.

The consideration of grazing incidence is of primary importance, since it has been demonstrated [*Inan et al.*, 1989] that the scattering which occurs in LEP events barely moves electrons from slightly above the loss cone to slightly below the loss cone. Thus, a burst of LEP electrons arriving at the atmosphere are initially always at grazing angles of incidence.

2.2.2 Geomagnetic (and thus Geographic) Location

In a perfect dipole field the observed characteristics of LEP events at the same latitude and different longitudes would be expected to be the same, with any (slight) differences attributed to systematic variations in the source lightning spectrum at the different locations or to differences in the GCP between the respective transmitters
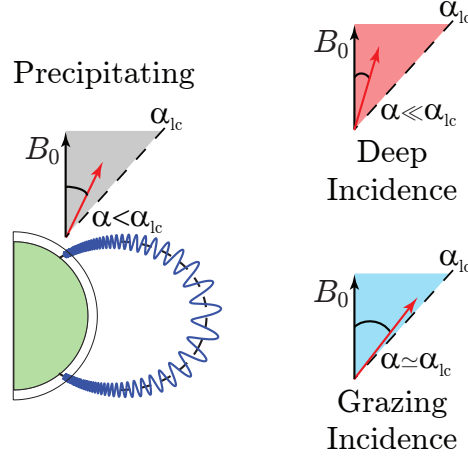
Figure 2.2: Schematic describing grazing versus deep incidence precipitating electrons.

and receivers. However, because the Earth's magnetic field is not a perfect dipole (rather it may be roughly approximated as an off-center, and tilted dipole) there are significant differences in the magnetic field as a function of longitude, the most well-known of which is the South Atlantic Anomaly [e.g., *Blake et al.*, 2001].

More relevant to this work is the manifestation of the magnetic field variation in the form of both longitudinal and hemispheric differences in the loss cone angles. The importance of these longitudinal and hemispherical differences in loss cone angle were first noted by *Inan et al.* [1988c] and were predicted to influence the occurrence rate and precipitated flux levels of LEP events. Figure 2.3a shows the difference in the equatorial loss cone angle for each hemisphere and its variation as a function of longitude at L=2.5. The loss cone —shown by the shaded region— is defined as the larger of the two hemispheric loss cone angles on any specific field line (conjugate longitudes are connected by the thin diagonal lines) and it is clear that equatorial electrons at varying longitudes behave very differently. The classic example is illustrated by comparison of two electrons with the same pitch angle (e.g., α_{eq}=16°) at longitudes of φ_1=0° **E** and φ_2=100° **E**. As shown by Figure 2.3a it is clear that the electron at φ_1 is inside the bounce loss cone while the electron at φ_2 is well outside the bounce loss cone, but inside the drift loss cone (the global maximum loss cone angle, taking into

account the eastward longitudinal drift of electrons [e.g., *Blake et al.*, 2001]).

Taking this scenario a step beyond the simple bounce loss cone example, consider an electron scattered to a pitch angle of $\alpha_{eq}=16°$ due to a south-going whistler wave launched by a lightning flash in the Northern Hemisphere. In this case the specific bounce motion of the first electron (at $\varphi_1=0°$ **E**) can again be differentiated. It is evident that a southward traveling (co-streaming) electron scattered to a pitch angle of $\alpha_{eq}=16°$ penetrates below 100 km and interacts with the atmosphere (possibly backscattering). On the other hand a northward traveling (counter-streaming) electron scattered to a pitch angle of $\alpha_{eq}=16°$ is far above the northern loss cone. This northward traveling electron does not interact with the northern atmosphere, but instead mirrors in the north (well above 100 km) and returns to the Southern Hemisphere where it interacts with the atmosphere.

In order to discuss these differences in the remainder of this dissertation it is necessary to introduce some new terminology. An electron which is below the southern loss cone, but above the northern loss cone (e.g., at $\varphi=0°$ and $\alpha_{eq}=16°$) is 'half-trapped' above the northern hemisphere atmosphere. Likewise, an electron which is below the northern loss cone, but above the southern loss cone (e.g., at $\varphi=200°$ and $\alpha_{eq}=11°$) is half-trapped above the southern hemisphere atmosphere.

Finally, as shown in subsequent sections, the difference between the two loss cones at conjugate points of the same field line plays a large role in determining the location (i.e., which hemisphere) of LEP precipitation as well as the temporal evolution (i.e., which atmospheric interaction) of the precipitation signature. Figure 2.3b shows this difference explicitly where $\Delta\alpha_{eq}^{lc} = \alpha_{eq,\mathbf{S}}^{lc} - \alpha_{eq,\mathbf{N}}^{lc}$. For example, an electron which is pitch angle scattered by 0.2° (a fairly large equatorial pitch angle-scattering [*Bortnik et al.*, 2006a,b]) inside the loss cone at a longitude of $\varphi=0°$ is still half-trapped more than 4° above the northern loss cone, while an electron which is scattered 0.2° at a longitude of $\varphi=200°$ is inside both loss cones. Combining the effects of the loss cone variation with longitude and hemisphere as well as the properties of backscatter discussed in Section 3.3.3 allows the prediction of LEP event characteristics as a function of longitude and hemisphere.
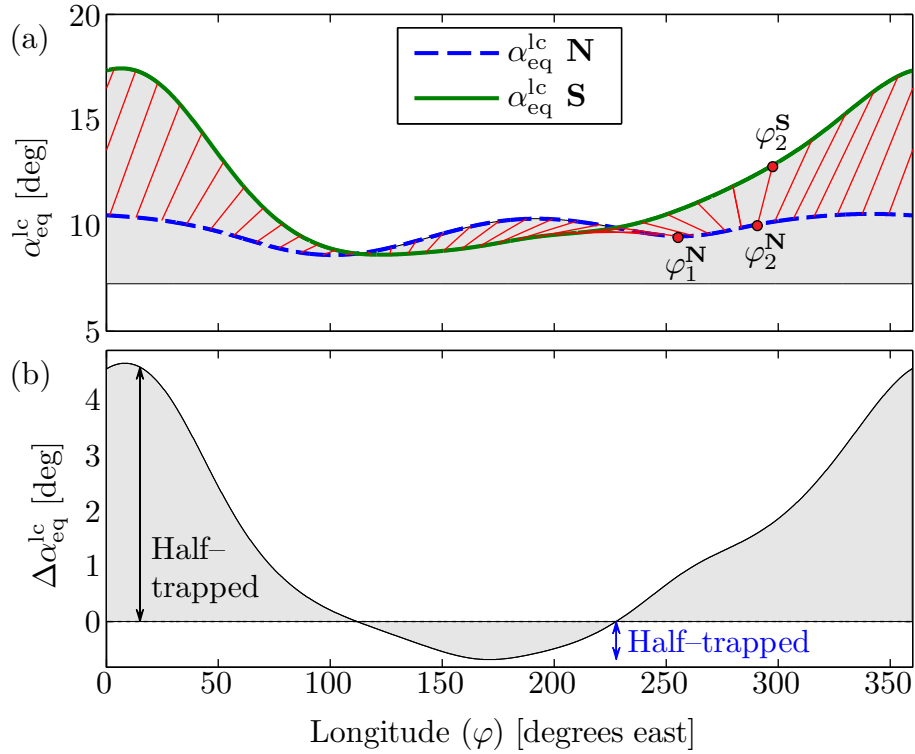
Figure 2.3: (a) Equatorial loss cone angle as a function of geographic longitude (φ). The thick dashed line indicates the loss cone angle in the Northern Hemisphere at an L-shell of 2.5 while the thick solid line indicates the loss cone angle in the Southern Hemisphere. The thin diagonal lines connecting the two curves (every 10°) indicate conjugate points of the same magnetic field line and the shaded region indicates the bounce loss cone. The small circles denote the locations (approximate) of the three regions for the experimental statistical study (Section 2.3.2). (b) Difference in equatorial pitch angle as a function of geographic longitude ($\alpha_{eq,\mathbf{S}}^{lc} - \alpha_{eq,\mathbf{N}}^{lc}$). The shaded region above zero indicates local pitch angles which are half-trapped above the Northern Hemisphere. The shaded region below zero indicates local pitch angles which are half-trapped above the Southern Hemisphere.

2.3   LEP Observations

A critical factor for linking the characteristics of LEP events to radiation belt electron loss is the observation of LEP events at different longitudes. This section briefly discusses the VLF receiver used in making the observations and then gives an overview of the three locations at which case study measurements are made.

2.3.1   The VLF Receiver

The receiver system used in acquiring data for the LEP observations is known as the AWESOME receiver (Atmospheric Weather Electromagnetic System for Observation, Modeling and Education) the details of which are reported in detail by *Cohen et al.* [2010]. The original array of receivers used for detecting D-region ionization due to lightning (consisting of several predecessors to the AWESOME receiver) was deployed along the eastern edge of the Rocky Mountains in the Central United States and is known as Holographic Array for Ionospheric Lightning (HAIL) [*Johnson et al.*, 1999; *Peter and Inan*, 2004]. Each VLF receiver in the HAIL array is deployed at a rural high school or community college with data sent back to Stanford daily for expedient data analysis. The deployed receiver is divided into indoor and outdoor components. Outside there is a GPS antenna which provides exact timing resolution so that receivers in all locations sample at exactly the same time. Additionally, the basic receiving apparatus is either a single, or an orthogonal pair of triangular (1.6 m height by 3.2 m base) air-core magnetic loop antenna(s) connected to a preamplifier which provides basic signal conditioning (high pass filtering for mitigating power line interference) and amplification. The signal from the preamplifier is transmitted inside over a long cable (up to 700 m) to the line receiver inside. The line receiver provides anti-aliasing filtering and passes the conditioned signal to a nearby computer for sampling and saving. The broadband VLF signal is digitized at a sampling rate of 100 kHz with 16-bit resolution and the individual VLF transmitter signals are extracted in software by mixing down each Minimum Shift Keying (MSK) signal to baseband and extracting the demodulated amplitude and phase used for identifying the characteristics of LEP events.
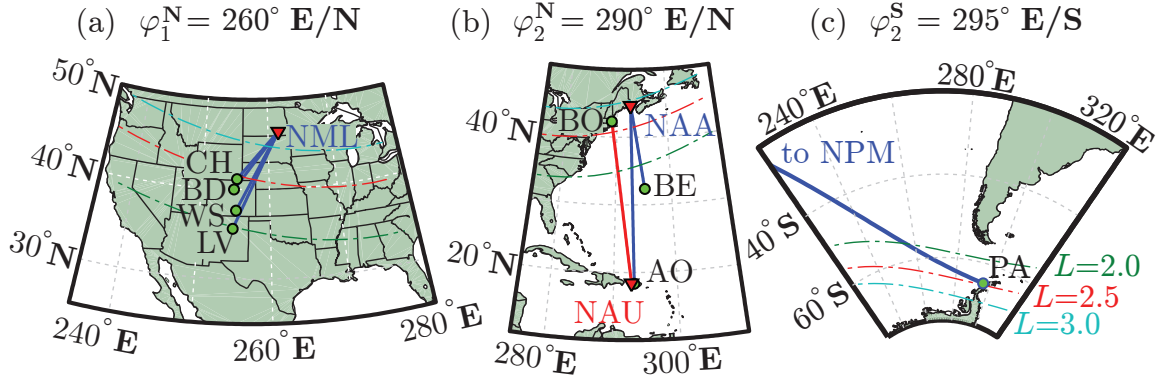
Figure 2.4: Maps showing the experimental setup of the three locations under investigation. (a) Central United States: the NML transmitter signal (25.2 kHz) received at the HAIL receivers in Wyoming, Colorado and New Mexico. (b) East Coast of the United States: the NAA (24 kHz) and NAU (40.75 kHz) transmitter signals received at Boston, MA, Arecibo, PR and Bermuda. (c) Palmer Antarctica: the NPM (21.4 kHz in HI) transmitter signal received at Palmer Station, Antarctica.

2.3.2 Case Studies: LEP Events at Different Longitudes

Previous studies of LEP event characteristics in the United States have primarily used the NAA (24.0 kHz in Maine) and the NAU (40.75 kHz in Puerto Rico) transmitters because the lightning occurrence rate in the Central and Eastern United States is quite high and the observation of LEP events is quite prevalent [*Johnson et al.*, 1999; *Peter and Inan*, 2004, 2007]. In the current study, however, it is important to isolate the longitudinal dependencies of the LEP events, and therefore it is important to select only GCPs which are located along a limited longitude range. The choice of location is primarily determined by the location of VLF transmitters and receivers available for comparison. The three primary areas of interest for the longitudinal/hemispherically varying LEP characteristics are $\varphi_1 = 260°$ **E/N**, $\varphi_2 = 290°$ **E/N**, and $\varphi_3 = 295°$ **E/S**. These longitudes correspond to the geographic location of transmitter and receiver pairs used for data comparison (shown in Figure 2.4 and discussed further in Section 5.1). For reference the geographic location of and call sign (name) of indicated transmitters (receivers) are shown in Table 2.1.

Group	Symbol	Name/Freq	Latitude (λ)	Longitude (φ)
$\varphi_1^{\mathbf{N}}$	NML	25.2 kHz	46.366°	261.665°
	CH	Cheyenne	41.1468°	255.2219°
	BD	Boulder	39.9718°	254.8156°
	WS	Walsenburg	37.6326°	255.2091°
	LV	Las Vegas	35.5954°	254.7792°
$\varphi_2^{\mathbf{N}}$	NAA	24.0 kHz	44.646°	292.719°
	NAU	40.75 kHz	18.399°	292.822°
	BO	Boston	42.4540°	288.7274°
	BE	Bermuda	32.2788°	295.2237°
	AO	Arecibo	18.3472°	293.2457°
$\varphi_2^{\mathbf{S}}$	NPM	21.4 kHz	21.420°	201.846°
	PA	Palmer Station	−64.7746°	295.9492°

Table 2.1: Transmitter (three-letter abbreviations) and receiver names (two-letter abbreviations) and locations.

Central United States: the HAIL Array

The first location (Figure 2.4a) uses GCPs between the NML transmitter and the HAIL array located in the Central United States. The longitude of the NML transmitter (25.2 kHz in North Dakota) is just a few degrees east of the HAIL receivers (the midpoint rounded to $\varphi_1^{\mathbf{N}}$=260° **E/N**). This location is ideal for observations because the northern and southern hemispheric loss cones are relatively close together ($\Delta\alpha_{\mathrm{eq}}^{\mathrm{lc}} \simeq 0.4°$) and because of the prevalence of lightning in Texas which produces LEP events in the desired location. In addition, the region conjugate to 260° **E/N** is in the middle of the Pacific Ocean and therefore the possibility of causative lightning coming from the Southern Hemisphere is quite low [e.g., *Christian et al.*, 2003].

East Coast of the United States

The second location is the East Coast of the United States, using GCPs between the NAA (24.0 kHz in Maine) and NAU (40.75 kHz in Puerto Rico) transmitters and VLF receivers in Boston, Massachusetts, Arecibo, Puerto Rico, and Bermuda as shown in Figure 2.4b. This set of transmitters and receivers is also clustered nicely along a

limited longitude range (the midpoint rounded to $\varphi_2^{\mathbf{N}}$=290° $\mathbf{E/N}$) and is a good contrast to the Central United States because the difference between the hemispheric loss cones is much larger than at $\varphi_1^{\mathbf{N}}$ (i.e., here $\Delta\alpha_{\mathrm{eq}}^{\mathrm{lc}} \simeq 1.5°$). Finally, as with $\varphi_1^{\mathbf{N}}$, there is a high occurrence rate of lightning in the Northern Hemisphere and a very low occurrence rate of lightning at the conjugate point meaning the vast majority of observed LEP events are caused by northern hemispheric lightning.

Southern Hemisphere Conjugate Location

The last region is comprised of the GCP between the NPM transmitter (21.4 kHz in Hawaii) and Palmer Station, Antarctica shown in Figure 2.4c. Both because this region is quite close to the conjugate point of φ_2, and because the predicted differences in southern hemispheric deposition are negligible at these longitudes (as shown in Section 3.6) it is sufficient to take the third region to be the conjugate point of $\varphi_2^{\mathbf{N}}$: $\varphi_2^{\mathbf{S}}$=295° $\mathbf{E/S}$. Finally, because the nearest land mass to this GCP is more than 10° equatorward in latitude it is highly unlikely that observed LEP events are due to southern hemispheric lightning [*Johnson et al.*, 1999; *Lauben et al.*, 1999; *Peter and Inan*, 2004].

2.4 Summary

This chapter has presented the necessary background for understanding the expected longitudinal differences in LEP event characteristics and has described the experimental setup for evaluating these differences. It is now possible to discuss the model of atmospheric backscatter which can be used to quantitatively predict the characteristics of LEP events at the three locations ($\varphi_1^{\mathbf{N}}$, $\varphi_2^{\mathbf{N}}$, and $\varphi_2^{\mathbf{S}}$) and to evaluate the role of radiation belt electron loss due to lightning as a function of longitude.

Chapter 3

Model of Atmospheric Backscatter

The Atmospheric Backscatter (ABS) model is comprised of a tabulated atmospheric backscatter response for any electron distribution defined by a grid of ~16,000 initial pairs of $(\mathcal{E}_0, \alpha_0)$ in the range $\mathcal{E}_0 \in [.05, 30]$ MeV (98 energies spaced roughly logarithmically) and $\alpha_0 \in [0°, 90°]$ (55 pitch angles spaced every 5° from 0°–25°, every 2.5° from 27.5°–75° and every 0.5° from 76°–90°). The ABS model also encompasses three separate magnetic dip angles —the angle between the horizontal plane and the vertical component of the magnetic field— of 63°, 68° and 72°. The chosen sampling in pitch angle maximizes the resolution of atmospheric effects on electrons with pitch angles near the loss cone (where the greatest variation in backscatter distributions occur, as shown in Sections 3.2 and 3.3.1).

A schematic representation of the input and output is shown in Figure 3.1 where each of the n incident electrons comprising the input 'beam' has the same initial energy and pitch angle $(\mathcal{E}_0, \alpha_0)$ as shown by the downward-opening cone in red. The backscattered distribution of electrons —each with a different backscattered energy and pitch angle $(\mathcal{E}_k, \alpha_k)$— is shown by the upward-opening cone in green where each backscattered electron has lost some energy $\Delta\mathcal{E} = \mathcal{E}_0 - \mathcal{E}_k \geq 0$ and has diffused somewhat in pitch angle $(\Delta\alpha)$. The energy lost $(\Delta\mathcal{E})$ is deposited into the atmosphere in the form of secondary ionization and the remaining electrons comprise the atmospheric backscatter response to the monoenergetic, monodirectional beam of precipitating electrons. The characteristic deposition profile $N_{e0}(\mathcal{E}_0, \alpha_0 | h)$, and backscatter
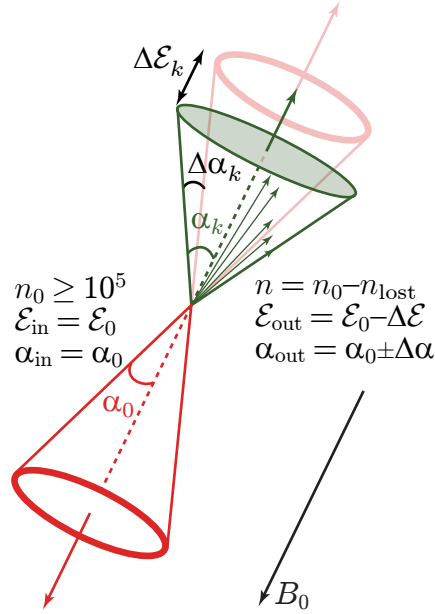
Figure 3.1: Schematic representation of the monoenergetic, monodirectional input beam of electrons and the backscattered distribution, $\Psi_0(\mathcal{E}_0, \alpha_0 | \mathcal{E}, \alpha)$.

distribution $\Psi_0(\mathcal{E}_0, \alpha_0 | \mathcal{E}, \alpha)$ can be calculated by observing the total energy loss and the properties of individual backscattered electrons.

In the remainder of this dissertation, the complete set of specifically calculated deposition profiles and backscatter distributions are represented as: $N_{e\mathbf{M}}(\mathcal{E}_0, \alpha_0 | h)$ and $\Psi_{\mathbf{M}}(\mathcal{E}_0, \alpha_0 | \mathcal{E}, \alpha)$, respectively, where the '$\mathbf{M}$' denotes Monte Carlo simulations (discussed in Section 3.1). Individual deposition profiles are represented as: $N_{e0}(\mathcal{E}_0, \alpha_0 | h)$ and individual backscatter distributions are represented as $\Psi_0(\mathcal{E}_0, \alpha_0 | \mathcal{E}, \alpha)$. The deposition profile or backscatter distribution for any initial pair $(\mathcal{E}_0, \alpha_0)$ not specifically calculated is represented as $N_{e0}(\mathcal{E}_i, \alpha_j | h)$ and $\Psi_0(\mathcal{E}_i, \alpha_j | \mathcal{E}, \alpha)$ and can be easily and accurately interpolated using the distribution for surrounding pairs as explained in Appendix A.

The notation for deposition profiles and backscatter distributions is shorthand and needs further explanation. $N_{e0}(\mathcal{E}_0, \alpha_0 | h)$ is the number of free electrons created in the atmosphere, evaluated as a function of altitude (h), and normalized to the precipitation of one electron per unit area, incident with an initial energy and pitch

angle described by $(\mathcal{E}_0, \alpha_0)$. Similarly, $\Psi_0(\mathcal{E}_0, \alpha_0|\mathcal{E}, \alpha)$ specifies the backscattered electron distribution for the incident energy and pitch angle $(\mathcal{E}_0, \alpha_0)$ as well as a backscattered energy and pitch angle $(\mathcal{E}, \alpha)$ (per unit of backscattered energy and solid angle), on which the function is evaluated. The distribution represents the fluence of backscattered electrons as a function of both (backscattered) energy and pitch angle, normalized to the precipitation of one electron per unit area incident with an initial energy and pitch angle described by $(\mathcal{E}_0, \alpha_0)$. The output (backscattered) energy is typically evaluated either on an absolute energy grid which is uniformly spaced between 0–$\mathcal{E}_0$ or on a normalized energy grid $(x = \mathcal{E}/\mathcal{E}_0)$ which is uniformly spaced between 0–1. The default output pitch angle is evaluated on a grid which spans the range of $0°$–$90°$ and is spaced so that the solid angle $\Omega = 2\pi(1 - \cos\alpha)$ is spaced linearly on the 0–2π interval. The reason for choosing the variable Ω instead of α is explained in the discussion of Section 3.3.1. A distribution which is evaluated on an absolute energy grid is represented $\Psi_0(\mathcal{E}_0, \alpha_0|\mathcal{E}, \alpha)$ while the same distribution evaluated on a normalized energy grid is represented $\Psi^{\mathrm{norm}}(\mathcal{E}_0, \alpha_0|x, \alpha)$.

To fully understand the importance of atmospheric backscatter for the observation of LEP events it is necessary to quantify both $N_{\mathrm{e}0}(\mathcal{E}_0, \alpha_0|h)$ and $\Psi_0(\mathcal{E}_0, \alpha_0|\mathcal{E}, \alpha)$, as a function of input energy and pitch angle. $N_{\mathrm{e}0}(\mathcal{E}_0, \alpha_0|h)$ is necessary because it is the newly introduced ionization which is detectable using VLF remote sensing, and $\Psi_0(\mathcal{E}_0, \alpha_0|\mathcal{E}, \alpha)$ —which can be observed by a particle-detector on-board a satellite in low-earth orbit [e.g., *Voss et al.*, 1984]— is necessary because it determines the temporal (i.e., which atmospheric interaction) and spatial (i.e., which hemisphere) evolution of the backscattered electrons.

3.1 Monte Carlo Simulations

The interaction of precipitating electrons with the neutral atmosphere is inherently a stochastic process and is therefore well suited to modeling with a Monte Carlo simulation. The Atmospheric Backscatter model detailed in this chapter is based upon the Monte Carlo model developed by *Lehtinen et al.* [1999] and tracks the full gyration of each individual precipitating electron around the magnetic field line as it

enters the atmosphere, accounting separately for inhomogeneity of **B** (responsible for mirroring), the dynamic friction force and angular diffusion, as well as the production of new (relativistic) electrons via ionization. Additionally the Monte Carlo model accounts for the effects of a geomagnetic field of arbitrary dip angle orientation making it suitable for calculations at all mid-latitude L-shells and longitudes. The ABS model begins simulation of atmospheric interaction at an altitude of 200 km so that the atmospheric effects on electrons above (but still near) the loss cone can also be evaluated.

The production of electrons in the atmosphere is calculated in the Monte Carlo model using the dynamic friction force [*Bethe and Ashkin*, 1953, p. 254] which acts in a direction opposing the electron motion and includes energy losses due to both excitation and ionization. Depending on the nature of the atmospheric collision, the ionizing collision can create either relativistic electrons which themselves become part of the simulated electron population, or non-relativistic electrons which act as free electrons in the ionospheric plasma and change the conductivity of the ionosphere. These two forces are accounted for separately in the Monte Carlo simulation by subtracting losses due to the production of relativistic electrons (calculated with an energy-dependent scattering cross section [*Bethe and Ashkin*, 1953, p. 277]) from the dynamic friction force as discussed in *Lehtinen* [2000, Ch. 2].

The production of new relativistic electrons and electron backscatter are discussed in Section 3.3.1, with the remaining energy losses contributing to the production of low energy (non-relativistic) secondary ionization. These non-relativistic free electrons produced as secondary ionization are discussed in Section 3.2 and contribute to changes in ionospheric conductivity (i.e., a deposition profile) which can be observed using VLF remote sensing as discussed in Section 1.1.1.

3.2 Atmospheric Deposition Profiles: $N_{e0}(\mathcal{E}_0, \alpha_0|h)$

The production of secondary ionization (free electrons) in the atmosphere is calculated in terms of energy deposited at each altitude. This energy deposition is then converted to an electron density profile using the often-quoted factor of one electron-ion pair

created for every 35 eV of electron energy [*Rees*, 1963]. Previous studies [e.g., *Peter and Inan*, 2007; *Chevalier et al.*, 2007] have used a similar (Monte Carlo) approach to determine the altitude profile of secondary ionization created by precipitating electrons. However, these studies emphasized the energy of the electron, ignoring the equally important contribution of incident pitch angle, or accounting for it only in a generalized sense (i.e., by assuming a specific initial pitch angle distribution).

In the remainder of this dissertation, unless otherwise specified, the energy and pitch angle pairs ($\mathcal{E}_0$, α_0) are assumed to be in units of MeV and degrees, respectively, where the pitch angle is specified at an altitude of 200 km (i.e., α_{200km}). For reference, $\alpha_{100km}=90°\leftrightarrow\alpha_{200km}=78°$, meaning that electrons $\lesssim78°$ at an altitude of 200 km are inside the conventionally-defined loss cone (i.e., mirror at or below 100 km altitude) while those electrons $\gtrsim78°$ at 200 km altitude are outside the loss cone.

Figure 3.2 illustrates the basic dependence of the deposition profile, $N_{e0}(\mathcal{E}_0, \alpha_0|h)$, on incident pitch angle and energy. Figure 3.2a shows $N_{e0}(\mathcal{E}_0, \alpha_0|h)$ for three different energies at one pitch angle and illustrates two key points. The higher the energy of the incident electrons, the deeper they penetrate into the atmosphere and the more secondary ionization they create. The peak value of $N_{e0}(\mathcal{E}_0=0.1\,\text{MeV}, \alpha_0=0°|h)$ is ~0.4 cm^{-3} at an altitude of $h \sim 80$ km while the peak of $N_{e0}(\mathcal{E}_0=0.3\,\text{MeV}, \alpha_0=0°|h)$ is located at $h \sim 70$ km with a peak deposition of ~1 cm^{-3} and the peak of $N_{e0}(\mathcal{E}_0=1.0\,\text{MeV}, \alpha_0=0°|h)$ is at $h \sim 60$ km with a peak deposition of ~3 cm^{-3}.

Figure 3.2b shows $N_{e0}(\mathcal{E}_0, \alpha_0|h)$ for three different incident pitch angles ($\alpha_0=0°$, 70°, and 80°) at the same energy ($\mathcal{E}_0=0.3$ MeV). Note that the deeper angles of incidence result in $N_{e0}(\mathcal{E}_0, \alpha_0|h)$ with higher peak ionization which are narrowly peaked. Despite the different shape of the deposition profiles, Figure 3.2b shows that the amount of deposition (for electrons incident below the loss cone angle) remains relatively unchanged as the incident pitch angle changes from 0° (directly down the magnetic field line) to 70° (grazing incidence), however, above the loss cone (80°) the deposition decreases dramatically, as expected. To quantify these characteristics more completely, Figure 3.3 shows deposition profiles for electrons with incident energy $\mathcal{E}_0$ ranging from 0.05 MeV–1.0 MeV and incident pitch angles (α_0 at 200 km) ranging from 0°–90°.
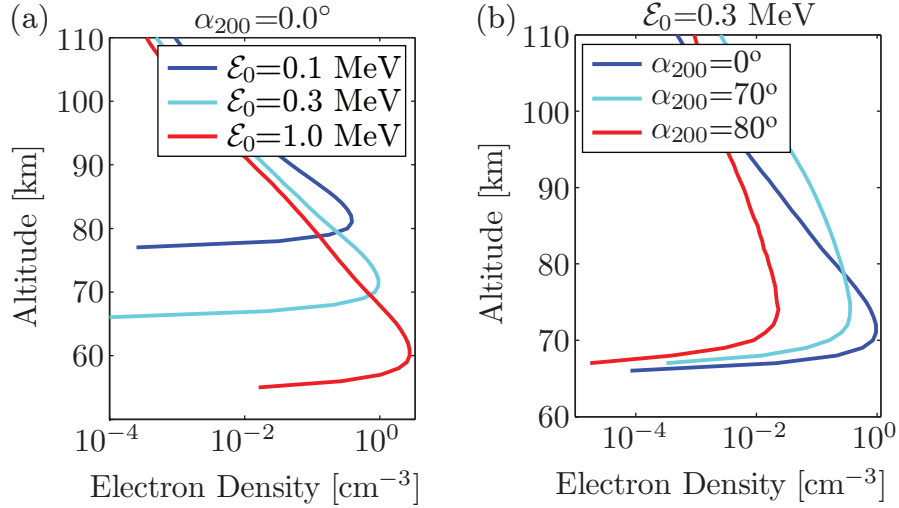
Figure 3.2: Simple deposition profiles showing the basic dependence of the created ionization on incident energy ($\mathcal{E}_0$) and pitch angle (α_0).

Figure 3.3 shows electron energy deposition profiles as a function of both incident energy and pitch angle. Each panel shows several $N_{e0}(\mathcal{E}_0, \alpha_0|h)$ profiles for a single incident pitch angle while the color of each line indicates the energy of the incident electrons, with values ranging from 0.05 MeV–1 MeV (corresponding to dark blue and dark red lines, respectively), and shown for reference by the color bar. Notice that matching previous numerical estimates [*Banks et al.*, 1974] (for electrons inside the loss cone), higher energy electrons deposit (i) more total energy per incident electron (while the fraction of deposited energy is a function of both the initial energy and pitch angle) and (ii) the peak deposition occurs at a lower altitude. This result is most easily seen in Figure 3.3a in which the peak of the 1 MeV deposition profile (shown in dark red) occurs at ∼60 km, whereas the peak of the 0.05 MeV deposition profile (shown in dark blue) occurs at ∼85 km. Furthermore, the peak ionization created is approximately one order of magnitude higher for the 1 MeV electron than the 0.05 MeV electron.

The dependence of the deposition profile on incident pitch angle is more subtle but is illustrated by comparing the different panels to one another. Notice first that the two energy-dependent features described above only hold true for precipitating
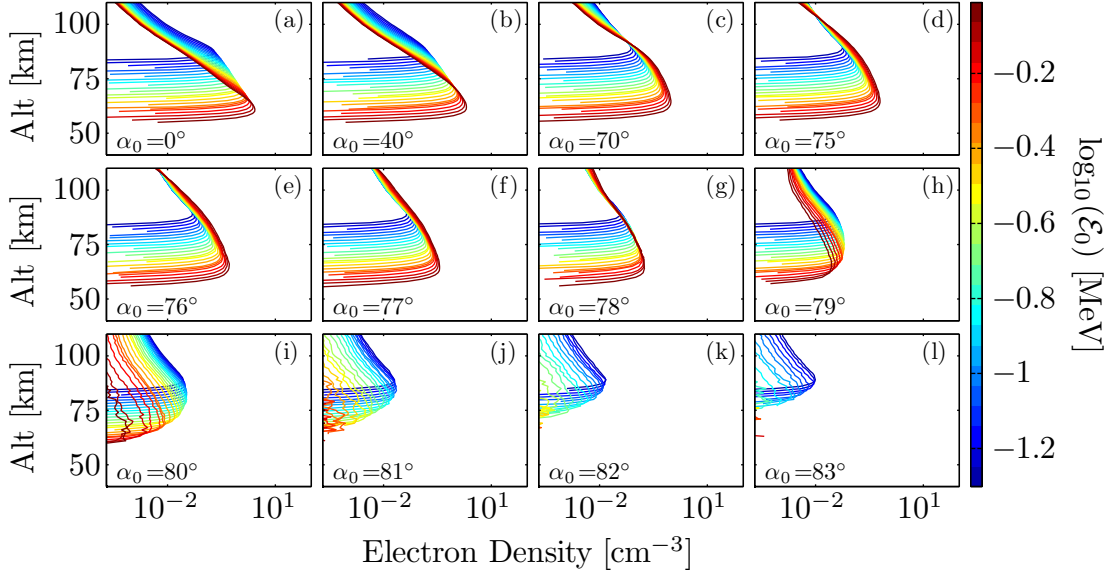
Figure 3.3: Electron deposition profiles vs. both $\mathcal{E}_0$ and α_0 (at L=2.5) normalized to a single electron of the specified energy and pitch angle per unit area. The abscissae are in units of electrons/cm^3 and the ordinates show the altitude in km. Each panel shows a different incident pitch angle ($\alpha_{200\text{km}}$, indicated at the bottom of the panel). Within each panel the color of each line indicates the incident energy of the precipitating electron with values ranging from 0.05 MeV (dark blue) to 1.0 MeV (dark red) as shown by the color bar displaying the $\log_{10}$ of the incident energy.

electrons with pitch angles below the loss cone angle as can be seen in Figure 3.3, panels (a) through (g); however, there are some interesting pitch angle dependent variations evident in the deposition profiles. Comparing panels Figure 3.3a and Figure 3.3c it is evident that while the deep incidence profile, $N_{\text{e}0}(\mathcal{E}_0\text{=0.3 MeV}, \alpha_0\text{=}0°|h)$, is narrowly peaked (with a 3 dB peak altitude range of 58–67 km) the altitude profile of $N_{\text{e}0}(\mathcal{E}_0\text{=0.3 MeV}, \alpha_0\text{=}70°|h)$, grazing incidence, has a much broader peak (with a 3 dB altitude range of 60–77 km), though the peak deposition is less by a factor of ~3. This fact has implications for both the magnitude [*Peter and Inan*, 2007] and recovery time [*Pasko and Inan*, 1994; *Lehtinen and Inan*, 2007] of observed LEP events as discussed in Sections 2.1.1 and 2.1.2. Finally, notice that above the loss cone angle of $\alpha_{200\text{km}}$=78°, $N_{\text{e}0}(\mathcal{E}_0, \alpha_0|h)$ alters significantly in two ways. i) The percentage of energy deposited decreases dramatically, and ii) the energy-dependent variation of

the deposition no longer exhibits the same characteristics as described above. While higher energy electrons still penetrate to lower altitudes, they deposit less of their energy (absolute deposition, not just relative) than the lower energy electrons.

In particular, at a pitch angle just above the loss cone ($\alpha_{200\text{km}} = 79°$) as shown in Figure 3.3h, incident electrons of all energies deposit roughly the same amount of energy (per km) at the peak of their respective profiles. In fact the largest peak in deposition occurs for precipitating electrons of $\sim$0.2 MeV and the peak deposition for 1 MeV electrons is approximately equal to the peak deposition for electrons of only 0.05 MeV (at altitudes of 67, and 89 km, respectively). This result is due to the energy-dependent dynamic friction force an electron experiences in the atmosphere, which has a minimum at $\sim$1.2 MeV [e.g., *Lehtinen et al.*, 1999]. This fact is especially important for precipitating electrons associated with LEP events of 0.1 MeV–0.3 MeV [*Voss et al.*, 1998; *Peter and Inan*, 2007] because it means that while proportionally more energy is initially deposited at these energies, there is also significantly more diffusion in pitch angle for those electrons which are backscattered from the atmosphere, as discussed in Section 3.3.1.

3.3   Atmospheric Backscatter of Electrons

This section focuses on electrons which remain after an atmospheric interaction i.e., those which are backscattered. Atmospheric backscatter can occur when the result of any individual atmospheric interaction leaves an electron with a local pitch angle $\geq$90°. The angular diffusion in electron pitch angle during an atmospheric interaction is dominated by elastic collisions with the nuclei of atmospheric constituents and while these interactions are quite frequent (below an altitude of $\sim$100 km), the change in pitch angle is very small. The angular diffusion is therefore calculated as a time rate of change in the mean squared scattering angle [*Lehtinen*, 2000, Eq. 2.13].

3.3.1 Backscattered Electron Characteristics

Similar to $N_{e0}(\mathcal{E}_0, \alpha_0 | h)$, the variation of $\Psi_0(\mathcal{E}_0, \alpha_0 | \mathcal{E}, \alpha)$ as a function of both $\mathcal{E}_0$ and α_0 reveals insight into the importance of input energy and pitch angle on the atmospheric backscatter distribution. However, while the deposition profiles show the altitude-dependent deposition of energy, the backscatter distributions show the energy and pitch angle of the backscattered electrons as a function of $(\mathcal{E}_0, \alpha_0)$. In this section, the discussion of backscattering is in terms of the fraction of total input energy backscattered (i.e., total number of electrons times individual electron energy divided by the total input energy), instead of electron number, because quantifying the number of backscattered electrons is not helpful as new relativistic electrons are created during the interaction process with the atmosphere. For example, for electrons well above the loss cone ($\alpha_{200km}=90°$) the ABS model predicts that there are more backscattered electrons than input electrons due to the production of new electrons during atmospheric collisions. However, due to conservation of energy, these backscattered electrons have only 99.9989% of the total input energy (the remaining small amount of energy being deposited in the rare atmospheric collision at 200 km).

Numerically determining the backscatter response of the atmosphere to one of these monoenergetic, monodirectional beams of precipitating electrons is more complicated than determining the deposition profile because the energy (or ionization) deposition profile is a function of only one variable (altitude), while the backscatter distribution is a function of two variables (energy and pitch angle).

Solid Angle vs. Pitch Angle Tabulation

It is instructive to begin the discussion of atmospheric backscatter by initially ignoring the backscattered energy and discussing the motivation to use a backscattered pitch angle grid which is linearly space in solid angle (Ω) instead of one linearly spaced in pitch angle (α). Figure 3.4a shows a histogram of backscattered electron pitch angle (with the histogram peak normalized to unity) for a beam of electrons incident at ($\mathcal{E}_0=$ 0.3 MeV, $\alpha_0=50°$). The bins in this histogram are linearly spaced in backscattered pitch angle (α_{200km}) between 0°–90° (up-going). This figure indicates two things
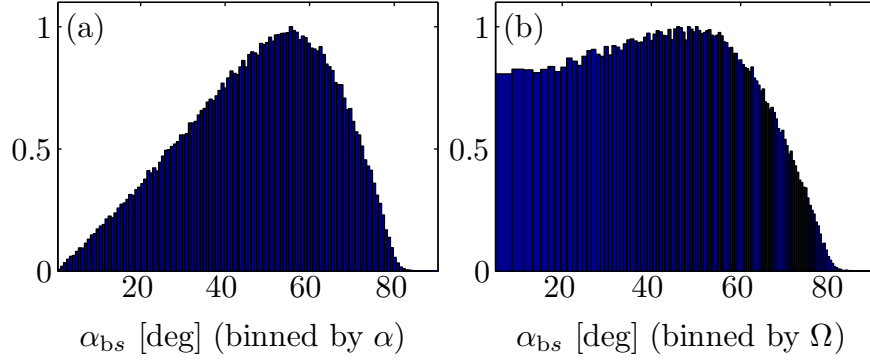
Figure 3.4: 1-D Histogram of backscattered electron pitch angle for ($\mathcal{E}_0 = 0.3\,\text{MeV}$, $\alpha_0{=}50°$). (a) Histogram with bins spaced linearly in pitch angle, α. (b) Histogram with bins spaced linearly in solid angle, Ω.

which are counter-intuitive. First, the most common backscattered pitch angle is at $\sim 55°$, and second the likelihood that an electron is backscattered with a specific pitch angle decreases approximately linearly from this peak to zero at $0°$. The first point is unexpected because the random change in pitch angle due to each atmospheric interaction should (on average) cancel out, so that the most likely backscattered pitch angle should be the input angle (though this is not necessarily the case for very deep incidence electrons). The second point is more troublesome because there is no physical reason that the likelihood of a particular backscattered pitch angle should decrease linearly with decreasing pitch angle. The reason for this apparent discrepancy is that the bins of the histogram are spaced linearly in pitch angle which means that as the pitch angle increases, the solid angle (Ω_i) corresponding to each individual pitch angle (α_i) also increases according to $\Omega_i = 2\pi(1 - \cos\alpha_i)$.

The reason this is misleading is shown in Figure 3.5a which shows the solid angle corresponding to linearly spaced bins in pitch angle (dashed blue curve). As illustrated in Figure 3.5b, if each bin in α is one degree, then the solid angle corresponding to the $0°$–$1°$ bin is only $\sim 10^{-3}$ str while the solid angle corresponding to the $70°$–$71°$ bin is 100 times larger ($\sim 10^{-1}$ str). Both the apparent discrepancies described in reference to Figure 3.4a can be addressed by binning the histogram linearly in solid angle (Ω). As shown by the solid green line in Figure 3.5a, the solid angle for each bin is equal resulting in an equal sampling space for all backscattered electrons.
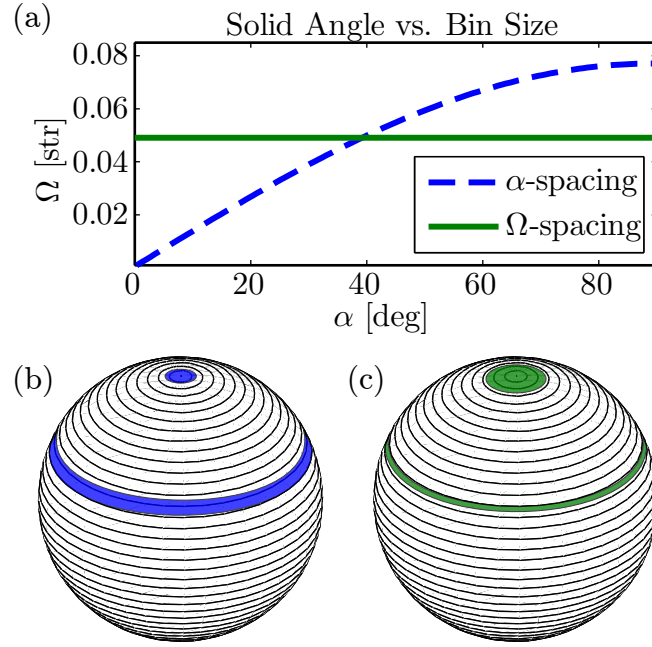
Figure 3.5: (a) Comparison of bin sizes (solid angle) for bins linearly spaced in pitch angle and solid angle. (b) Illustration of bins linearly spaced in pitch angle. (c) Illustration of bins linearly spaced in solid angle.

This is illustrated in Figure 3.5c where it is apparent that the pitch angle range (α) corresponding to each solid angle (Ω) bin is unequal. This is reflected in the size of the bins shown in Figure 3.4b, where the bin sizes decrease with increasing pitch angle (though displaying the bins according to solid angle would yield constant bin-widths). Binning the histogram by solid angle yields results which make more sense. There is a peak in the backscattered distribution at $\sim 50°$ and the probability of backscatter with any specific (low) pitch angle is roughly equal.

1-D Histograms Showing Backscattered Distribution Dependence on Incident Pitch Angle

While Figure 3.4 shows the backscattered pitch angle distribution for one incident pitch angle it is important to show how varying the incident pitch angle can affect

the backscattered pitch angle and energy distributions. Figure 3.6 shows backscattered histograms for a constant incident energy ($\mathcal{E}_0$=0.3 MeV) and incident pitch angles of α_0=30°, 50°, 60°, and 70°. In contrast to Figures 3.2 and 3.3 which showed that the incident energy is the dominant factor in determining the deposition profile of precipitating electrons, Figure 3.6 shows that the incident pitch angle is the dominant factor in determining the pitch angle and energy distributions of backscattered electrons. At grazing incidence, most backscattered electrons have lost a relatively small amount of energy ($\lesssim$10%), while at deep incidence most of the backscattered electrons have lost $\gtrsim$50% of their energy. This occurs because in the absence of atmospheric interactions, the grazing incidence electrons mirror at an altitude significantly higher than electrons incident deep inside the loss cone. This difference in mirror altitude results in shorter total atmospheric interaction times and consequently lower overall energy loss. Note that the sudden drop in in the first bin of each histogram is because the Monte Carlo model removes electrons <2 keV from the backscattered population. The corresponding backscattered pitch angle distributions are shown in Figure 3.6b, and it is clear that similar to the pitch-angle dependent differences in the energy deposition (shown in Figures 3.2b and 3.3), there are also significant differences in the pitch-angle distribution of backscattered electrons based upon the incident pitch angle. There are proportionally fewer electrons backscattered with low pitch angles for incidence at ($\mathcal{E}_0$=0.3 MeV, α_0=70°) than for ($\mathcal{E}_0$=0.3 MeV, α_0=30°), which is due to the number of elastic atmospheric scatterings that are necessary to to alter the local pitch angle to ≥90° and hence backscatter. At grazing incidence it takes relatively few elastic atmospheric scatterings, while at deep incidence it takes relatively many.

1-D Histograms Showing Backscattered Distribution Dependence on Incident Energy

Having shown the variation in backscatter distribution as a function of incident pitch angle, it is now important to determine the backscattered distributions as a function of incident energy. The backscattered energy distribution is not as complicated as the backscattered pitch angle in terms of bin sizes (bins are linearly spaced between 0
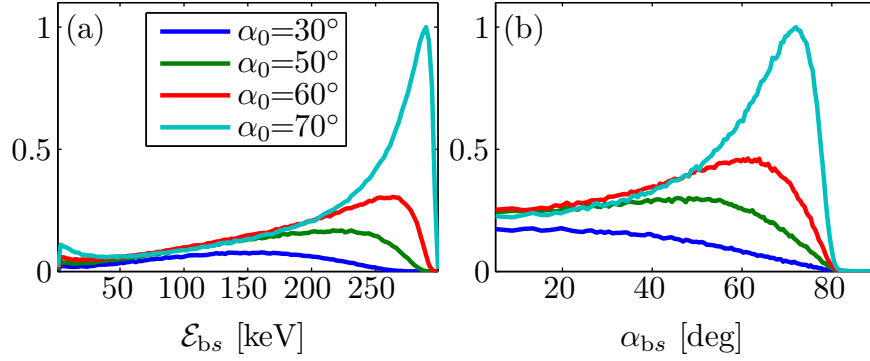
Figure 3.6: 1-D Histograms of backscattered electrons for one energy $\mathcal{E}_0$=0.3 MeV and a range of incident pitch angles, α_0=30°, 50°, 60° and 70°. (a) Backscattered energy. (b) Backscattered pitch angle.

and $\mathcal{E}_0$) with several example histograms shown in Figure 3.7. The initial pitch angle for each distribution is α_0=70°, with separate curves for energies of $\mathcal{E}_0$=0.1 MeV, 0.3 MeV, 0.5 MeV and 1 MeV. Figure 3.7a shows the histograms of backscattered energy normalized by the incident energy (i.e. $x = \mathcal{E}/\mathcal{E}_0$) while Figure 3.7b shows the histograms of backscattered pitch angle at an altitude of 200km ($\alpha_{200\text{km}}$). As seen in this figure, the backscattered distributions are almost completely independent of the initial energy. The backscattered pitch angle shows almost no difference when varying the input energy by an order of magnitude, while the backscattered energy distribution (normalized to the incident energy) shows only very minor differences in the number and (normalized) energy of backscattered electrons. The reason there are slightly fewer and (relatively) less energetic electrons backscattered at 1 MeV is because higher energy electrons penetrate to lower (denser) altitudes where slightly more energy loss and scattering occurs so even though the dynamic friction force is less, the overall energy loss is greater.

2-D Histograms of Backscattered Electrons Showing their Distribution Dependence on $(\mathcal{E}_0, \alpha_0)$

So far this section has described the pitch angle or energy distribution of backscattered electrons, but this is insufficient to fully characterize the atmospheric response to a
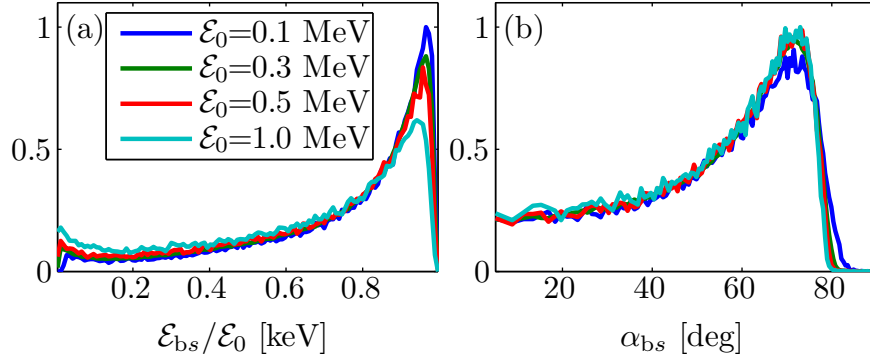
Figure 3.7:   1-D Histograms of backscattered electrons for one pitch angle $\alpha_0=70°$ and a range of incident energies, $\mathcal{E}_0=0.1$ MeV, 0.3 MeV, 0.5 MeV and 1.0 MeV. (a) Backscattered energy. (b) Backscattered pitch angle.

representative monoenergetic, monodirectional beam of incident electrons. While it is logical that there is a relationship between the backscattered energy and pitch angle, the 1-D distributions do not sufficiently characterize the atmospheric response. For example, based upon the cyan curves shown in Figure 3.6, corresponding to ($\mathcal{E}_0=0.3\,$MeV, $\alpha_0=70°$), it is logical to assume that those electrons which have lost the least amount of energy are also those which have diffused the least in pitch angle, and likewise that those electrons which have lost the most energy are those which have diffused furthest in pitch angle. While these assumptions may generally be correct, in order to have confidence in the atmospheric backscatter distributions it is necessary to investigate the exact relationship between energy loss and pitch angle diffusion of backscattered electrons.

To do this it is necessary to create 2-D histograms of the backscattered electrons with each bin in the histogram now corresponding to both an energy and solid angle. Two example 2-D histograms are shown in Figure 3.8 with backscattered energy shown on the abscissa, backscattered pitch angle on the ordinate, and the number of electrons in each bin (linearly spaced in energy and solid angle) shown on the vertical axis and normalized to unity. As expected, the logical trends indicated above are shown to be generally true. The electrons backscattered with the most remaining energy are typically also those with the smallest pitch angle diffusion, however, there
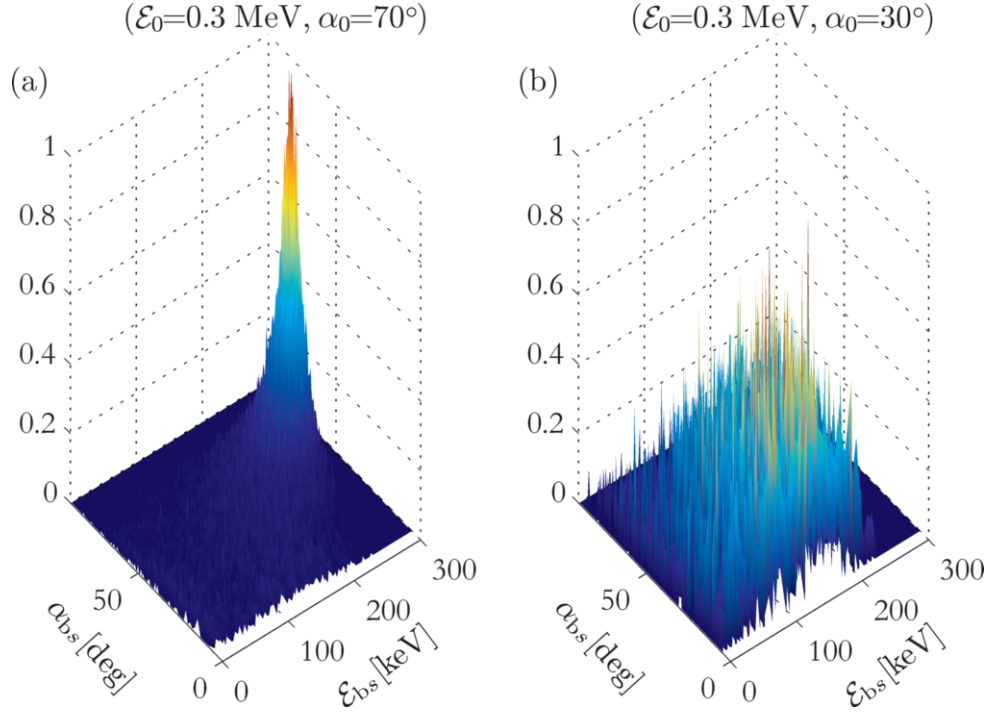
Figure 3.8: 2-D histograms of backscattered electrons with peak normalized to unity. Each bin is corresponds to both an energy and a solid angle. (a) 2-D backscattered distribution for ($\mathcal{E}_0$=0.3 MeV, α_0=70°). (b) 2-D backscattered distribution for ($\mathcal{E}_0$= 0.3 MeV, α_0=30°).

is a complicated relationship between backscattered energy and pitch angle which cannot be accurately described by the individual 1-D histograms.

This approach is clearly superior to the individual 1-D histograms but introduces a new set of challenges for determining the full atmospheric backscatter distribution. Due to the fact that most electrons incident at grazing angles of incidence ($\mathcal{E}_0 =$ 0.3 MeV, α_0=70°) do not lose significant energy or diffuse appreciably in pitch angle there are a large number of electrons with similar backscatter characteristics, and there are a sufficient number of backscattered electrons to smoothly populate the 2-D sampling grid as shown in Figure 3.8a. Conversely, for electrons at deep angles of incidence there is a large spread both in backscattered energy and pitch angle. More importantly, there are significantly fewer backscattered electrons. An example of this is shown in Figure 3.8b which depicts the 2-D histogram of backscattered electrons

incident at ($\mathcal{E}_0$=0.3 MeV, α_0=30°). The smaller number of backscattered electrons leaves the 2-D grid sparsely populated, with the general backscatter characteristics somewhat defined but without the precise distribution of Figure 3.8a. The typical approach for addressing this problem is either to simulate a sufficient number of electrons to populate the grid or to increase the bin size (decrease the sampling) of the 2-D grid. Simulating the number of electrons necessary to sufficiently populate the 2-D grid is not practical due to the huge computational resources required, and decreasing the number of bins runs the risk of undersampling the distribution and missing significant features.

To address both of these problems it is necessary to find a more computationally efficient way to populate the 2-D histograms (especially for deep incidence simulations) without sacrificing the necessary sampling precision or simulation accuracy.

3.3.2   Kernel Density Estimation (KDE)

Previous models of atmospheric backscatter [e.g., *Voss et al.*, 1998; *Stadsness and Maehlum*, 1965] have simulated a limited number of electrons and calculated the response for each separately. When additional backscatter calculations are made, a subset of the backscattered population is typically randomly sampled and re-simulated to determine the subsequent backscatter response. While the re-simulation of once-backscattered electrons ensures that the subsequent backscatter responses correspond exactly to the initial distribution, it limits the extendability of the result such that each new initial distribution must be re-simulated, making it computationally infeasible to produce a general and globally applicable result. Since the goal of this work is to produce a model which is applicable for any arbitrary distribution of electrons, the previous approaches are insufficient and a new solution is necessary.

The 2-D backscatter distributions discussed in Section 3.3.1 are an excellent approach to extending the applicability of the Monte Carlo model results to any arbitrary input distribution. However, these distributions present the problem of either unwieldy computational requirements or undersampled backscatter distributions limits their effectiveness. To maintain a sufficiently sampled distribution while limiting

the computational demand requires a method of extending the computational results over under-populated regions. An excellent approach to accomplish this goal is through the use of a kernel density estimation (KDE) technique.

The KDE can be thought of in terms similar to a typical histogram, except that instead of placing a single element in a bin, the element is spread out or smoothed by some kernel into the center bin and surrounding bins. The most common kernel used is a Gaussian kernel with a zero mean and standard deviation (or bandwidth) of one. Assuming that a Gaussian kernel is sufficient for the atmospheric backscatter data, the challenge is to determine a representative bandwidth for the bivariate kernel (i.e., a two-dimensional Gaussian with separate bandwidths for $\mathcal{E}$ and Ω). The bandwidths are chosen [*Sheather and Jones*, 1991; *Botev*, 2006] based upon the backscattered electron properties calculated by the Monte Carlo model for each ($\mathcal{E}_0$, α_0) and the kernel smoothing is carried out using a two dimensional discrete cosine transform.

KDE Model Verification

Of course, the most important question in the use of the KDE is whether or not the calculated results are accurate. To determine whether or not this is the case it is necessary to evaluate the backscattered distributions to see how they compare to the simulated results. This is accomplished by choosing a small (but representative) number of the $\sim$16,000 input distributions and simulating a very large number of electrons. As the number of backscattered electrons increases, the noise inherent in the under-populated distributions smooths and approaches the desired result. As shown in Section 3.3.1 the distribution of backscattered electrons is relatively consistent with normalized energy but varies significantly with pitch angle. The chosen distributions for the KDE model verification are therefore for $\mathcal{E}_0$=0.3 MeV and for the entire range of incident pitch angles (0°–90°, calculated at every 10° increment).

Figures 3.9 and 3.10 show how the 2-D histogram of backscattered electrons (and corresponding KDE distribution) evolve as a larger number of electrons are included in their calculation. The top row of each figure shows the 2-D histogram of the
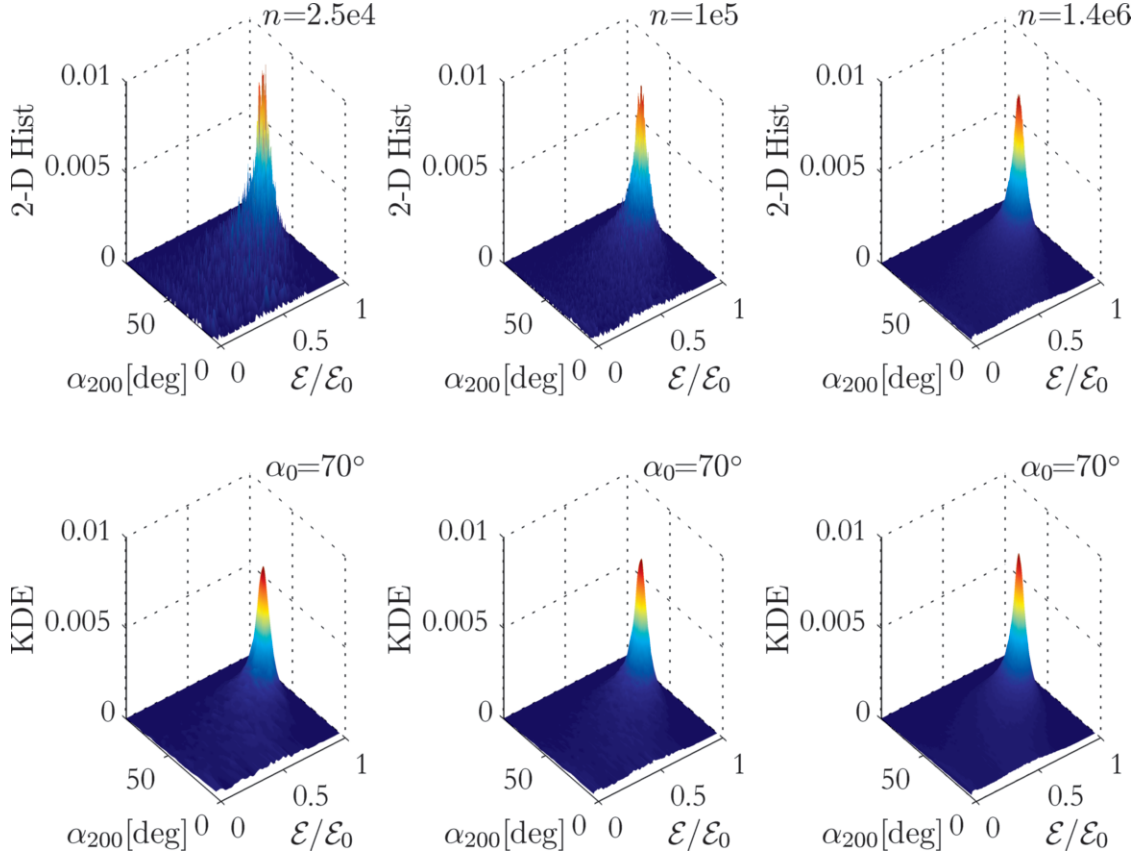
Figure 3.9: KDE method justification for $\Psi^{\mathrm{norm}}(\mathcal{E}_0=0.3\,\mathrm{MeV}, \alpha_0=70°|x,\alpha_{200})$. The top row shows the 2-D histogram as more electrons are included in its calculation. The bottom row shows the corresponding KDE.

backscatter distribution and the bottom row shows the corresponding KDE estimated distribution. Each subplot shows the normalized energy $(\mathcal{E}/\mathcal{E}_0)$ on the abscissa, backscattered pitch angle $(\alpha_{200\mathrm{km}})$ on the ordinate, and count on the vertical axis (normalized by the number of input electrons). Each column shows the number of electrons in the simulated monoenergetic, monodirectional electron beam in the top row of panels and the incident pitch angle in the bottom row of panels.

Figure 3.9 shows the 2-D histograms and KDE estimates for an input at a grazing angle of incidence, $(\mathcal{E}_0=0.3\,\mathrm{MeV}, \alpha_0=70°)$. The first column shows the backscatter distribution for $n = 2.5 \times 10^4$ incident electrons, the second column for $n = 10^5$ electrons, and the third column for $n > 1.4 \times 10^6$ incident electrons. The differences in the

2-D histograms are striking. While the first column shows the overall structure of the backscattered distribution, there is a general undersampling of the lower pitch angle and energy portions of the distribution (as shown by the jagged-looking distribution), the third column shows a smooth and well-sampled 2-D histogram, indicating that sufficient electrons have been simulated to determine an accurate distribution.

While the three 2-D histograms in the top row change markedly with the number of simulated electrons, the corresponding KDE distributions shown in the bottom row change very little even with a sixty-fold increase in the number of simulated electrons. The only minor changes come in the peak counting rate of the KDE distributions, and slight narrowing of the simulated peak. More important is the demonstration that the KDE distribution for 10^5 simulated electrons (bottom row, middle column) matches the 'actual' backscattered distribution (shown in the top-right), calculated from $n > 1.4 \times 10^6$ simulated electrons, very closely.

The accuracy of the KDE results for grazing incidence electrons are very close to the actual distribution, however as shown in Figure 3.8b, electrons which are initially input at a deep angle of incidence are backscattered far less often, meaning that a significantly higher number of simulated electrons are required to sufficiently populate the 2-D backscatter distribution. KDE calculations and 2-D backscatter histograms for deep incidence electrons ($\mathcal{E}_0$=0.3 MeV, α_0=30°) are shown in Figure 3.10, with axes similar to that in Figure 3.9. As expected, the 2-D histograms for deep incidence are significantly sparser than the corresponding histograms for grazing incidence, this is due to the relatively small fraction of deep-incidence electrons which are backscattered from the atmosphere and the wider range of $\mathcal{E}$–Ω bins which are typically filled. The result is that the differences between the columns are more dramatic than the corresponding 2-D histograms from Figure 3.9. In fact for the $n = 2.5 \times 10^4$ simulation (top left panel) it is difficult to see any trend at all due to the sparseness of the plot. The middle column (showing $n = 10^5$ incident electrons) is better, but even the last column (with $n > 1.5 \times 10^6$ incident electrons) is still not entirely smooth, but certainly defines the backscatter response sufficiently. In contrast to the 2-D histograms, the KDE distributions for all three cases are again fairly consistent even with only $n = 2.5 \times 10^4$ incident electrons.
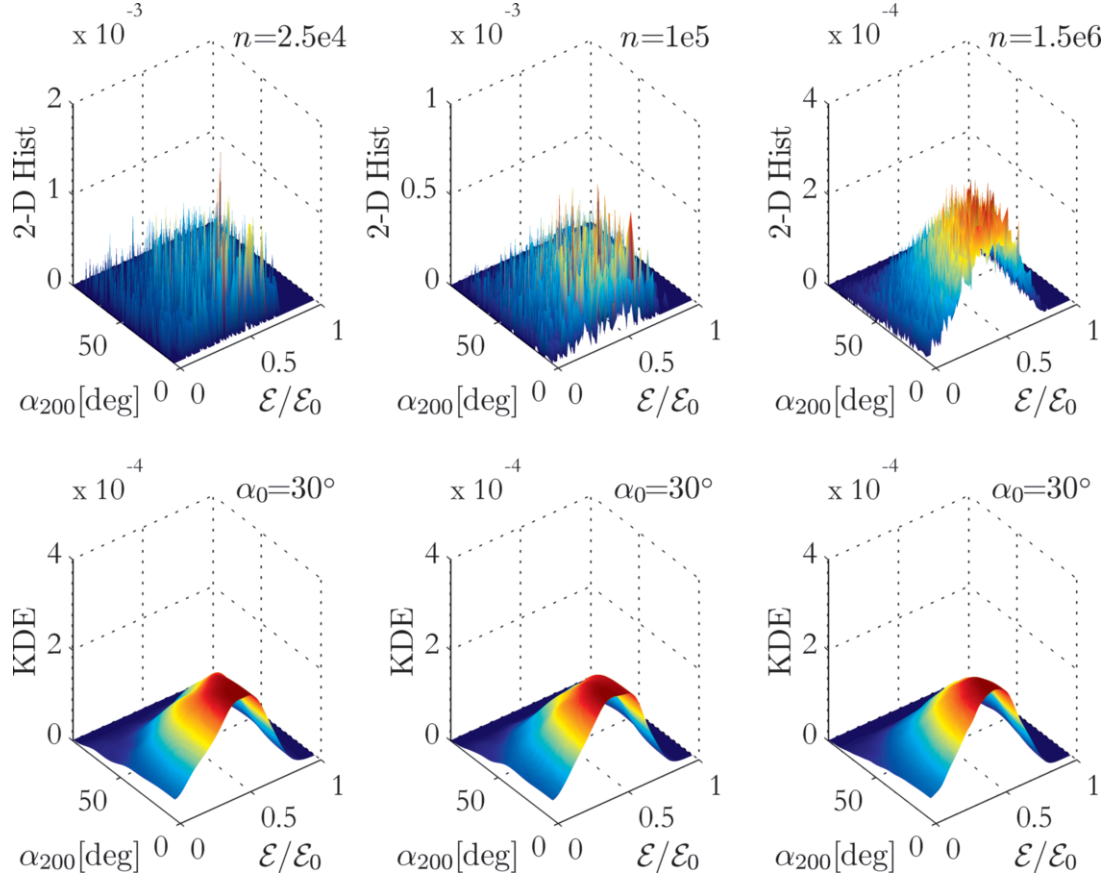
Figure 3.10: KDE method justification for $\Psi^{\mathrm{norm}}(\mathcal{E}_0{=}0.3\,\mathrm{MeV},\ \alpha_0{=}30°|x,\alpha_{200})$. The top row shows the 2-D histogram as more electrons are included in its calculation. The bottom row shows the corresponding KDE.

The demonstration that all the KDE distributions (especially for $\geq 10^5$ incident electrons) closely approximate the calculated 2-D histogram for the $n > 1.5$ million distribution indicates that the desired effect has been achieved and it is now computationally feasible to completely characterize the atmospheric backscatter response to a precipitating electron using the method described in this section. Finally, though not shown here, the results are similar for all investigated pitch angles (0°–90°) indicating that $n = 10^5$ simulated electrons are sufficient to completely characterize the atmospheric backscatter response, $\Psi_0(\mathcal{E}_0,\ \alpha_0|\mathcal{E},\alpha)$, for any modeled input.

3.3.3 Atmospheric backscatter distributions: $\Psi_0(\mathcal{E}_0, \alpha_0 | \mathcal{E}, \alpha)$

As discussed in Section 3.3.2, a major improvement of the current approach over previous calculations of atmospheric backscatter [e.g., *Stadsness and Maehlum*, 1965; *Wedde*, 1971; *Wulff and Gledhill*, 1974; *Berger et al.*, 1974] is in the treatment of the backscattered population of electrons. The ABS model uses a large number of simulated electrons ($\geq 10^5$) and then normalizes the response to that of a single precipitating electron per unit area. Combinations of different $\Psi_0(\mathcal{E}_0, \alpha_0 | \mathcal{E}, \alpha)$ can therefore be used to characterize the atmospheric response to any arbitrary distribution of precipitating electrons. In the case of atmospheric backscatter calculations these results can then be used in subsequent calculations, eliminating the need to re-simulate for a new distribution of precipitating electrons. This approach is viable because the interaction of electrons with the atmosphere (i.e., loss of energy or diffusion in pitch angle resulting from interaction with the atmosphere) is determined by the atmospheric neutral density [*Jackson*, 1998, Ch. 13] which remains relatively unchanged by even the largest conceivable flux of electrons precipitated through wave-particle interactions. This property of linearity between the different $\Psi_0(\mathcal{E}_0, \alpha_0 | \mathcal{E}, \alpha)$ pairs allows the response for any arbitrary input distribution of electrons to be calculated by a combination of the individually calculated atmospheric backscatter responses.

To illustrate how varying $\mathcal{E}_0$ and α_0 affect the backscatter distributions, Figure 3.11 shows $\Psi^{\mathrm{norm}}(\mathcal{E}_0, \alpha_0 | x, \alpha)$ for several different $(\mathcal{E}_0, \alpha_0)$ input pairs. Each row corresponds to a different input energy ($\mathcal{E}_0$, indicated at the left of each row) and each column to a different input pitch angle, α_0 (at 200 km, indicated at the top of each column). In each individual panel the abscissa corresponds to the energy of backscattered electrons normalized to the input energy ($x = \mathcal{E}/\mathcal{E}_0$) while the ordinate shows the pitch angle of the backscattered electrons at an altitude of 200 km (up-going). The color bar shows the fluence of backscattered electrons (normalized to a single precipitating electron per unit area) with all panels displaying the same color axis for easy comparison. Finally, the fraction of total incident energy which is backscattered is shown in the top-left corner of each panel.

As described above, backscatter occurs when the result of any individual atmospheric interaction leaves an electron with a local pitch angle of $\geq 90°$. The first
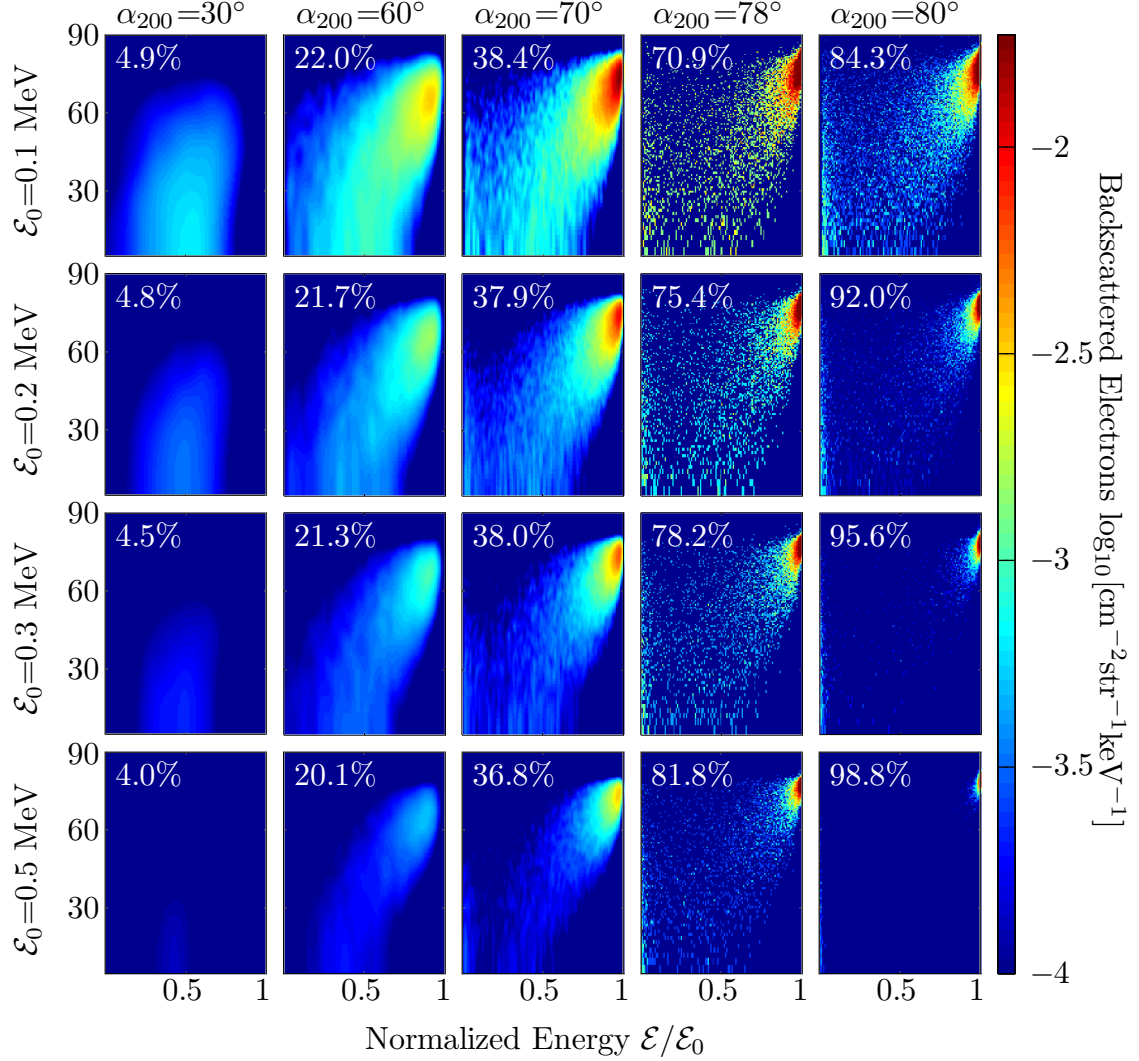
Figure 3.11: Electron backscatter distributions as a function of both $(\mathcal{E}_0, \alpha_0)$. Each panel has the same axes. The abscissae show normalized energy $(x = \mathcal{E}/\mathcal{E}_0)$ of the backscattered electrons, ranging from 0–1 and the ordinates show the pitch angle of backscattered electrons (up-going, at an altitude of 200 km) ranging from 0°–90°. The color bar indicates the backscattered fluence (normalized to a single precipitating electron per unit area) in units of $cm^{-2}str^{-1}keV^{-1}$. Each row shows a specific incident energy $(\mathcal{E}_0)$, indicated at the left of each row, and each column shows a specific incident pitch angle (α_{200km}), indicated at the top of each column. Note that the color bar corresponds to the $\log_{10}$ of the fluence.

column of Figure 3.11 shows that only a very small fraction of electrons incident with pitch angles deep inside the loss cone are backscattered. Those electrons which are backscattered have lost much of their initial energy and leave the atmosphere with a pitch angle distribution which is isotropic and completely uncorrelated to the incident pitch angle. This result is due to the fact that each atmospheric elastic scattering interaction results in only a small pitch angle deflection [*Lehtinen et al.*, 1999] so that it takes many interactions before the electron can have a high enough pitch angle to mirror and return to the magnetosphere. Furthermore, numerous elastic scatterings also imply numerous inelastic scatterings. Although the inelastic scatterings are less frequent and the fractional energy loss in each inelastic scattering is small, they may (but not always, see example below) accumulate and thus lead to a significant total energy loss.

Comparing any column in Figure 3.11 it appears that for the same initial pitch angle the backscattered fluence is significantly less for higher energy than lower energy electrons. This apparent difference is because each panel is normalized to a single precipitating electron with the specified energy and pitch angle (per unit area), not to a single unit of fluence (i.e., $\mathrm{cm}^{-2}\mathrm{str}^{-1}\mathrm{keV}^{-1}$). However, it is clear from the percentages shown in each panel that the fraction of total input energy backscattered is roughly constant with $\mathcal{E}$ below the loss cone (columns 1–3), and increases with $\mathcal{E}$ for electrons incident with pitch angles at or above the loss cone (columns 4–5).

Next, it is important to note that as the incident pitch angle increases, the number of atmospheric scatterings required to change the local pitch angle to $\geq 90°$ decreases (on average) and therefore the backscattered distribution begins clustering nearer to the initial input distribution. This effect is seen most clearly in the third row of Figure 3.11, corresponding to $\mathcal{E}_0 = 0.3$ MeV where the backscatter distributions for higher incident electron pitch angles show less diffusion in pitch angle and significantly less energy loss. For example, for $(\mathcal{E}_0 = 0.3\,\mathrm{MeV},\ \alpha_0 = 78°)$ —right at the conventionally-defined loss cone angle (i.e., $\alpha_{100\mathrm{km}} = 90°$)— $\sim 78\%$ of the total incident energy is backscattered. In addition, many of the electrons which are backscattered have retained much of their initial energy ($\gtrsim 290$ keV) but have experienced a relatively large

diffusion in pitch angle to between 72°–82° because inelastic scatterings are less frequent that elastic. Above the loss cone angle, at $(\mathcal{E}_0 = 0.3\,\text{MeV}, \alpha_0 = 80°)$, almost 96% of the total initial energy is backscattered with the majority of backscattered electrons having experienced a pitch angle diffusion to between 74°–84°. Note that due to the definition of the loss cone angle, the first scattering for such electrons has to occur above 100 km.

Both of these observations are important with respect to the characteristics of observed LEP events. First, as only ∼22% of the energy incident at $(\mathcal{E}_0 = 0.3\,\text{MeV}, \alpha_0 = 78°)$ is initially deposited into the atmosphere, the initial precipitation may not be detectable using subionospheric VLF remote sensing. In addition, since after the first backscatter the pitch angle distribution has broadened (72°–82°), more energy is deposited into the conjugate hemisphere.

Assuming a dipole magnetic field, the pitch angle distribution of electrons leaving one hemisphere is the same entering the conjugate hemisphere at the same altitude (the fact that such is not physically the case for the true magnetic field has a significant effect on the backscatter distribution as discussed in Section 3.6). In the case of a dipole field, all of the backscattered electrons —containing 78% of the initial energy— reach the conjugate hemisphere, of which more than 36% of remaining energy is deposited (30% of the initial energy, which is 30% more than in the first deposition of 22%) and only ∼50% of the total initial energy remaining in the magnetosphere to return to the initial hemisphere. This result suggests that the ionospheric disturbance in the conjugate hemisphere is larger than in the initial hemisphere. For the case of $(\mathcal{E}_0 = 0.3\,\text{MeV}, \alpha_0 = 80°)$ the results are even more pronounced. The broadening of pitch angles (input into the conjugate hemisphere) to 74°–84° leads to 13% of the energy which reaches the conjugate hemisphere being deposited (12% of the initial energy, or 200% more than the initial deposition of 6%), leaving roughly 83% of the initial energy un-deposited.

The dependence of the backscatter distribution on both $(\mathcal{E}_0, \alpha_0)$ is of critical importance for the evolution of an LEP event because a typical wave-particle interaction results in an equatorial pitch angle change of only a fraction of a degree [*Chang and Inan*, 1983; *Inan et al.*, 1989; *Bortnik et al.*, 2006a,b]. This result indicates that a

typical precipitating electron distribution is nearly always incident onto the atmosphere at a grazing angle of incidence and $\gtrsim 70\%$ of the energy is backscattered and subsequently incident on the conjugate hemisphere in its next atmospheric interaction.

3.4   Properties of $N_{e0}(\mathcal{E}_0,\,\alpha_0|h)$ and $\Psi_0(\mathcal{E}_0,\,\alpha_0|\mathcal{E},\alpha)$

Having now completely characterized both $N_{e0}(\mathcal{E}_0,\,\alpha_0|h)$ and $\Psi_0(\mathcal{E}_0,\,\alpha_0|\mathcal{E},\alpha)$ with respect to incident energy and pitch angle, it is now possible to discuss additional factors which can affect the full atmospheric backscatter calculation, and which must be addressed in order to apply these results to realistic distributions of electrons with confidence.

3.4.1   Effects of the Magnetic Dip Angle

As discussed in Section 2.2.2, the strength of the magnetic field varies with both longitude and hemisphere. Not only does this asymmetric magnetic field cause longitudinal and hemispheric differences in the loss cone angle, but it also affects the magnetic dip angle (Φ), which is the angle of the magnetic field line measured from the horizontal plane. While the atmospheric neutral density is the dominant factor in determining electron backscatter characteristics, it is possible that for vastly different magnetic dip angles the trajectory of precipitating electrons could be systematically varied enough to affect $N_{e0}(\mathcal{E}_0,\,\alpha_0|h)$ and/or $\Psi_0(\mathcal{E}_0,\,\alpha_0|\mathcal{E},\alpha)$. In order to investigate this possibility it is necessary to simulate a full range of precipitating electrons incident upon the atmosphere under the influence of a magnetic field with a variable dip angle. If the variation of $N_{e0}(\mathcal{E}_0,\,\alpha_0|h)$ and $\Psi_0(\mathcal{E}_0,\,\alpha_0|\mathcal{E},\alpha)$ with magnetic dip angle is substantial then a separate simulation set, $N_{e\mathbf{M}}(\mathcal{E}_0,\,\alpha_0|h)$ and $\Psi_{\mathbf{M}}(\mathcal{E}_0,\,\alpha_0|\mathcal{E},\alpha)$, is necessary for each dip angle.

The dip angle as a function of longitude is shown in Figure 3.12 for L=2 and L=3. Similar to Figure 2.3a, the dip angle in the Northern Hemisphere is shown in blue while the dip angle in the Southern Hemisphere is shown in green. Between the two curves
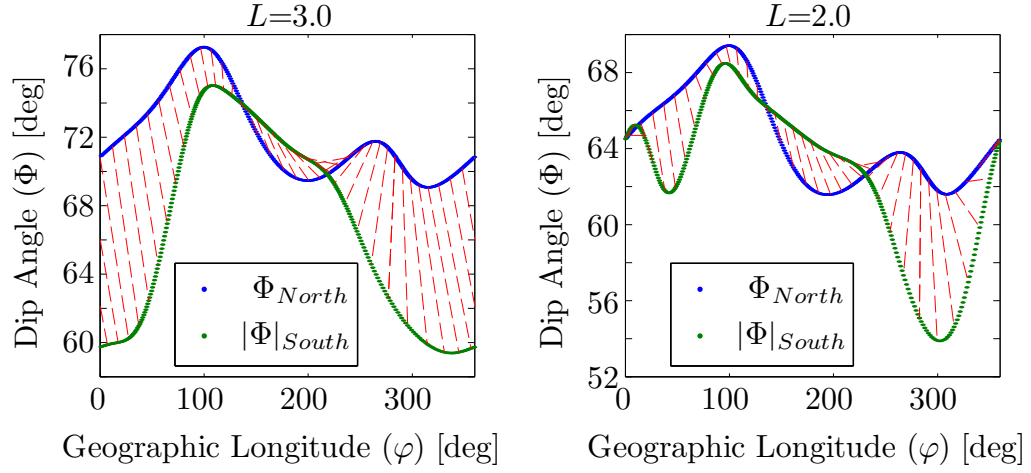
Figure 3.12: Magnetic dip angle at $L = 2$ and $L = 3$ and all longitudes. Note that the ideal geomagnetic dipole model values are $\Phi = \tan^{-1} 2\sqrt{L-1} = 70.5°$ for $L = 3$ and $64.3°$ for $L = 2$.

are thin red lines every $10°$ in longitude, linking conjugate points for reference. The maximum dip angle for the L=2–3 region is at (L=3, $\varphi \sim 100°$ **E/N**), where the magnetic dip angle is $\Phi \simeq 77°$ and the minimum dip angle is at (L=2, $\varphi \sim 300°$ **E/S**), where the dip angle is $\Phi \simeq 54°$. Comparing the variation in $N_{e0}(\mathcal{E}_0, \alpha_0|h)$ and $\Psi_0(\mathcal{E}_0, \alpha_0|\mathcal{E}, \alpha)$ at these two extreme mid-latitude dip angles as well as at $\Phi \simeq 68°$ (representing a typical intermediate point) is necessary to determine the global applicability of the ABS model.

Figure 3.13 shows $N_{e0}(\mathcal{E}_0, \alpha_0|h)$ for three separate incident pitch angles (α_0=30°, α_0=70°, and α_0=78°) and three separate energies ($\mathcal{E}_0$=0.1 MeV, $\mathcal{E}_0$=0.3 MeV, and $\mathcal{E}_0$=1.0 MeV) representing the broad spectrum of precipitation characteristics likely to be observed in an LEP observation. The incident pitch angle is indicated at the top of each column and the incident energy is indicated on the right side of each row. The solid lines in each panel are the deposition for the each dip angle (labeled by the L-shell at which the dip angle occurs). Note that even on a logarithmic scale it is impossible to see any qualitative difference between the deposition profiles. Indeed, the peak of $N_{e0}(\mathcal{E}_0, \alpha_0|h)$ at each of the three dip angles is within $\leq 1\%$ for all investigated ($\mathcal{E}_0$, α_0). The only way to see the difference quantitatively is to calculate
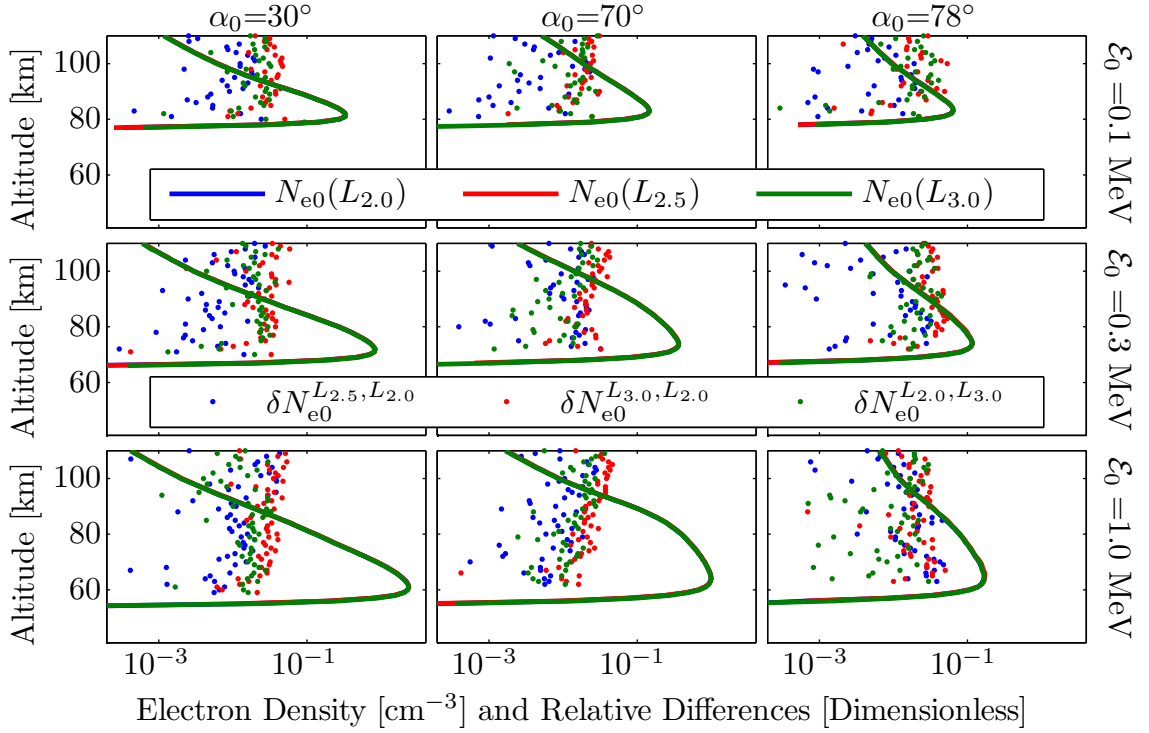
Figure 3.13: $N_{e0}(\mathcal{E}_0, \alpha_0|h)$ profiles at varying dip angles (lines) and the relative difference between profiles (dots).

the relative difference between the various profiles. This difference is shown by the colored dots within each panel. $\delta N_{e0}^{L_1, L_2}$ represents the relative difference between $N_{e0}(\mathcal{E}_0, \alpha_0|h)$ at $L = L_1$ and $L = L_2$:

$$\delta N_{e0}^{L_1, L_2}(\mathcal{E}_0, \alpha_0|h) = \frac{N_{e0}(\mathcal{E}_0, \alpha_0, L_1|h) - N_{e0}(\mathcal{E}_0, \alpha_0, L_2|h)}{N_{e0}(\mathcal{E}_0, \alpha_0, L_1|h)}.$$

While the difference between the peak of each deposition is only 1%, the difference at other altitudes can reach as high as 5%, but is still quite small. At first sight, this result is in apparent contrast to past work [*Wulff and Gledhill*, 1974] in which a magnetic dip angle dependence on deposition was calculated for electrons precipitating in relation to the aurora. However, this contrast is easily understood in terms of the limited range of magnetic dip angles which are necessary here, and also because the electrons of interest here are of much higher energy (≥ 50 keV vs. ~ 1 keV).
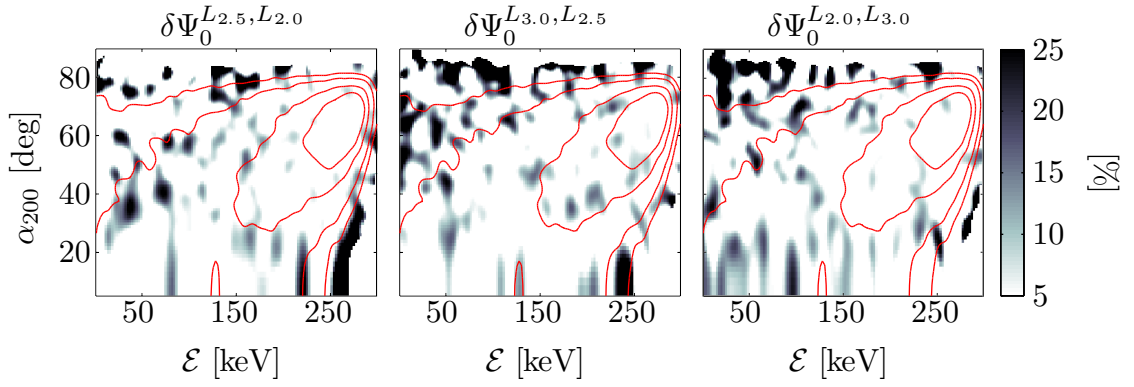
Figure 3.14: Relative difference in $\Psi_0(\mathcal{E}_0, \alpha_0|\mathcal{E}, \alpha)$ distributions (in percent) for varying dip angle.

The $\Psi_0(\mathcal{E}_0, \alpha_0|\mathcal{E}, \alpha)$ distributions corresponding to the deposition profiles in Figure 3.13 (not shown) are all qualitatively similar and in fact the fraction of total energy backscattered for each of the three investigated dip angles is within 0.3%. This indicates that $\Psi_0(\mathcal{E}_0, \alpha_0|\mathcal{E}, \alpha)$ is not qualitatively affected by the dip angle. However, close inspection reveals that there are some differences between the specific distributions as shown in Figure 3.14. Each panel shows the relative difference between $\Psi_0(\mathcal{E}_0, \alpha_0|\mathcal{E}, \alpha)$ at each of the three dip angles as a function of both energy and pitch angle and for an input of ($\mathcal{E}_0$=0.3 MeV, α_0=60°). Overlaid in red on each panel are contours of constant fluence (on a log scale) with the lines (from inside out) representing contours of -3.25, -3.5, -4, and -4.5. This is done to indicate which portions of the backscatter are most important (i.e., where the highest fluence is located). Note that while each title lists only the L-shells (e.g., $\delta\Psi_0^{L_1,L_2}$), the meaning is:

$$\delta\Psi_0^{L_1,L_2}(\mathcal{E}_0, \alpha_0|\mathcal{E}, \alpha) = \frac{\Psi_0(\mathcal{E}_0, \alpha_0, L_1|\mathcal{E}, \alpha) - \Psi_0(\mathcal{E}_0, \alpha_0, L_2|\mathcal{E}, \alpha)}{\Psi_0(\mathcal{E}_0, \alpha_0, L_1|\mathcal{E}, \alpha)}.$$

Note that for all three cases the difference is $\leq$5% for the vast majority of the distribution. This is especially true for the portion of the backscatter distribution which is near to the peak of $\Psi_0(\mathcal{E}_0, \alpha_0|\mathcal{E}, \alpha)$. Most of the differences larger than 5% occur in portions of $\Psi_0(\mathcal{E}_0, \alpha_0|\mathcal{E}, \alpha)$ for which the fluence is at least an order of magnitude below the peak. In these cases calculating the percent difference is

essentially dividing by zero and negligible absolute differences result in large relative differences which are not significant to $\Psi_0(\mathcal{E}_0, \alpha_0|\mathcal{E}, \alpha)$.

While the differences between $N_{e0}(\mathcal{E}_0, \alpha_0|h)$ and $\Psi_0(\mathcal{E}_0, \alpha_0|\mathcal{E}, \alpha)$ calculated with varying magnetic dip angle are fairly small even for dip angle changes varying by more than $\sim 20°$ there are sufficient differences that it is useful to select a representative dip angle each L-shell. Based upon calculations similar to that presented in Figure 3.12, the representative dip angles are $63°$, $68°$ and $72°$. These angles are roughly the mean value of the dip angle over L=2.0, L=2.5, and L=3.0, respectively, and correspond to a geographic longitude of $270°$ **E/N**.

3.4.2 Timing Effects

All discussion of precipitating or backscattered electron densities in this chapter are in terms of a fluence (measured in el-cm^{-2}str^{-1}keV^{-1}) rather than the typical method of discussing magnetospheric particle densities which is flux (measured in el-cm^{-2}s^{-1}str^{-1}keV^{-1}). The reason for using fluence is that the scattering due to LEP is inherently an impulsive process and it is not very informative to calculate a number density of electrons per second. It is more useful to work in terms of the time-integrated flux (or fluence) of precipitating and/or backscattered electrons.

While understanding that fluence is a better metric than the flux for this particular situation, it is still necessary to be able to determine (or at least estimate) the timing of the precipitation/backscatter evolution with subsequent interactions in the respective hemispheres. If the initial distribution of electrons disperse significantly as they interact with the atmosphere and/or as they traverse between hemispheres then it is not be possible to estimate the timing effects of the LEP process using the fluence. If, however, the electrons stay relatively bunched together during the atmospheric backscatter and magnetospheric traverse then by simply assuming some initial time duration profile for the incident distribution of electrons (e.g., 0.5 s [*Lauben et al.*, 2001, Fig. 4]) it is possible to retain the benefits of the fluence calculation while still estimating the timing characteristics of modeled LEP events.

To answer this question it is necessary to determine two separate timing effects.

The first is the flight-time (or bounce period) of magnetospheric particles as they traverse the magnetic field between conjugate points, and the second is the time it takes for the precipitating electrons to backscatter from the atmosphere. In addition, the two are not directly related and it is necessary to determine whether or not the atmospheric backscatter time is an appreciable fraction of the bounce period between hemispheres.

Magnetospheric Electron Bounce Period (τ_b)

The primary complication for the bounce period (τ_b) calculation is that the bounce period of trapped (or half-trapped) magnetospheric electrons is a strong function of both energy and pitch angle. Therefore the packet of incident electrons continues to spread in time as it mirrors between hemispheres. To assess the range of bounce periods which are present in a distribution of backscattering 0.1 MeV–0.3 MeV electrons it is useful to compare the variability of τ_b with the energy and pitch angle. This comparison is shown in Figure 3.15 where contours of constant bounce period (between 200 km altitudes in each hemisphere and calculated using a dipole magnetic field model, but accounting for relativistic factors [*Walt*, 2005, p. 44]) are overlaid on $\Psi_0(\mathcal{E}_0, \alpha_0 | \mathcal{E}, \alpha)$ for electrons incident at ($\mathcal{E}_0$=0.1 MeV, α_0=78°) and ($\mathcal{E}_0$=0.3 MeV, α_0=78°) and at L=2.5.

Notice that in both panels the vast majority of the backscattered electrons lie along one of the contours of constant bounce period. This fact indicates that for electrons incident upon the atmosphere near the loss cone, the effect of energy loss on τ_b (increasing τ_b) is compensated by the decrease in pitch angle (decreasing τ_b) and electrons of the same initial energy incident upon the atmosphere continue to stay bunched together (in agreement with previous work [*Voss et al.*, 1998]). For the specific distributions shown, 0.1 MeV electrons are bunched near a bounce period of 0.45 s, and 0.3 MeV electrons are bunched near 0.3 s which is an important fact to note when discussing the predicted characteristics of LEP events as discussed in Chapter 4.
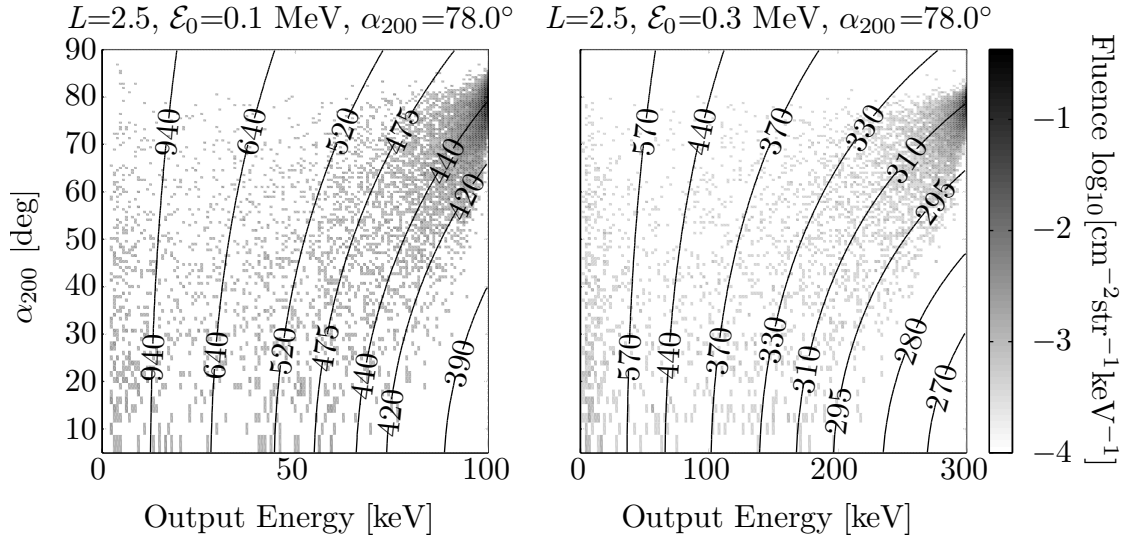
Figure 3.15: Contours of constant bounce period (τ_b, in ms) overlaid on example distributions of once-backscattered electrons as a function of energy and pitch angle. Left panel: backscatter distribution for $\Psi_0(\mathcal{E}_0{=}0.1\,\text{MeV}, \alpha_0{=}78°|\mathcal{E}, \alpha_{200})$ where α_{200} is the output pitch angle evaluated at 200 km. Right panel: backscatter distribution for $\Psi_0(\mathcal{E}_0{=}0.3\,\text{MeV}, \alpha_0{=}78°|\mathcal{E}, \alpha_{200})$.

Atmospheric Backscatter Time

Knowing that electrons of the same energy which are initially bunched together remain together after an atmospheric backscatter, the next step is to determine whether or not the atmospheric backscatter time itself is an appreciable fraction of the bounce period. The bounce period depends on both the energy and pitch angle of precipitating electrons and it is important to determine the extent that these same factors affect the atmospheric interaction time.

The Monte Carlo model tracks the interaction time (along with all physical properties) throughout the simulation and returns the time each particle exits the atmosphere (an altitude of 200 km in this case). Figure 3.16 shows histograms of backscatter time for various $(\mathcal{E}_0, \alpha_0)$ and it is evident that like the bounce period, the atmospheric interaction time is a strong function of both energy and pitch angle. While energy is the dominant factor affecting the bounce period, the incident pitch angle dominates the atmospheric interaction time. At deep angles of incidence

($\alpha_0 \lesssim 70°$) the backscatter time is limited to below $\sim$10 ms regardless of energy while at grazing angles ($\alpha_0 \gtrsim 70°$) there is a spread in the backscatter time reflecting the fact that some electrons backscatter quickly while others penetrate to lower altitudes and backscatter more slowly. In addition, at grazing incidence the energy-dependence of the backscatter time is more pronounced, with the lower energy electrons showing significantly more temporal spread than higher energy electrons. Finally, though not shown, backscatter timing results for $\mathcal{E}_0 > 1$ MeV follow the same general trends as the 1 MeV described above with all backscatter interactions taking place over times $\lesssim$10 ms.

Significant for this work is the demonstration that the backscatter time is always a very small fraction of the total bounce period. For example, the longest backscatter time of $\sim$20 ms which occurs for electrons of $\lesssim$0.1 MeV constitutes less than 5% of the bounce period of $\sim$450 ms and as such is a negligible contribution to the total magnetospheric flight-time between hemispheres. Similarly, for the higher energy electrons the longest backcatter time of $\sim$10 ms is only 3% of the 300 ms flight time for 0.3 MeV electrons. Note that even at L=2 (where the bounce period is shorter) the backscatter time still constitutes only $\lesssim$5% of the total flight-time.

Combining the results for bounce period and backscatter time shows that the backscattered particles stay relatively bunched together during the backscatter process and it is therefore possible to estimate the timing characteristics of modeled LEP events using the total precipitated fluence as opposed to using a time-dependent flux.

3.4.3 Interpolation Between $\Psi_0(\mathcal{E}_0, \alpha_0 | \mathcal{E}, \alpha)$ Pairs

The ABS model completely spans the electrons of interest for LEP and beyond (i.e. $\mathcal{E}_0 \in [.05, 30]$ MeV and $\alpha_0 \in [0°, 90°]$). Therefore the backscatter response for any incident electron ($\mathcal{E}_0, \alpha_0$) which is not specifically calculated can be found through interpolation. The method of interpolation, however, must be determined. This is the final step necessary before it is possible to fully characterize the backscatter and deposition response for any arbitrary distribution of precipitating electrons.

Interpolating between $\Psi_0(\mathcal{E}_0, \alpha_0 | \mathcal{E}, \alpha)$ which have different axes can be difficult
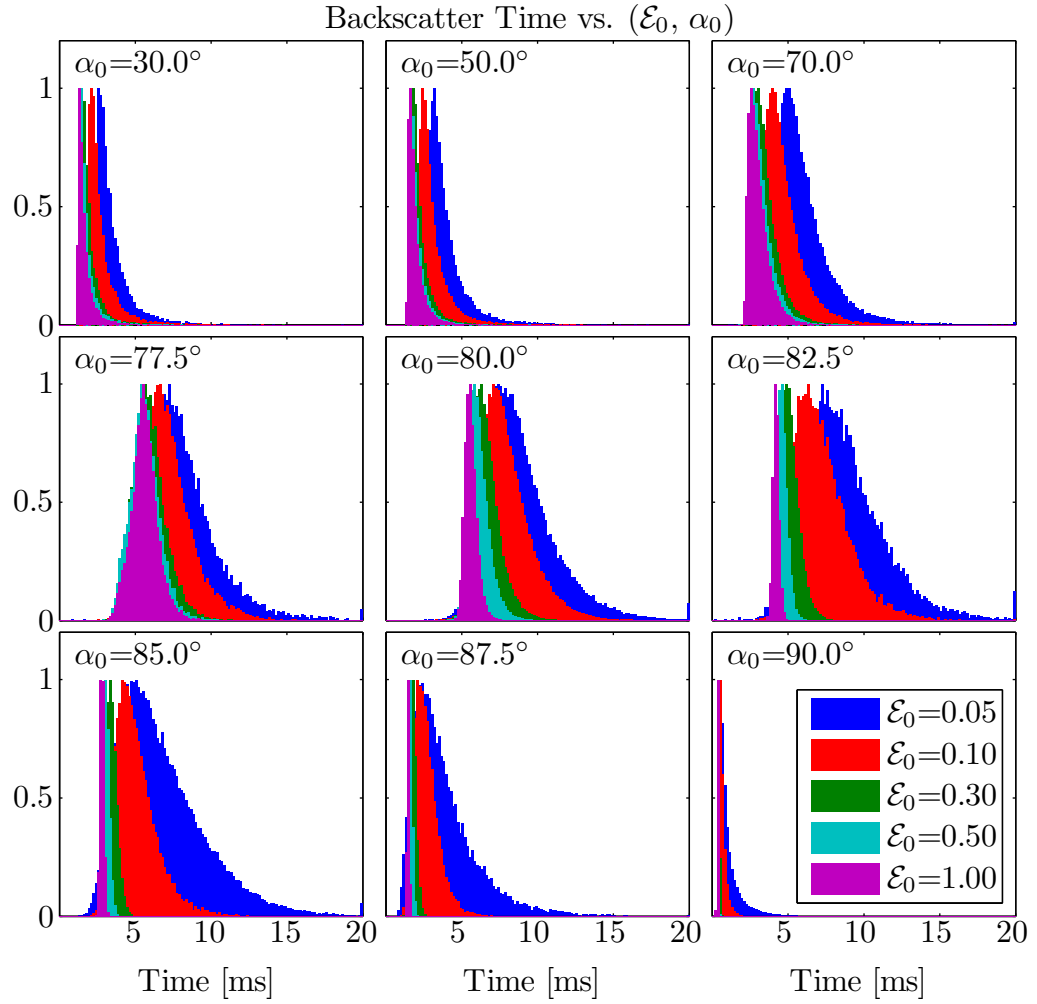
Figure 3.16: Histograms showing the time it takes for electrons to backscatter from the atmosphere as a function of both input energy and pitch angle.

because two distributions which are similar but shifted along one axis or another can lead to erroneous interpolation results. Such is the case for the backscatter distributions of the ABS model. As shown by comparing the 1-D backscatter histograms of Figure 3.7 or the 2-D backscatter responses for any column of Figure 3.11, the similarities in the backscatter distribution on a normalized energy scale ($\mathcal{E}/\mathcal{E}_0$) between electrons of even distant energies is quite close. Even though the blue and green curves of Figure 3.7 differ in incident energy by a factor of three, the backscatter responses normalized with energy are nearly indistinguishable. Similarly, the more accurate 2-D distributions corresponding to the same energy range (third column of Figure 3.11) show that the percentage of backscattered energy is nearly identical, and differ only by scaling factors based upon the size of the energy bin (i.e. keV^{-1}).

The similarities between backscatter distributions of distantly spaced energies indicate that the match between two closely spaced energies would be even more similar. The energy range of primary interest for LEP events is 0.1 MeV–0.3 MeV [e.g., *Peter and Inan*, 2007] and the ABS model samples this energy range with nearly 20 separate energies (for all incident pitch angles indicated in Section 3.1).

To quantify the benefits of interpolating on a normalized energy scale compared to an absolute scale it is necessary to show both methods and compare the error between them. Figure 3.17 shows the backscatter distribution for a known input ($\mathcal{E}_0$=0.28 MeV, α_0=60°) and the interpolated result (using adjacent distributions) for interpolation on an absolute energy scale, and on a normalized energy scale. The panel on the left shows $\Psi_0(\mathcal{E}_0, \alpha_0|\mathcal{E}, \alpha)$ as calculated from the Monte Carlo model, the middle panel shows the result of interpolating to that energy using an absolute energy scale, $\Psi(\mathcal{E}_0', \alpha_0'|\mathcal{E}, \alpha)$, while the last panel shows the result of interpolating using a normalized energy scale $\Psi^{\mathrm{norm}}(\mathcal{E}_0', \alpha_0'|x, \alpha)$. The methods for interpolating these two distributions are shown in Appendix A.

A visual inspection of the interpolation results (Figure 3.17) is sufficient to determine that $\Psi^{\mathrm{norm}}(\mathcal{E}_0', \alpha_0'|x, \alpha)$ is superior to $\Psi(\mathcal{E}_0', \alpha_0'|\mathcal{E}, \alpha)$. While the lower energies and pitch angles tend to match well with the actual backscatter distribution, the peak of the distribution is shifted down in energy to ∼240 keV (compared to ∼250 keV in the actual distribution). Furthermore, the portion of the distribution ≳260 keV and
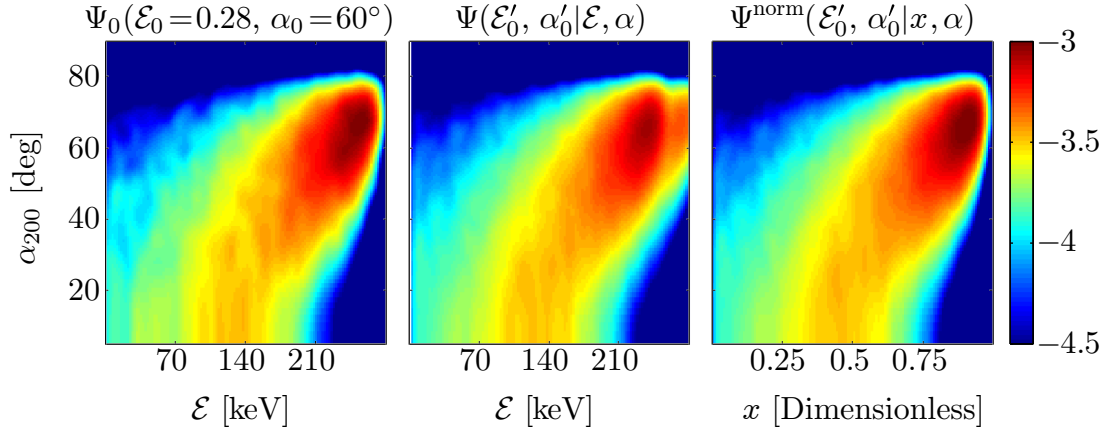
Figure 3.17: Interpolation of a known distribution ($\mathcal{E}_0 = 0.3\,\text{MeV}$, $\alpha_0 = 60°$) (left panel) using an absolute energy scale (middle panel) and a normalized energy scale (right panel).

between 55° and 75° is stretched toward higher energies. This is the effect of interpolating on the absolute energy scale. The linear interpolation between the lower and upper energy bounds smears the energy at the peak to higher energies which are not present in the actual distribution.

Conversely, $\Psi^{\text{norm}}(\mathcal{E}_0', \alpha_0'|x, \alpha)$, shows none of the major deformities associated with $\Psi(\mathcal{E}_0', \alpha_0'|\mathcal{E}, \alpha)$. The peak in the backscattered distribution is located in the correct place and the smearing of the peak to higher energies is also absent. The distribution is smoother than the corresponding Monte Carlo-calculated distribution, $\Psi_0(\mathcal{E}_0, \alpha_0|\mathcal{E}, \alpha)$, but this is to be expected from an interpolation operation and the overall match between the interpolated and calculated distribution is quite good.

The relative error associated with the two methods gives a clearer picture as to the location and severity of the errors introduced by the interpolation. Figure 3.18 shows the relative error for the two interpolation methods on the same axes as those of the initial distribution except that the color bar shows relative error (in percent) instead of fluence. Overlaid in red are contours of constant backscattered fluence from $\Psi_0(\mathcal{E}_0, \alpha_0|\mathcal{E}, \alpha)$ to indicate those portions of the distribution which have a large fluence and those portions which have a very small fluence. Similar to that shown in Figure 3.14, the contours correspond to the limits of the color bar in Figure 3.17
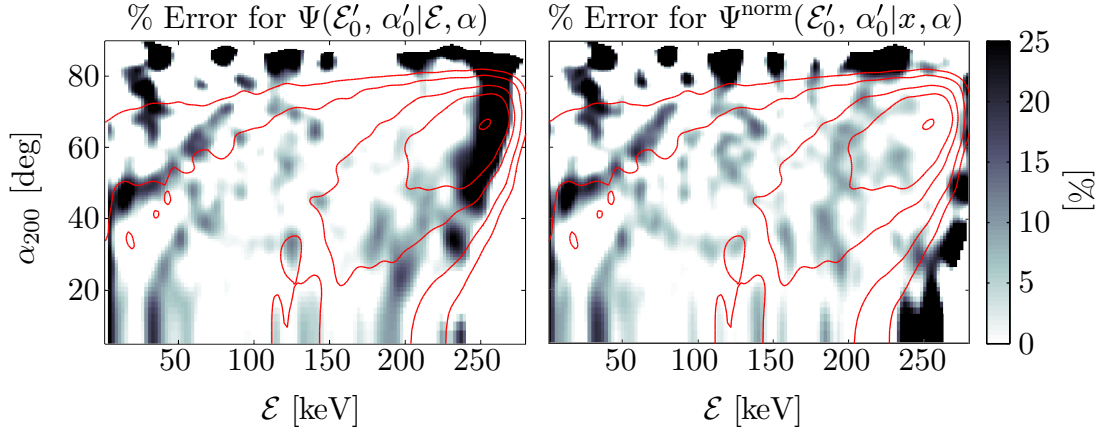
Figure 3.18: Relative error (in percent) introduced by interpolating in energy using an absolute energy scale (left panel) and using a normalized energy scale (right panel).

and are located at -3, -3.25, -3.5, -4, and -4.5. This figure gives a much clearer picture of the location and severity of the errors. The overlaid contours give a good metric to distinguish which portions of the error are most important. Errors near the center contours (inner three contours) are especially egregious because they are near the peak of the backscattered distribution. Errors near the two outer curves on the other hand are not as significant because $\Psi_0(\mathcal{E}_0, \alpha_0 | \mathcal{E}, \alpha)$ is so small in those areas (less by at least an order of magnitude than the peak) that calculating the relative error is essentially dividing by zero and negligible absolute differences result in large relative errors which are not significant to the interpolated distribution.

Figure 3.18 clearly shows why interpolating on the normalized energy scale is far superior. All errors based upon the normalized energy scale are either $\leq 10\%$ or in portions of the distribution which are an order of magnitude smaller than the peak (i.e., outside the 4th or 5th contour). The errors based upon the absolute energy scale (though similar over much of the distribution), are largest near the peak of the backscattered distribution, precisely where the maximum detriment occurs.

The results for other energies (not shown) follow the same trend as described above, though for deep incidence electrons the generated errors are comparable for both interpolation methods, so the normalized energy scale is used for all interpolation calculations during the backscatter process. Finally, it is important to note that

the interpolation demonstration used here is carried out at a known energy so that the distance (in energy) between the interpolated distribution and the surrounding distributions is twice as large as any interpolation which is carried out in practice and this result can therefore be considered to be an upper bound of the error calculation.

3.5 Complete Backscatter Calculation

Calculating $\Psi_0(\mathcal{E}_0, \alpha_0 | \mathcal{E}, \alpha)$, and $N_{e0}(\mathcal{E}_0, \alpha_0 | h)$ for any monoenergetic, monodirectional beam of precipitating electrons is now trivial using the ABS model. It is simply the characteristic response of the atmosphere, calculated as described in Sections 3.2 and 3.3.3 and then scaled by the number of input electrons.

The difficulty in calculating a full (hemispheric) response to this precipitation now comes in taking a distribution of once-backscattered electrons and determining which electrons (if any) mirror above the conjugate hemisphere (i.e., which electrons are half-trapped) and which precipitate into the conjugate hemisphere (some backscattering for a second time). In addition, because the once-backscattered distribution is no longer monoenergetic the second deposition and second backscatter calculations in the conjugate atmospheric need to be calculated from the full tabulated sets of $N_{eM}(\mathcal{E}_0, \alpha_0 | h)$ and $\Psi_M(\mathcal{E}_0, \alpha_0 | \mathcal{E}, \alpha)$. This is calculated as a superposition of $N_{e0}(\mathcal{E}_0, \alpha_0 | h)$ and $\Psi_0(\mathcal{E}_0, \alpha_0 | \mathcal{E}, \alpha)$ for each individual $(\mathcal{E}_0, \alpha_0)$ pair in the input (now the once backscattered distribution) and then scaled by the number of precipitating electrons within each corresponding bin.

Understanding the process of combining backscatter distributions for an arbitrary input is important because it is a key component necessary for calculating the backscatter due to a realistic distribution of incident electrons due to LEP (as discussed in Chapter 4). Mathematically, it can be expressed by interpreting Ψ_0 as the Green's function applied to the initial distribution of particles $\Psi_{\text{incident}}(\mathcal{E}, \alpha)$:

$$\Psi(\mathcal{E}, \alpha) = \iint \Psi_{\text{incident}}(\mathcal{E}_0, \alpha_0) \Psi(\mathcal{E}_0, \alpha_0 | \mathcal{E}, \alpha) \, d\mathcal{E}_0 \, d\Omega_0. \qquad (3.1)$$

A full mathematical description of the interpolation process is found in Appendix A and a description of the methodology for combining different backscatter distributions (evaluated on arbitrary energy grids) is found in Appendix B. Finally an explicit example for the process of combining different backscatter distributions is shown graphically in Figure B.1.

Having laid out the methodology for combining individual backscatter profiles for any arbitrary input distribution, it is now possible to demonstrate the full capabilities of the ABS model. The best way to discuss how all the important pieces fit together is to consider an example distribution as it backscatters between hemispheres. As in the rest of this chapter, the simplest case is also the best for illustrative purposes and the example input is ($\mathcal{E}_0$=0.3 MeV, α_0=78°). In addition, since the full hemispheric backscatter calculation requires knowledge of the magnetic field it is now necessary to specify a longitude and hemisphere where the initial interaction takes place. For this case the incident longitude is φ=235° **E/S** (conjugate point of the HAIL array in the Central United States, φ=260° **E/N**) and the full input is represented ($\mathcal{E}_0$= 0.3 MeV, α_0=78°, φ_0=235° **E/S**).

The process describing the hemispheric evolution of this distribution over the first complete cycle (initial incidence in the Southern Hemisphere, deposition/backscatter, incidence in the Northern Hemisphere, deposition/backscatter, and then subsequent incidence in the Southern Hemisphere) is shown in the six panels of Figure 3.19. The color bar shows the fluence of incident/backscattered electrons on a log scale while the abscissa of each panel is in energy ranging from 50–300 keV and the ordinates of each panel represent either the incident or backscattered pitch angle of the electrons. For the case of backscattered electrons (Figures 3.19a and 3.19d) the ordinates (α_{bs}) represent the pitch angle of electrons up-going as they exit the atmosphere at an altitude of 200 km, and for the case of incident electrons (Figure 3.19c and 3.19f) the ordinates (α_{in}) represent the pitch angle of electrons down-going as they enter the atmosphere at an altitude of 200 km. Finally, for the case of half-trapped electrons (Figure 3.19b) the ordinate (α_{ht-S}) represents the pitch angle of electrons at 200 km in the Southern Hemisphere (they can be thought of as either up-going or down-going since they are stably trapped and return to the 200 km altitude in the

Southern Hemisphere with an unchanged pitch angle between initial backscatter and re-incidence upon the Southern Hemisphere).

Figure 3.19a shows the initial backscatter from a monoenergetic, monodirectional beam of electrons incident at ($\mathcal{E}_0$=0.3 MeV, α_0=78°, φ_0=235° **E/S**). The dashed line represents the angle of the southern hemispheric loss cone while the solid line is the loss cone angle in the Northern Hemisphere transformed to the Southern Hemisphere and separates the portion of electrons which are half-trapped above the Northern Hemisphere (electrons above the solid line). Notice that this region contains the vast majority ($\sim$70%) of backscattered energy and that the expected deposition in the Northern Hemisphere (discussed in Section 3.6) is significantly reduced compared to the Southern Hemisphere. The half-trapped electrons (shown on an expanded scale in Figure 3.19b) traverse the magnetic field line to the Northern Hemisphere but mirror at or above an altitude of 200 km and return to the Southern Hemisphere.

At this longitude, the magnetic field in the Northern Hemisphere is stronger (at the same altitude of 200 km) and therefore the first adiabatic invariant dictates that those electrons inside both loss cones have a larger pitch angle at 200 km in the Northern Hemisphere than in the Southern Hemisphere. For this specific example, the portion of electrons in Figure 3.19a which backscatter with pitch angles between 0°–70° (shown by the solid line) broaden to a range of 0°–90° in the conjugate hemisphere.

It can be shown as a product of Liouville's theorem [e.g., *Walt*, 2005, p. 64] that the flux, $j(\mathcal{E}, \theta)$, along a field line between these two points is conserved. This is because the spreading in solid angle due to increasing B (which decreases the flux), is exactly counteracted by the converging magnetic field (concentrating the flux) and therefore the flux of electrons is constant along a field line. Since fluence is just the time-integrated flux, it is also conserved along the field line, but both are only constant in the direction perpendicular to the velocity of the electron. Since the input for the Monte Carlo simulations needs to be in terms of fluence, $J(\mathcal{E}, \alpha)$, per unit horizontal area (not area perpendicular to the velocity of the electron), it is necessary to compensate for the changing angle of the magnetic field as well as for the contraction of the flux tube.
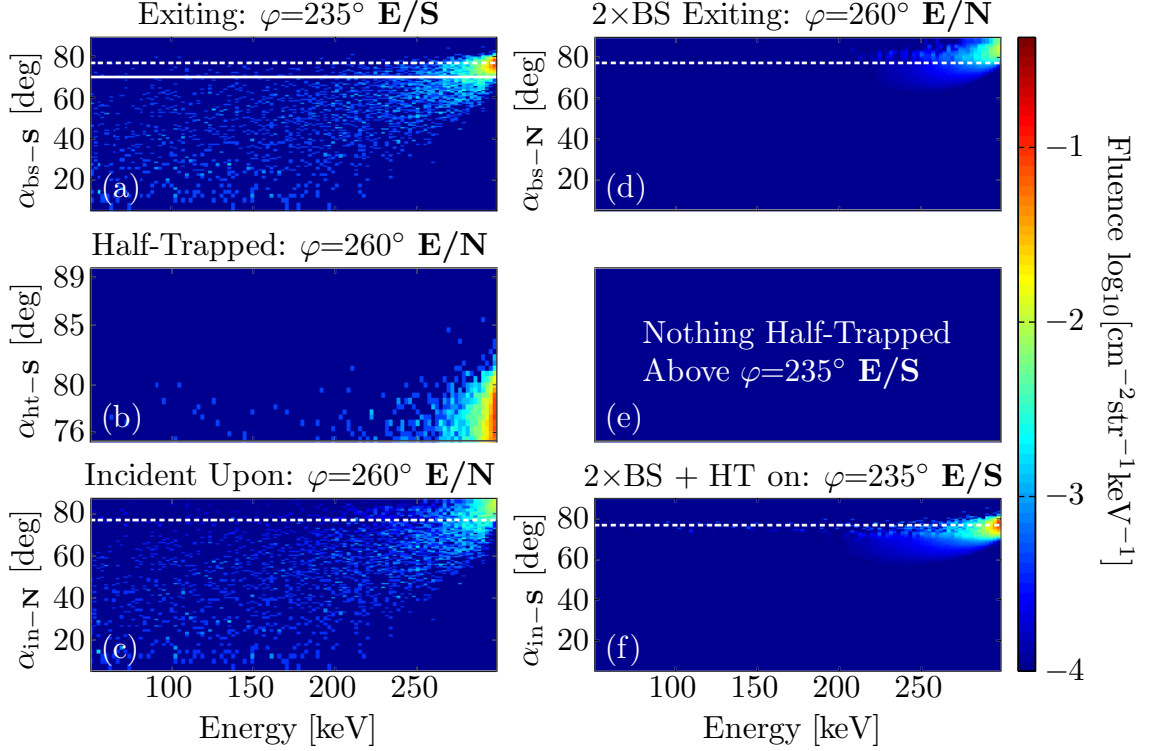
Figure 3.19: Evolution of a monoenergetic, monodirectional beam of electrons with an initial input of ($\mathcal{E}_0$=0.3 MeV, α_0=78°, φ_0=235° **E/S**). The abscissa of each plot shows the particle energy from 50–300 keV and the ordinates are pitch angle in degrees. The local loss cone is shown by the dashed line in each plot for reference and the color bar shows the fluence of backscattered electrons (on a log scale). (a) Initial backscattered distribution exiting the Southern Hemisphere at 200 km. The solid line corresponds to the northern hemispheric loss cone transformed to the Southern Hemisphere. (b) Half-trapped (above 200 km altitude in the Northern Hemisphere) electrons shown on a narrow pitch-angle range at an altitude of 200 km in the Southern Hemisphere. (c) Precipitating electrons at the conjugate point (φ=260° **E/N**) entering the Northern Hemisphere. (d) Backscattered electrons (now twice backscattered) exiting the Northern Hemisphere at an altitude of 200 km. (e) Portion of electrons exiting the Northern Hemisphere which are half-trapped above the Southern Hemisphere (empty because the loss cone in the Southern Hemisphere is larger at this longitude). (f) Combination of twice backscattered —panel (d)— and half-trapped —panel (b)— electrons now incident once again upon the Southern Hemisphere at 200 km.

The downward directed fluence can be calculated through scaling the fluence perpendicular to the electron velocity by a factor of $\cos\alpha\cos\theta_B$, where θ_B is the angle of the magnetic field with the vertical. Likewise, it is possible to relate the backscattered (upward traveling) fluence (per unit horizontal area) leaving one hemisphere to the input (downward traveling) fluence incident upon the conjugate hemisphere through the ratio:

$$\frac{J_d(\mathcal{E},\alpha_d)}{J_u(\mathcal{E},\alpha_u)} = \frac{\cos\alpha_d\cos\theta_{B_d}}{\cos\alpha_u\cos\theta_{B_u}} \tag{3.2}$$

where the u indicates upward traveling (i.e., backscattered electrons) and the d indicates downward traveling electrons in the conjugate hemisphere. Using Equation (3.2), the portion of the distribution below the solid horizontal line in Figure 3.19a is mapped to the Northern Hemisphere and incident upon the atmosphere, with pitch angles ranging from 0°–90°, as shown in panel Figure 3.19c.

Figure 3.19, panels (a) through (c) show the process of converting the backscatter in the Southern Hemisphere into an input distribution in the Northern Hemisphere. The next step is to employ the methodology described by Appendix B in conjunction with Equation (B.4) to calculate the twice-backscattered distribution, $\Psi_{\mathrm{bs2}}(\mathcal{E}_{\mathrm{bs2}},\,\alpha_{\mathrm{bs2}}|\mathcal{E},\alpha)$, due to this distribution of incident electrons, $\Psi_{\mathrm{bs1}}(\mathcal{E}_{\mathrm{bs1}},\,\alpha_{\mathrm{bs1}}|\mathcal{E}_{\mathrm{bs2}},\alpha_{\mathrm{bs2}})$. The result of this calculation is shown in Figure 3.19d (on the same color axis as for the other panels). Note that as expected, below the loss cone, there are significantly fewer electrons backscattered than above the loss cone. In fact, based upon this figure it appears that there is almost no backscatter for deep incidence electrons.

The full effect of the backscatter process is shown by Figure 3.20 which repeats the data of Figure 3.19, panels (c) and (d), but shows two additional orders of magnitude in the dynamic range of the color bar. The top panel of Figure 3.20 shows $\Psi_{\mathrm{bs1}}(\mathcal{E}_{\mathrm{bs1}},\,\alpha_{\mathrm{bs1}}|\mathcal{E}_{\mathrm{bs2}},\alpha_{\mathrm{bs2}})$ incident upon the northern hemisphere atmosphere (as a function of $\mathcal{E}_{\mathrm{bs2}}$ and α_{bs2}) and the bottom panel shows the twice backscattered electron distribution, $\Psi_{\mathrm{bs2}}(\mathcal{E}_{\mathrm{bs2}},\,\alpha_{\mathrm{bs2}}|\mathcal{E},\alpha)$, exiting the atmosphere. There are two primary features to note from this figure which cannot be seen from the corresponding panels in Figure 3.19. The first is that due to the methodology employed i.e., using an

atmospheric response $\Psi_0(\mathcal{E}_i, \alpha_j | \mathcal{E}_{\text{bs2}}, \alpha_{\text{bs2}})$ for each $\Psi_{\text{bs1}}[i, j]$, the calculated backscatter distribution is significantly smoother than that obtained by a typical Monte Carlo simulation. The second feature to note is that the amount of twice-backscattered fluence (especially below the loss cone) is two orders of magnitude lower and is therefore not seen in Figure 3.19d.

Returning to the discussion of the atmospheric backscatter cycle, Figure 3.19e shows that there are no half-trapped electrons above the Southern Hemisphere (because the southern hemispheric loss cone is larger) and the final step in completing a single 'backscatter cycle' is to combine the half-trapped electrons (Figure 3.19b) with the twice-backscattered distribution (Figure 3.19d). This combination is valid because (as discussed above in Section 3.4.2), the atmospheric backscatter time is negligible compared to the total hemispheric bounce period, so the twice-backscattered electrons and the half-trapped electrons remain relatively bunched together throughout the backscatter process. The two distributions (Figures 3.19b and 3.19d) can be easily combined because as the distribution in Figure 3.19d traverses the magnetic field line back to the Southern Hemisphere the magnetic field strength decreases, and the twice-backscattered fluence (which exits the Northern Hemisphere spanning the pitch angle range from 0°–90°) contracts to span the pitch angle range of 0°–70° in the Southern Hemisphere. In addition, the fluence contained within each bin scales according to Equation (3.2) (this time with α_u, α_d and θ_u, θ_d reversed).

The final combination of the twice-backscattered and the half-trapped electrons is shown in Figure 3.19f where it is incident upon the southern hemisphere atmosphere. This new input distribution now progresses through the same process just described. With each atmospheric interaction some (dynamically changing) percentage of the total energy fluence is backscattered or deposited until all the energy is gone or the amount remaining is below the background diffusion precipitation rate.

3.6 Geographic Variation of $N_{\text{e}}(\mathcal{E}, \alpha | h)$ and $\Psi(\mathcal{E}, \alpha | \mathcal{E}, \alpha)$

Having finally detailed the ABS model in terms of deposition, backscatter, magnetic dip angle, hemispheric bounce period, interpolation, and shown a single complete
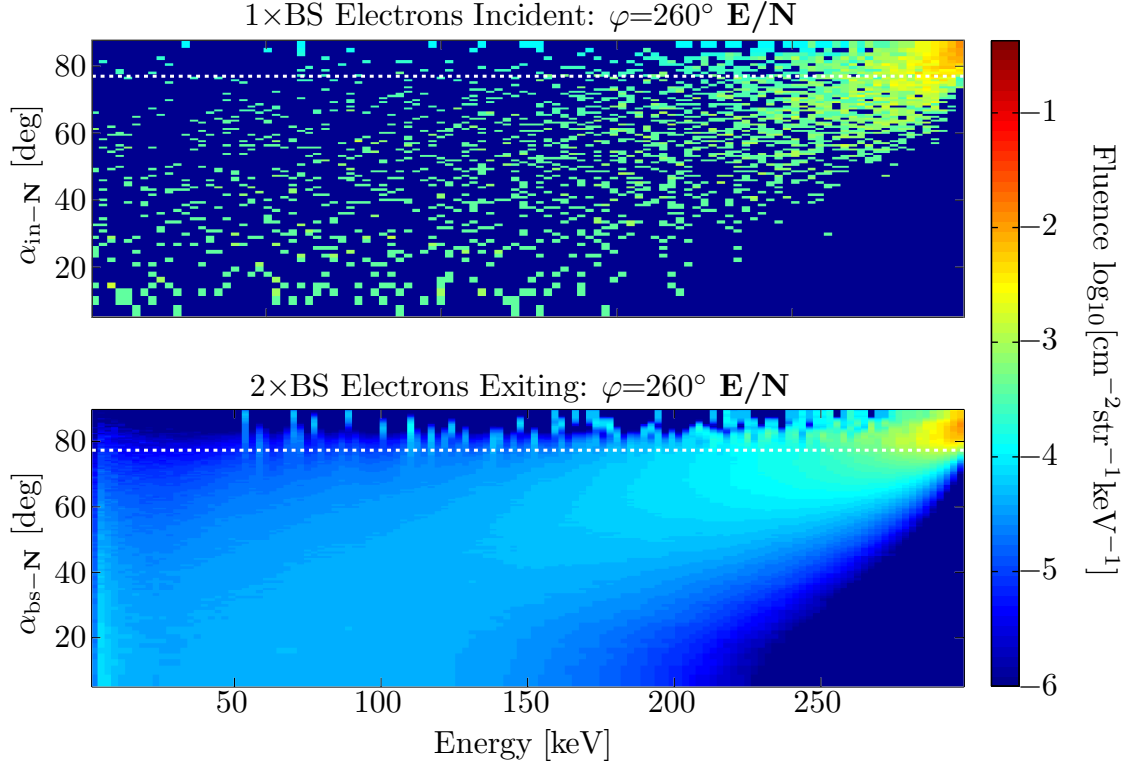
Figure 3.20: Conjugate backscatter calculation for an initial input of ($\mathcal{E}_0 = 0.3\,\mathrm{MeV}$, $\alpha_0 = 78°$, $\varphi_0 = 235°$ **E/S**). The top panel shows the portion of the initial backscattered distribution $\Psi_{\mathrm{bs1}}(\mathcal{E}_{\mathrm{bs1}}, \alpha_{\mathrm{bs1}}|\mathcal{E}, \alpha)$ which reaches the conjugate point ($\varphi=260°$ **E/N**) in the Northern Hemisphere. The bottom panel shows the twice backscattered distribution of electrons, $\Psi_{\mathrm{bs2}}(\mathcal{E}_{\mathrm{bs2}}, \alpha_{\mathrm{bs2}}|\mathcal{E}, \alpha)$ exiting the atmosphere. In both panels the dashed white line indicates the local loss cone angle and the color bar shows the fluence of backscattered electrons, including two additional orders of magnitude in dynamic range compared to Figure 3.19.

backscatter cycle it is now possible to demonstrate the full potential of the ABS model by predicting the observable effects of precipitating electrons in both hemispheres and as a function of longitude.

3.6.1 Hemispheric Variation

As discussed briefly in Section 2.2.2, the effect of backscatter is dominant in the hemisphere where the loss cone angle is smaller because absent the case of very large pitch angle scattering (or closely spaced loss cones), the hemisphere with a smaller loss cone cannot have precipitation until backscattered electrons arrive from the conjugate hemisphere. With the inclusion of atmospheric backscatter it is evident that observed LEP event characteristics vary with longitudes/hemisphere. The best illustration of these differences is the evolution of an incident distribution of electrons as it repeatedly follows the atmospheric backscatter cycle discussed in Section 3.5.

This concept is illustrated in Figure 3.21, continuing the evolution of the distribution shown in Figure 3.19. The evolution of the electron distribution is shown over the first six interactions with the atmosphere (three in each hemisphere). The abscissae show energy (in keV) and the ordinates show the pitch angle of both precipitating and backscattered electrons together on the same axis (at an altitude of 150 km, $\alpha_{150\text{km}}$) where precipitating electrons are shown with pitch angles between 0°–90° and backscattered electrons are shown with pitch angles between 90°–180° (i.e., $\alpha_{\text{bs}} = 180° - \alpha_{\text{in}}$). Additionally, in each panel the border between precipitating and backscattered electrons is shown by the dashed line (at 90°) for easy reference and the color bar shows the fluence of electrons (on a log scale). Note also that at 150 km the local loss cone angle is ∼82°.

The top row of Figure 3.21 shows the electrons in the Southern Hemisphere at a longitude of 235° **E/S** and the bottom row shows the electrons at the conjugate point of 260° **E/N**. Each column indicates the interaction number (κ) which designates the total number of times the electrons have interacted with the atmosphere (1, 3, 5, ... in the Southern Hemisphere and 2, 4, 6, ... in the Northern Hemisphere). Additionally, in the hemisphere with the larger loss cone (the Southern Hemisphere in this case) the
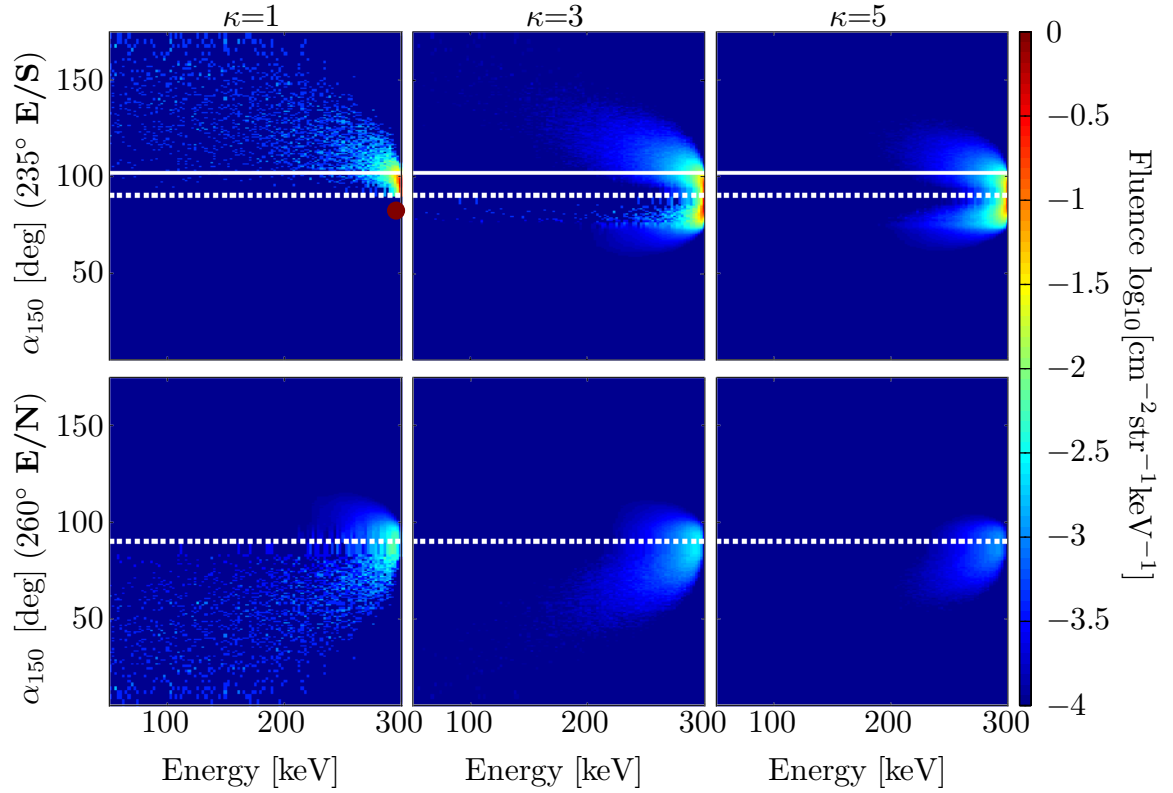
Figure 3.21: Evolution of a monoenergetic, monodirectional beam of electrons with an initial input of ($\mathcal{E}_0$=0.3 MeV, α_0=78°, φ_0=235° **E/S**) as shown by the solid dot in the top-left panel. The top row shows the fluence in the Southern Hemisphere while the bottom row shows the Northern Hemisphere fluence. Each panel shows the incident and backscattered fluence of electrons with κ indicating the total number of atmospheric interactions. The abscissae show energy (in keV) and the ordinates show the pitch angle of both precipitating and backscattered electrons together on the same axis (at an altitude of 150 km, $\alpha_{150\text{km}}$) where precipitating electrons are shown with pitch angles between 0°–90° and backscattered electrons are shown with pitch angles between 90°–180°. The dotted line in each plot is at 90° to help differentiate between precipitating (0°–90°) and backscattered (90°–180°) electrons. The solid line in the top row shows the angle of the northern hemispheric loss cone transformed to the Southern Hemisphere and demarcates the portion of electrons which are half-trapped above the Northern Hemisphere (backscattered electrons with pitch angle above 90° and below the solid line). The color bar shows the fluence of backscattered electrons (on a log scale).

solid line indicates the portion of particles which are half-trapped above the conjugate hemisphere (note that unlike Figure 3.19 the local loss cone angle is not indicated). In these figures (and subsequent atmospheric backscatter calculations) the definition of half-trapped is expanded slightly so that any electron which mirrors at an altitude of 200 km or lower is input into the atmosphere to ensure that all atmospheric effects on precipitating electrons are accounted for. Additionally, in order to limit computational requirements, energy which is deposited as secondary ionization at altitudes above ∼130 km, and electrons backscattered with energy ≤50 keV are not included in subsequent atmospheric interactions (though their contribution is accounted for in terms of conservation of total energy).

In the top-left panel of Figure 3.21, the large dot shows the energy and pitch angle of the example monoenergetic precipitation input as it is incident on the atmosphere at 150 km. The backscattered distribution is shown in the same panel above the dashed line. As indicated by the solid horizontal line, only those electrons with pitch angles above ∼102° are below the loss cone in both hemispheres, so only these electrons are incident in the Northern Hemisphere as shown in the bottom-left panel. As discussed in reference to Figure 3.19, because the magnetic field strength in the Northern Hemisphere is larger than in the Southern Hemisphere, the backscattered electrons leaving the Southern Hemisphere with pitch angles of 102°–180° (corresponding to 0°–78°) broaden to a range of 0°–90° in the conjugate hemisphere and scale in fluence as shown by Equation (3.2).

Recall from Section 3.3.1 that $\Psi_0(\mathcal{E}_0, \alpha_0 | \mathcal{E}, \alpha)$ can vary significantly with input energy and pitch angle. It is therefore necessary to calculate the response of every input $(\mathcal{E}_0, \alpha_0)$ individually and to combine their response into a single distribution as summarized in Equation (B.4). The ABS model calculates $\Psi_{\text{bs2}}(\mathcal{E}_{\text{bs2}}, \alpha_{\text{bs2}} | \mathcal{E}, \alpha)$ by interpolating between specifically calculated $(\mathcal{E}_0, \alpha_0)$ pairs and combining the results of the backscatter distribution for each $\Psi_0(\mathcal{E}_i, \alpha_j | \mathcal{E}_{\text{max}}, \alpha)$ in the input distribution onto the same grid. As expected, only those electrons which are near the local loss cone angle experience significant backscatter. The rest are deposited and lost from the magnetospheric system, as seen by comparing the incident and backscattered distributions in the bottom-left panel of Figure 3.21.

The electrons which are half-trapped (90°–102° in the top-left panel) mirror at an altitude above 200 km and are not considered in the Northern Hemisphere backscatter calculation, instead they return to the Southern Hemisphere where they combine with the (now) twice backscattered electrons, $\Psi_{bs2}(\mathcal{E}_{bs2}, \alpha_{bs2}|\mathcal{E}, \alpha)$. The combined distribution is then incident once again upon the Southern Hemisphere (top row, center panel). This process repeats until all electrons are lost from the magnetosphere as seen in subsequent panels. It is evident from this evolution that at this longitude there is significantly more precipitation in the Southern Hemisphere than in the Northern Hemisphere.

Note that the ABS model provides a specific and calculable relationship between the fluence incident in the two hemispheres, $\Psi_{in,\mathbf{S}}(\mathcal{E}, \alpha)$ and $\Psi_{in,\mathbf{N}}(\mathcal{E}, \alpha)$ (linking them), so that knowledge (or measurements) of an electron distribution (or deposition profile) in one hemisphere also provides valuable information about the electron distribution in the conjugate hemisphere, even in the absence of direct observations. In many cases, these measurements are from VLF remote sensing so while the atmospheric backscatter determines the evolution of electrons in the magnetosphere, it is the secondary ionization created in the ionosphere which is reliably observed. These deposition profiles can therefore be used to predict systematic differences between the characteristics of LEP events in different hemispheres, or at varying longitudes as shown in the next section.

3.6.2 Longitudinal Variation

The previous section showed the hemispheric differences in the evolution of $\Psi_{in}(\mathcal{E}, \alpha)$ due to the Earth's asymmetric magnetic field. This section shows how this asymmetry also affects precipitation at different longitudes. For example, at $\varphi_1 = 235°$ $\mathbf{E/S}$, the loss cones are relatively close together ($\Delta\alpha_{eq}^{lc} \simeq 0.4°$, as shown in Figure 2.3b), however at longitudes where the loss cones are further apart such as at $\varphi_2 = 295°$ $\mathbf{E/S}$ ($\Delta\alpha_{eq}^{lc} \simeq 1.5°$), the results are significantly different despite an identical input. This contrast is shown in Figure 3.22 which shows $N_e(\mathcal{E}, \alpha|h)$ as a function of altitude, with one deposition profile for each atmospheric interaction, κ. Panels (a) and (c) show the
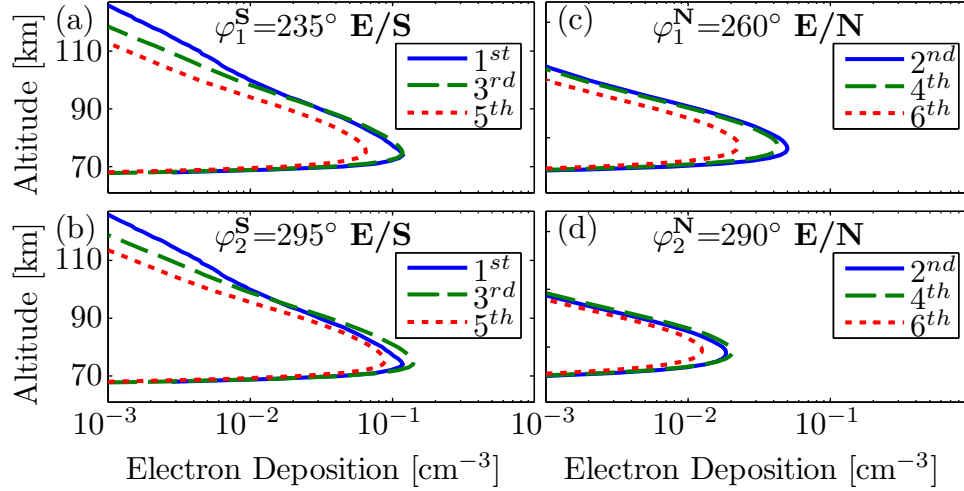
Figure 3.22: Electron density profiles as a function of altitude for the first six atmospheric interactions of a monoenergetic beam of electrons ($\mathcal{E}_0$=0.3 MeV, α_0=78°) incident first on the Southern Hemisphere. (a) Evolution of deposition at $\varphi_1^{\mathbf{S}}$=235° $\mathbf{E/S}$. (b) Evolution of deposition for the same input at $\varphi_2^{\mathbf{S}}$=295° $\mathbf{E/S}$. (c) Deposition at the conjugate point of the first longitude $\varphi_1^{\mathbf{N}}$=260° $\mathbf{E/N}$. (d) Deposition at conjugate the point of the second longitude $\varphi_2^{\mathbf{N}}$=290° $\mathbf{E/N}$.

deposition profiles for electrons initially incident at $\varphi_1^{\mathbf{S}}$=235° $\mathbf{E/S}$ (corresponding to Figure 3.21), and panels (b) and (d) show the deposition profiles for the same initial distribution of electrons incident at $\varphi_2^{\mathbf{S}}$=295° $\mathbf{E/S}$, with each panel showing the first three depositions at each location.

Notice that the first deposition in the Southern Hemisphere, $N_{\mathrm{e}1}(\mathcal{E}, \alpha|h)$, is nearly identical at both longitudes. As previously discussed this result comes about because backscatter from the atmosphere is primarily determined by the neutral density. The differences in subsequent depositions in the Southern Hemisphere, $N_{\mathrm{e}3}(\mathcal{E}, \alpha|h)$ and $N_{\mathrm{e}5}(\mathcal{E}, \alpha|h)$, are a result of the differing range of half-trapped electrons at the two longitudes. In the Northern Hemisphere at φ_2, the portion of electrons which are half-trapped is significantly higher than at φ_1, which translates to about twice as much deposition in the Northern Hemisphere (for $\kappa = 2, 4, 6$) at $\varphi_1^{\mathbf{N}}$ than at $\varphi_2^{\mathbf{N}}$. The fact that there is such a significant difference between the deposition profiles (due to an identical input) at different longitudes indicates that subionospheric VLF remote

sensing of D-region disturbances can likely be used to investigate differences in LEP event characteristics at varying longitudes (discussed further in Section 4.2).

3.7 Summary

This chapter has detailed the Atmospheric Backscatter model, which is based upon $\sim$16,000 $(\mathcal{E}_0, \alpha_0)$ pairs, individually calculated by a Monte Carlo model of atmospheric physics. The ABS model determines characteristic deposition profiles and backscatter distributions: $N_{e0}(\mathcal{E}_0, \alpha_0|h)$, and $\Psi_0(\mathcal{E}_0, \alpha_0|\mathcal{E}, \alpha)$ due to each input $(\mathcal{E}_0, \alpha_0)$ pair and takes advantage of kernel density estimation techniques in limiting the necessary computational resources. The ABS model additionally accounts for the asymmetric magnetic field in the form of longitudinal and hemispheric variations in the loss cone angle. Even accounting for the longitudinally varying loss cone angle, without the effects of atmospheric backscatter the characteristics of LEP events would be similar at different locations. This is true despite the fact that the population of electrons at the edge of the loss cone is similar at different longitudes [e.g., *Selesnick et al.*, 2003]. However, when atmospheric backscatter is considered, the characteristics of LEP events should be different at varying longitudes because of the difference between hemispheric loss cones.

With the details of the ABS model specified, and a background laid for the capabilities of the ABS model, the next chapter makes use of previous work to calculate a representative distribution of incident electrons, $\Psi_{\mathrm{LEP}}(\mathcal{E}, \alpha)$ as an input to the ABS model at varying longitudes, with the goal of predicting and quantifying observable differences in LEP event characteristics at different longitudes and hemispheres thus quantifying the loss of radiation belt electrons on a global scale.

Chapter 4

Modeling LEP Event Characteristics

The previous chapters describe how the backscatter and deposition of electrons can vary as a function of energy and pitch angle, as well as how the asymmetry of the Earth's magnetic field affects the evolution of backscattered electrons. With this background it is now possible to use the ABS model to investigate the evolution of a realistic distribution of precipitating electrons calculated using a complete wave-particle interaction model as detailed in *Bortnik et al.* [2006a,b].

4.1   Whistler-Induced Particle Precipitation Model

The complete modeling of electron precipitation due to lightning requires sophisticated models of lightning discharge electromagnetic pulse waveforms [e.g. *Cummer*, 1997, and references therein], transionospheric propagation (coupling) of VLF waves [*Helliwell*, 1965], magnetospheric wave propagation [e.g. *Inan and Bell*, 1977], magnetospheric particle motion [e.g. *Walt*, 2005] and wave-particle interactions [e.g. *Inan et al.*, 1978, 1989; *Bell*, 1984], as well as other knowledge of radiation belt particle and wave dynamics.

Previous work by *Peter and Inan* [2007] has shown that a forward modeling approach can be successful in determining the amplitude characteristics of individual

LEP events. However, the present work focuses on the systematic differences which are statistically observed in LEP event characteristics at different longitudes. To accomplish this task it is necessary to calculate a realistic input distribution of precipitating electrons for input into the ABS model at various longitudes. The input distribution is calculated by the whistler-induced particle precipitation (WIPP) model of *Bortnik et al.* [2006a,b], which calculates the pitch angle scattering due to a representative lightning flash.

To make comparison with previous work as easy as possible, the same input parameters are used as in *Peter and Inan* [2007, Figure 7, Case 1]. In this case the +133 kA cloud-to-ground causative lightning flash was located at 33.34° **N**, 260° **E**. At latitudes of $\pm 10°$ surrounding the causative flash, the lightning energy is coupled through the ionosphere to an altitude of 1000 km using attenuation coefficients from *Helliwell* [1965, Figure 3-35]. Once the wave energy is in the magnetosphere the WIPP model calculates 41 ray paths for each of 130 frequency components ranging from 200 Hz to 60 kHz (spaced roughly logarithmically), resulting in 5330 total rays. The ray paths are calculated using a cold plasma density model based upon the work of *Tarcsai et al.* [1988], and then interpolated every 0.01° in latitude and every 1 Hz in frequency for a total of ~ 120 million rays. These rays are assumed to enter the magnetosphere with vertical wave-normal angles, due to the horizontally stratified sharp edge of the lower ionosphere. The pitch angle scattering of electrons is calculated using the previously discussed gyro-resonance condition [e.g., *Chang and Inan*, 1983], for each harmonic resonance mode ranging from -5 to 5. This calculation is carried out for each frequency component, accounting for particle scattering contributions at geomagnetic latitudes of $-40°$ to $40°$ and for energy components within a factor of two around the resonant energy.

The result of this calculation is a pitch angle change as a function of energy and time, with each pitch angle change referred back to the equator using the first adiabatic invariant. The WIPP model then accounts for the travel time to the ionosphere for each electron bunch and the root-mean-square (rms) pitch angle change is placed in the appropriate $\mathcal{E}$-t bin. The pitch angle scattering for Case 1 of *Peter and Inan*

[2007] is shown in Figure 4.1a where the abscissa shows time (in seconds), the ordinate shows the energy of resonant electrons and the color bar shows the equatorial rms pitch angle change ($\Delta\alpha_{\mathrm{eq}}^{\mathrm{rms}}$). The portion of the figure highlighted by the black box (i.e., 0.1 MeV–0.3 MeV, and 0–5 s) indicates the portion of the overall calculation which is used as an input into the ABS model. The chosen energy range is a representative sample of electrons which are typically involved in the production of LEP events [*Voss et al.*, 1998] and the chosen time range matches previous work [*Peter and Inan*, 2007]. Though not evident from Figure 4.1a, further analysis by *Peter* [2007, Figure 4.1b] shows that the majority of 0.1–0.3 MeV precipitation is incident upon the atmosphere within the first second.

The next step is to convert the $\mathcal{E}$-t calculation of rms pitch angle change to a distribution of precipitating electrons. In order to do this it is necessary to know the pitch angle distribution of the trapped magnetospheric electrons. Since this distribution is not typically known a priori, it is assumed to be either a square-shaped distribution (a step function, with a sharp cutoff at the loss cone) or a more realistic sine-shaped distribution (where the electron density is zero below the loss cone and increases as $\sin\alpha_{\mathrm{eq}}$ above the loss cone). In either case the loss cone angle is defined as the larger of the northern and southern hemispheric loss cones. The probability density function (PDF) of the new (scattered) pitch angle distribution is then calculated as shown in *Bortnik et al.* [2006a, Figure 10]. This PDF represents the scattering distribution and is calculated for each time and at each energy. The contributions are superimposed to form a single scattered pitch angle PDF at each energy. An example of a single (normalized) PDF based upon an initially square pitch angle distribution is shown in Figure 4.1b, indicating both the initial and scattered equatorial distributions. Figure 4.1c shows the distribution mapped to an altitude of 200 km using the first adiabatic invariant (not accounting for the dip angle of the magnetic field or the contraction of the flux tube from the equator to 200 km). Note that because the goal is to model an impulsive injection of electrons, only electrons below the local loss cone (vertical dashed line) are considered to be incident upon the atmosphere. The final step is to scale the distribution to a realistic population. While the actual population of radiation-belt electrons can vary significantly based upon geomagnetic conditions
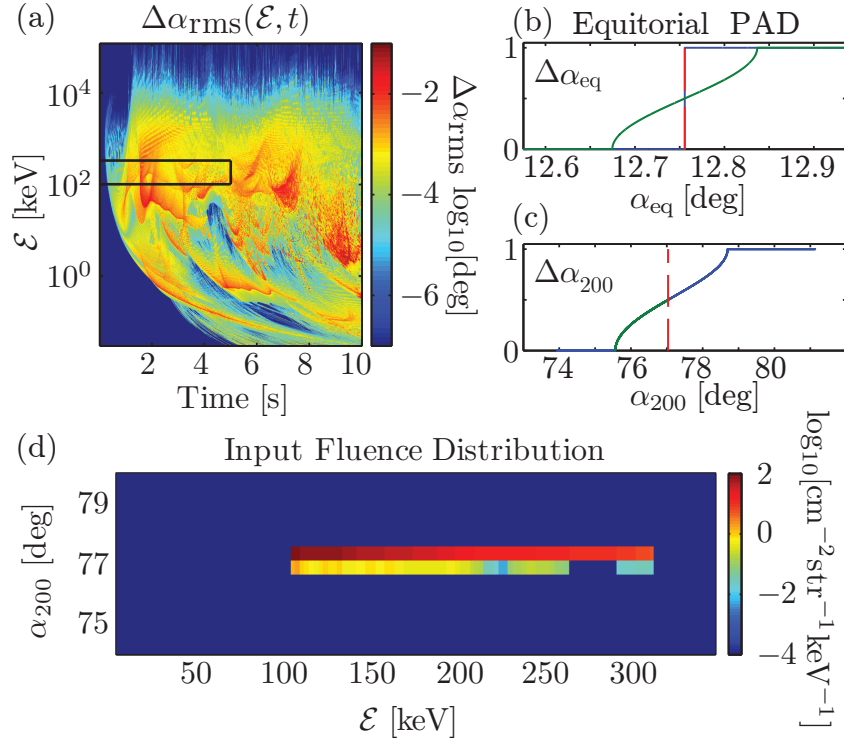
Figure 4.1: Results from a model of whistler interaction with energetic electrons [*Bortnik et al.*, 2006a,b], calculated to give a realistic distribution of electrons between 0.1 MeV and 0.3 MeV incident upon the atmosphere as the result of a whistler interaction. (a) Change in equatorial pitch angle ($\Delta\alpha_{\mathrm{rms}}$) as a function of energy and time. (b) Example probability density function based upon a square loss cone at the equator. (c) Same example PDF transformed to the altitude of input into the ABS model (not showing fluence change from equator to 200 km). (d) Scaled (AE8) distribution of precipitating electron fluence input into the ABS model.

[e.g., *Nagai*, 1988], the goal of this dissertation is to compare LEP signatures at different longitudes, under similar conditions and therefore the exact available flux of electrons is not of great importance. However, to simplify the comparison to past work [*Bortnik et al.*, 2006a,b; *Peter and Inan*, 2007] the distribution is scaled using the AE8 MAX radiation belt model [*Vette*, 1991] and the final input distribution is shown in Figure 4.1d as a function of both energy and pitch angle.

Figure 4.1 shows the calculation method for a specific input; however, because the whistler-interaction model uses a dipole model for Earth's magnetic field and refers all pitch angle changes back to the magnetic equator, the same pitch angle scattering calculation may be used at different longitudes by specifically accounting for the longitudinal and hemispheric variations of the Earth's magnetic field as they are manifested in the loss cone angle (as shown in Figure 2.3). These differences are incorporated into the input distribution as shown in Figure 4.1c and Figure 4.1d.

4.2   LEP Event Backscatter and Deposition Calculations

The process described above in conjunction with Figure 4.1 is based entirely on previous work, but is just the first step in calculating the characteristics of LEP events. In this section the calculated equatorial pitch angle distribution is used as an input into the ABS model for causative lightning flashes located at $L = 2.5$ and longitudes of $\varphi_1^{\mathbf{N}}$=260° $\mathbf{E/N}$ and $\varphi_2^{\mathbf{N}}$=290° $\mathbf{E/N}$ (chosen for comparison with LEP event data recorded at those longitudes as discussed in Section 2.3.2). The expected LEP event characteristics are calculated from the results of the evolution of the backscatter and deposition as shown in Figures 4.2 and 4.3, respectively. Figure 4.2 shows the first four backscatter calculations (two in each hemisphere) for both longitudes as a function of energy and pitch angle at an altitude of 150 km (i.e., $\alpha_{150\mathrm{km}}$). The top row of Figure 4.2 shows precipitating and backscattered electrons in the Northern Hemisphere and the bottom row precipitating and backscattered electrons in the Southern Hemisphere.
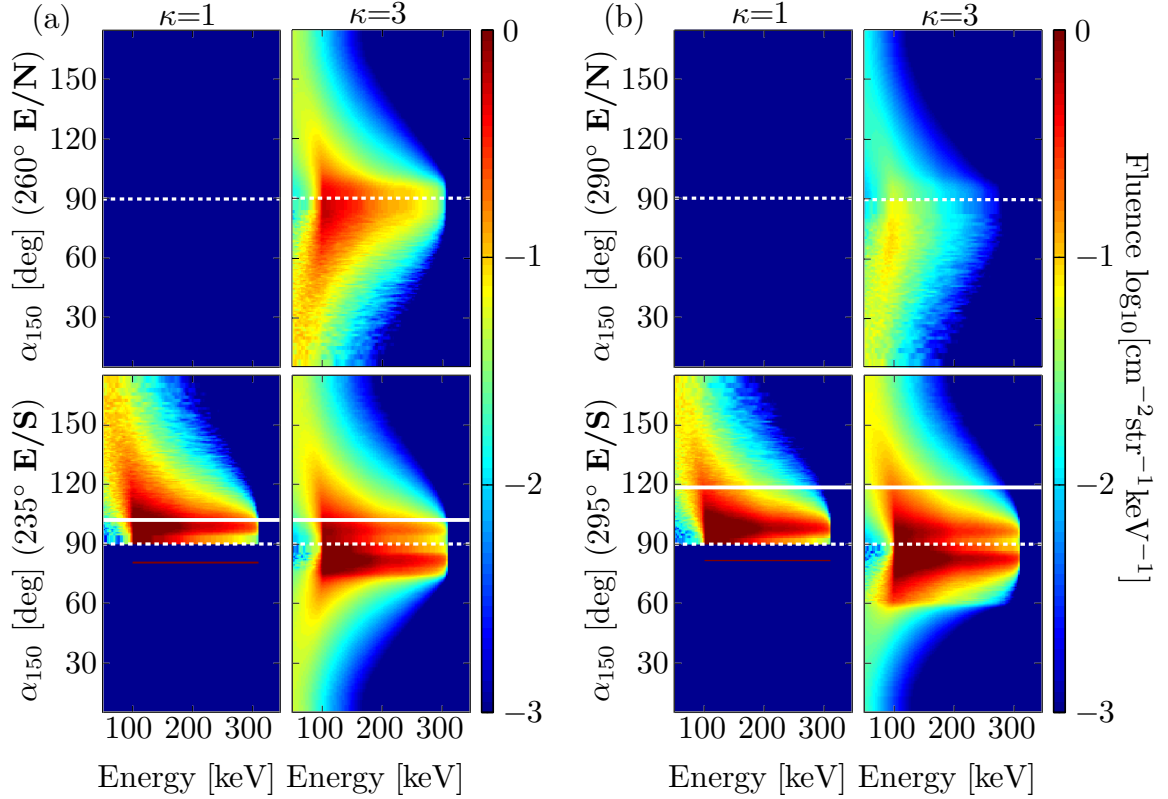
Figure 4.2: Longitudinal dependence of electron backscatter between hemispheres. Similar to Figure 3.21, the abscissae show energy in keV, the ordinates show pitch angle in degrees at an altitude of 150 km and the color bar shows fluence in units of $cm^{-2}str^{-1}keV^{-1}$. The dashed line at 90° separates precipitating electrons (below 90°) and backscattered electrons (above 90°). The solid line in the bottom row (Southern Hemisphere) shows the northern hemispheric loss cone angle transformed to the Southern Hemisphere and separates electrons half-trapped above the Northern Hemisphere (between 90° and the solid line) from electrons which reach the Northern Hemisphere. (a) Electrons initially incident at 260° **E/N**. (b) Electrons initially incident at 290° **E/N**.
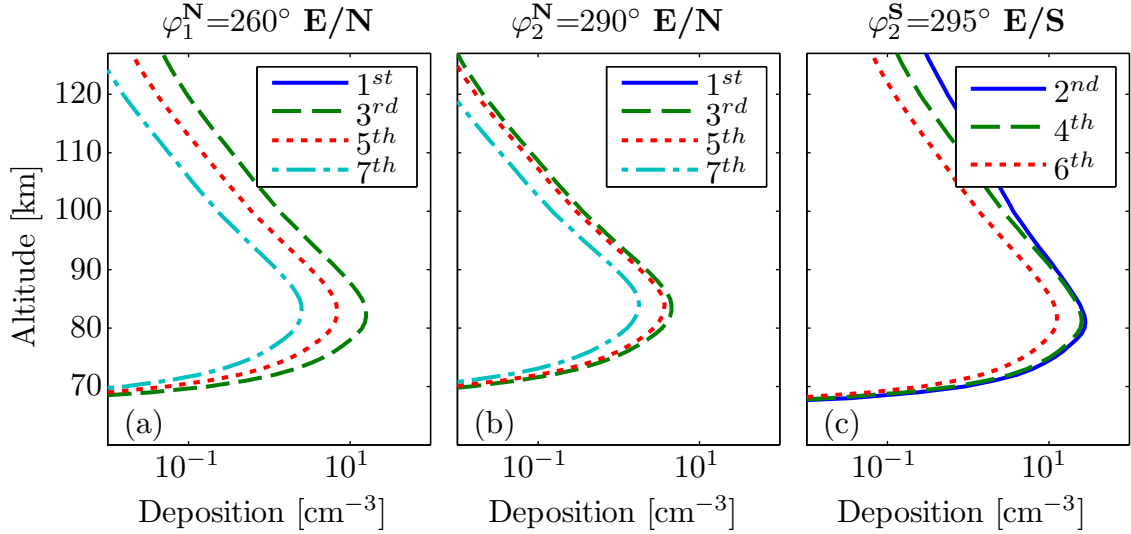
Figure 4.3: Electron deposition profiles as a function of altitude for the atmospheric interactions (corresponding to Figure 4.2) in both hemispheres. (a) Electron deposition profiles created at $\varphi_1^{\mathbf{N}}=260°$ $\mathbf{E/N}$. (b) Electron deposition profiles created at $\varphi_2^{\mathbf{N}}=290°$ $\mathbf{E/N}$. (c) Electron deposition profiles created at $\varphi_2^{\mathbf{S}}=295°$ $\mathbf{E/S}$.

The evolution of the backscattered distribution of electrons determines the timing, energy and pitch angle of electrons incident upon the conjugate atmosphere; however, it is the deposition profile (i.e., change in electron density due to deposited electrons) which is observed using VLF remote sensing. These variations in electron density deposition result in differences in the characteristics of observed LEP events. Figure 4.3 shows the electron density profile calculations which are carried out in conjunction with the backscatter calculation for each of the three locations with a separate curve corresponding to each atmospheric interaction $\kappa=1$–7 (the first four of which are shown in Figure 4.2).

4.3 Prediction of LEP Characteristics

4.3.1 Onset Delay (Δt)

The first feature to notice from Figures 4.2 and 4.3 is that there is no initial backscatter or deposition from the first atmospheric interaction in the Northern Hemisphere

(κ=1). This result can be seen by noting that the top-left panels of Figure 4.2a and 4.2b are empty and also by noting that there is no solid curve in either Figure 4.3a or 4.3b. This lack of initial precipitation is due to the fact that at both longitudes, the southern hemispheric loss cone is larger and the population of (counter-streaming) electrons which are initially scattered into the loss cone are still half-trapped above the Northern Hemisphere. The electrons mirror at an altitude above 200 km and traverse the magnetic field line to the Southern Hemisphere (where they are now below the local loss cone) and are incident upon the southern hemisphere atmosphere as shown in the bottom-left panels of Figure 4.2a and 4.2b. Some electrons are then deposited (as shown by the solid curve corresponding to κ=2 in Figure 4.3c) and others are backscattered, returning to the Northern Hemisphere where those electrons which are inside the northern hemispheric loss cone (above the solid line in the bottom row of Figure 4.2) are incident upon the northern hemisphere atmosphere. The resulting deposition is shown by the long-dashed curve (κ=3) in Figure 4.3a and 4.3b.

The fact that there is no deposition in the Northern Hemisphere until the κ=3 interaction means that an LEP event observed at $\varphi_1^{\mathbf{N}}$ or $\varphi_2^{\mathbf{N}}$ has an onset delay (Δt) which is increased by one extra bounce period (τ_{b}) between the causative lightning flash and the onset of the LEP event as previously predicted [*Voss et al.*, 1998; *Peter and Inan*, 2007]. Likewise, the fact that there there is energy deposited into the southern hemisphere atmosphere on the κ=2 interaction (as shown in Figure 4.3c) means that LEP events observed at $\varphi_2^{\mathbf{S}}$ (caused by northern hemispheric lightning) have an onset delay time which is $\frac{1}{2}\tau_{\mathrm{b}}$ shorter than corresponding LEP events in the Northern Hemisphere.

Based upon the bounce period calculation discussed in Section 3.4.2, these values indicate that the onset delay in the Northern Hemisphere ($\Delta t_{\mathbf{N}}$) is increased by $\tau_{\mathrm{b,min}}$=0.3 s while the onset delay in the Southern Hemisphere ($\Delta t_{\mathbf{S}}$) is decreased by $\frac{1}{2}\tau_{\mathrm{b,min}} = 0.15$ s (with respect to the northern hemispheric delay time). Combined with the modeling work of *Peter and Inan* [2007] this result indicates onset delay times of $\Delta t_{\mathbf{N}}$=0.7 s, and $\Delta t_{\mathbf{S}}$=0.55 s.

4.3.2 Perturbation Magnitude (ΔA)

Another important feature to note when comparing the backscatter and deposition results for the two cases is that there is a significantly lower total energy fluence incident at $\varphi_2^{\mathbf{N}}$ than at $\varphi_1^{\mathbf{N}}$ which can be seen by comparing the top-right panels (between 0° and 90°) of Figure 4.2a and 4.2b. This lower total incident energy fluence also results in significantly different deposition profiles at the two longitudes and can also be seen by comparing the deposition profiles at the two longitudes, (long-dashed curves) in Figure 4.3a and 4.3b where the total electron density enhancement at $\varphi_1^{\mathbf{N}}$ is more than twice as large as that at $\varphi_2^{\mathbf{N}}$. The physical reason for these differences is the asymmetry of the Earth's magnetic field. As shown by the solid lines in each bottom-row panel of Figure 4.2, a significantly larger portion of electrons are half-trapped above the Northern Hemisphere at $\varphi_2^{\mathbf{N}}$ than at $\varphi_1^{\mathbf{N}}$. At $\varphi_1^{\mathbf{N}}$ the difference between the northern and southern loss cones (at the altitude of 150 km shown) is $\sim$15°, whereas at $\varphi_2^{\mathbf{N}}$ the difference is $\sim$30°.

Similar longitudinal differences in LEP event precipitation magnitude and occurrence rate were previously predicted by *Inan et al.* [1988c]. Rather than assuming an empty loss cone, their approach presumed (based upon satellite measurements) that the population of trapped electrons available for scattering would vary (with longitude and hemisphere) according to $\Delta\alpha_{\mathrm{eq}}^{\mathrm{lc}}$. While the initial approach was different, the net result is similar to that shown in the present work. Their predictions of higher LEP event occurrence rate and event magnitude over the Central/Western United States compared to the East Coast are similar to that presented here (assessed quantitatively below).

Without significant further modeling (beyond the scope of this dissertation) it is not possible to calculate the expected amplitude perturbation for the above deposition profiles; however, considering the fact that there is a significant difference between the deposition profiles means that there should (on average) be a longitudinal variation in the observed amplitude change of LEP events.

As discussed at length in Section 2.1.1, the observed perturbation magnitude of a VLF signal due to scattering by an ionospheric disturbance is a complicated function of the ambient electron density, as well as the relative location of the disturbance

region between the transmitter and receiver. However, it is possible to qualitatively estimate the magnitude of the signal perturbations by noting that in a statistical sense, the larger the disturbance (i.e., the more secondary ionization created) the larger (on average) the observed LEP event will be. Of course this observation assumes that the GCPs in the experimental setup are similar, but for $\varphi_1^{\mathbf{N}}$ and $\varphi_2^{\mathbf{N}}$ this is a good assumption because both are nearly directly north-south. Additionally, both are relatively short paths (i.e., $\lesssim 2$ Mm) and are therefore similar enough for a direct comparison. Comparing the deposition profiles in Figure 4.3a and Figure 4.3b it is apparent that there is a significant difference in the amount of secondary ionization created at the two locations (a factor of ~ 3.5) and this should in general lead to larger LEP events in the Central United States compared to the East Coast of the United States.

The path from NPM to Palmer Station, Antarctica on the other hand is ~ 10 Mm, and therefore direct comparison between the deposition profiles at $\varphi_2^{\mathbf{S}}$ with the two northern hemispheric locations is not possible. However, it is clear from Figure 4.3c that the deposition in the Southern Hemisphere (i.e., $\kappa = 2$, 4, 6) is significantly larger than the deposition in the Northern Hemisphere (at either longitude) and while a direct comparison is not likely to be accurate, it seems logical that the amplitude changes observed at $\varphi_2^{\mathbf{S}}$ would be larger than either of the northern hemispheric locations.

While a qualitative estimate of event magnitude is useful for general observations, a quantitative metric is necessary to compare to the observed characteristics of LEP events. Bearing in mind the similarities (and dissimilarities) of the investigated paths, it is possible to quantitatively estimate the amplitude change by applying metrics from previous work [*Peter and Inan*, 2007, Figure 12b)] relating the change in electron density to the amplitude of an observed LEP event as discussed in Section 2.1.1. While the integrated line density enhancement (or N_{ILDE}) metric derived in this past work is technically only valid for the exact path for which it was calculated, the linear relationship between ionization and amplitude implies that a similar (linear) relationship should also exist between LEP events observed on similar GCPs (such as $\varphi_1^{\mathbf{N}}$ and $\varphi_2^{\mathbf{N}}$).

The N_{ILDE} metric is a single number which characterizes, for the purpose of estimating ΔA, the total integrated ionization created between the transmitter and the receiver (shown in Figure 4.4a) and between the altitudes of 80 km and 85 km (as shown in Figure 4.4b). Since the location of each precipitation region is unknown, it is necessary to estimate both the size of the disturbance region and the distance from the observed GCP on which it occurred. Estimating the size of the precipitation region from *Peter and Inan* [2007, Figure 8d], the deposition region is assumed to have a Gaussian shape with a standard deviation of $\sigma \simeq 90$ km. It is then assumed that an LEP event is only observed when the center of the deposition region is within one standard deviation of the GCP (i.e., $d_{\mathrm{c}} \leq \sigma$), and also assumed that the distance between the GCP and the disturbance region is uniformly distributed between $[-\sigma, \sigma]$.

The total electron density (ambient plus secondary ionization) profile for each of the three locations is shown in the top row of Figure 4.5 for the Amb 1 ambient profile (used extensively in past work). Note that the differences in the magnitude of electron density change at the different locations is even more noticeable when compared to an ambient density. Using the N_{ILDE} conversion factor to estimate ΔA for the three cases results in a mean amplitude change of 0.57 dB for $\varphi_1^{\mathbf{N}}$, 0.22 dB for $\varphi_2^{\mathbf{N}}$ and 1.5 dB for $\varphi_2^{\mathbf{S}}$.

4.3.3 Onset Duration (t_{d})

The next important feature shown in Figure 4.3 is that it suggests the possibility for determining a longitudinal dependence of the onset duration time for observed LEP events. The onset of an LEP event persists as long as sufficient energy continues to be deposited into the atmosphere and thus depends on the amount of new ionization created during each atmospheric interaction. Below some minimum detectability threshold the newly introduced ionization is sufficiently small so as to constitute a negligible change in the overall electron density. The onset duration is therefore determined by the number of atmospheric interactions of the inter-hemispherically bouncing electron bunch which contribute new ionization at a level large enough to be detected using VLF remote sensing.
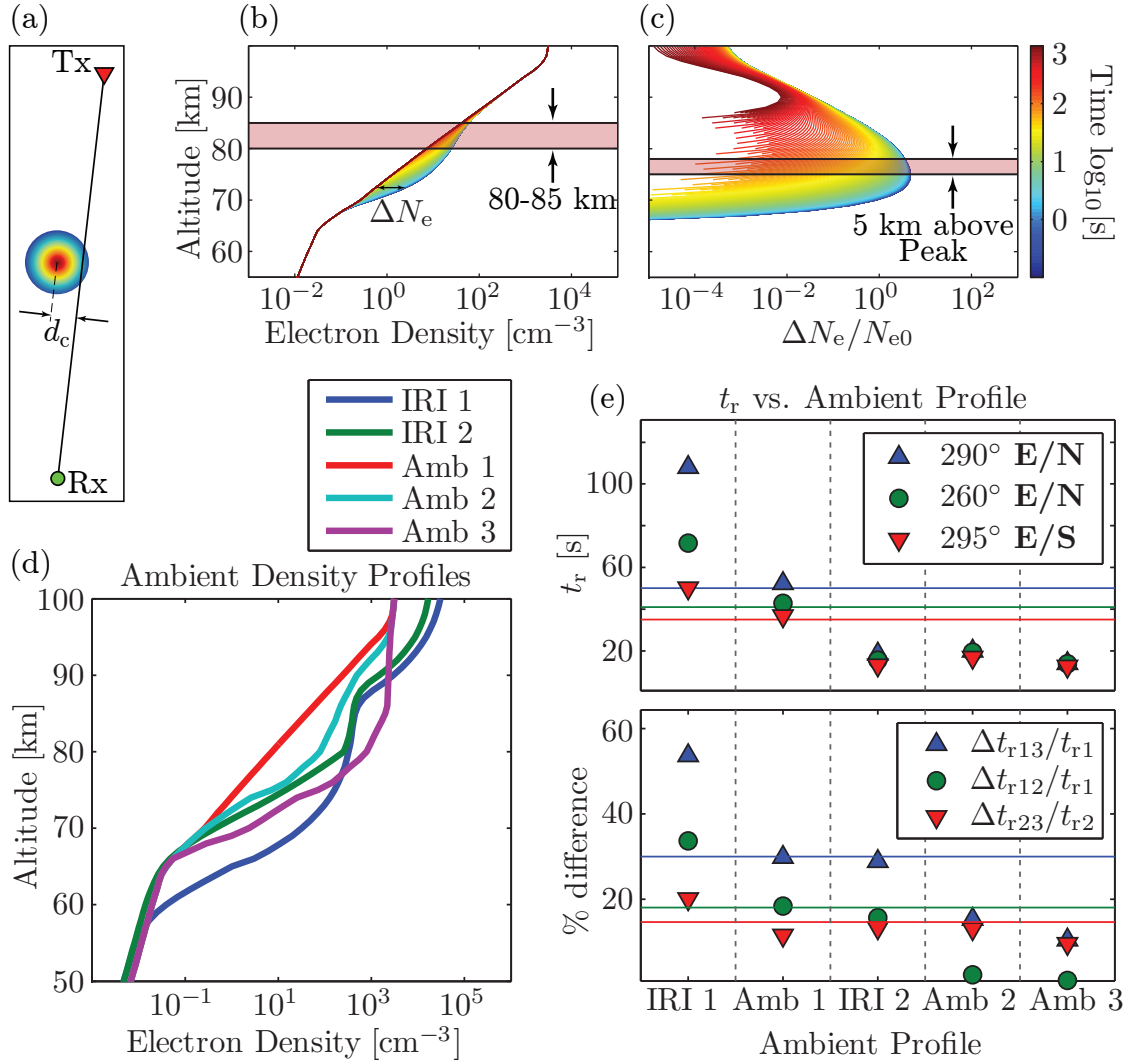
Figure 4.4: Methodology for calculating LEP event amplitude (ΔA) and recovery time (t_r). (a) Example Gaussian precipitation region disturbing a subionospherically propagating VLF transmitter signal. (b) Ambient electron density profile (with deposition) illustrating the altitude dependence of the N_{ILDE} approximation for calculating the amplitude change. (c) Change in electron density relative to the ambient electron density (for the Amb 1 profile), used to calculate the recovery time. (d) Five different ambient profiles used in estimating the recovery time for each longitude. (e) Top panel: recovery time for each of the five ambient profiles (at the altitude of maximum $\Delta N_e/N_{e0}$ to 5 km above this altitude) at each of the three investigated longitudes. Bottom panel: percent difference between the recovery times calculated at each longitude. In both panels the horizontal lines show the mean values recorded in data and discussed in Section 5.1.
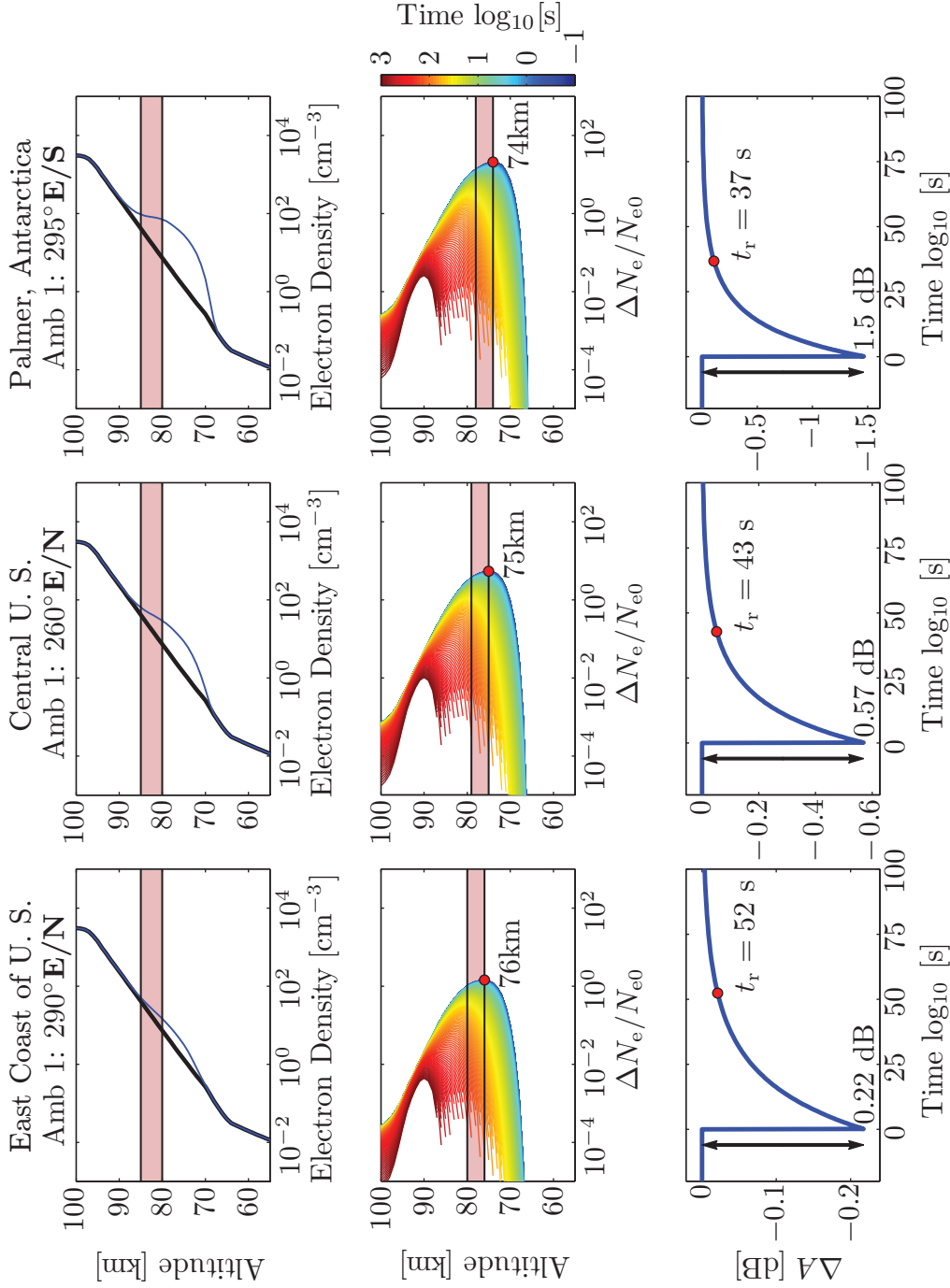
Figure 4.5: Predicted event magnitude and recovery for each of the three locations using the Amb 1 profile. Top Row: total electron density highlighting the altitude range used for calculating ΔA. Middle Row: change in electron density relative to the ambient density, highlighting the altitude range used for calculating t_r. Bottom Row: predicted event shape highlighting the predicted magnitude and recovery time for each of the three locations.

In the specific cases of the calculated deposition profiles at $\varphi_1^{\mathbf{N}}$ and $\varphi_2^{\mathbf{N}}$ (shown in Figure 4.3) the onset duration at each longitude can be inferred by comparing the peak deposition for each of the atmospheric interactions. The secondary ionization created by the first two northern hemispheric depositions (i.e., $\kappa = 3,\ 5$) for both longitudes is on the same order of magnitude as the ambient electron density near the VLF reflection height, and it is therefore likely for these ionospheric disturbances to create perturbations on the VLF signal. Conversely, the peak of the $\kappa=7$ profiles are smaller than the ambient electron density, begging the question as to whether or not they create sufficient ionization to be observed. The deposition peak at $\varphi_1^{\mathbf{N}}$ is more than 40% larger than that at $\varphi_2^{\mathbf{N}}$ so if the minimum detectability threshold lies between these values then the onset duration at $\varphi_1^{\mathbf{N}}$ will be $3\tau_{\mathrm{b}}$ while the onset duration at $\varphi_2^{\mathbf{N}}$ will only be $2\tau_{\mathrm{b}}$. The $\kappa=6$ peak deposition at $\varphi_2^{\mathbf{S}}$ is larger than at either location in the Northern Hemisphere, and while not directly comparable to those two locations (as discussed in Section 4.3.2), it is likely that the corresponding onset duration observed is $\geq 3\tau_{\mathrm{b}}$.

Based upon the bounce period calculation described in Section 3.4.2 for $\varphi_1^{\mathbf{N}}$ and $\varphi_2^{\mathbf{S}}$ the predicted onset duration is $t_{\mathrm{d}}=3\tau_{\mathrm{b}}$, or 0.9–1.3 s depending on the relative contributions of each energy band to the complete distribution. For the $\varphi_2^{\mathbf{N}}$ longitude, the predicted onset duration is $t_{\mathrm{d}}=2\tau_{\mathrm{b}}$ which corresponds to a range of 0.6–0.9 s.

4.3.4 Recovery Time (t_{r})

The last measurable characteristic of LEP events is their recovery time. Like the amplitude change of an LEP event, the recovery time depends significantly on the ambient ionospheric density profile because the recovery of transient ionization is, to first order, determined by the percent change in electron density relative to the ambient electron density profile (i.e. $\Delta N_{\mathrm{e}}/N_{\mathrm{e0}}$) [*Pasko and Inan*, 1994]. In addition, previous work [*Inan et al.*, 1988b; *Glukhov et al.*, 1992; *Pasko and Inan*, 1994] has shown that D-region ionization at lower altitudes recover at a faster rate than ionization at higher D-region altitudes. Based upon this evidence alone, the ABS model can also be used to qualitatively predict the recovery time of LEP events at different

longitudes. To do this, it is necessary to determine the altitude of peak deposition for each geographic location.

The differences seen in the peak altitude of deposition are again due to the asymmetry of the Earth's magnetic field. Recalling from Figure 3.3 that the altitude of deposition is strongly correlated with the energy of precipitating electrons, it is evident that the differences in the altitude profiles for each of the cases are due to the incidence of electrons with a different energy range at each longitude/hemisphere. As previously discussed (at both longitudes in question) the southern hemispheric loss cone is larger, and hence a significant range of electrons are half-trapped above the Northern Hemisphere. This fact, coupled with the previous demonstration that electrons incident at near loss cone angles experience relatively little energy loss and small pitch angle scatterings means, that only the electrons which have lost significant energy have diffused far enough inside the southern loss cone to also be inside the northern hemispheric loss cone. Note again that the half-trapped range of electrons is indicated by the solid horizontal line in each bottom-row panel of Figure 4.2. This feature can be seen graphically by comparing the incident distributions for each of the three cases in Figure 4.2. The range of input electrons for $\varphi_1^{\mathbf{N}}$ can be seen in the top-right panel of Figure 4.2a, the range for $\varphi_2^{\mathbf{N}}$ can be seen in the top-right panel of Figure 4.2b, and the range for $\varphi_2^{\mathbf{S}}$ can be seen can be seen in either of the bottom panels of Figure 4.2b. Note that the bottom panels of Figure 4.2a represent the conjugate point of $\varphi_1^{\mathbf{N}}$ but as there are no transmitter to receiver GCPs in this region it is not possible to compare the predicted results to measurements. In each case, the incident electrons are shown between the pitch angles of 0° and 90°. It is evident by comparing these three plots that not only is the total incident energy different, but the fluence of high energy electrons (i.e., those near 0.3 MeV) is significantly different depending on input location.

Before modeling the recovery time, it is important to note that because the recovery time is so dependent on the percent change relative to the background levels, that the differences (and unknowns) in the ambient electron density profile may introduce significant uncertainty into the recovery time calculations. In an effort to address the variability of ambient electron density, a number of different ambient profiles are

used in recovery calculations. In addition to the three profiles described by *Inan et al.* [1992], two ionospheric profiles from the International Reference Ionosphere (IRI) are used. These five profiles are shown in Figure 4.4d and display the ambient electron density (in cm^{-3}) as a function of altitude.

The recovery of the transient ionization incident upon the atmosphere is calculated using a 5-species model (separated into electrons, positive ions and ion clusters, negative light and heavy ions) of ionospheric chemistry [*Lehtinen and Inan*, 2007], and described in detail in Section 2.1.2. For the current simulations most of the important rate coefficients are taken from *Pasko and Inan* [1994], with the electron detachment rate taken from *Alexandrov et al.* [1997]. An example ionospheric recovery is shown in Figure 4.4c. In this figure the change in ionization relative to the ambient ionosphere ($\Delta N_e / N_{e0}$) is shown as a function of altitude and the corresponding time is indicated by the color of the line (shown by the color bar on a log scale with t=0 s corresponding to dark blue and t=1000 s corresponding to dark red). Note that as expected [e.g., *Pasko and Inan*, 1994; *Lehtinen and Inan*, 2007], the recovery of ionization is a strong function of altitude, with higher D-region altitudes ($\sim$90 km) generally recovering more slowly than lower D-region altitudes ($\sim$80 km).

The middle row of Figure 4.5 shows the peak relative change in electron density (i.e., $\Delta N_e / N_{e0}$) at each of the three locations. At $\varphi_1^{\mathbf{N}}$ this peak change in electron density occurs at 76 km, at $\varphi_2^{\mathbf{N}}$ the peak relative change in electron density occurs at 75 km, and at $\varphi_2^{\mathbf{S}}$ the peak relative change occurs at 74 km. Though these differences in altitude may seem relatively small, it is important to note that the attachment and detachment coefficients of electrons (critical factors for determining the chemical relaxation of the atmosphere) vary exponentially with altitude [e.g., *Pasko and Inan*, 1994], so that even small differences in the altitude profile can have a relatively large influence on the recovery of the LEP event. In addition, because the chemical relaxation of the atmosphere is not dependent on GCP configuration (in contrast to the amplitude change), the recovery time for each of the three locations can all be reasonably compared. For the cases presented, the ABS model predicts the fastest recovery for LEP events observed at $\varphi_2^{\mathbf{S}}$, the slowest recovery at $\varphi_2^{\mathbf{N}}$, and an intermediate value at $\varphi_1^{\mathbf{N}}$.

Using the first-order approximation of the recovery time, $t_r \sim \Delta N_e/N_{e0}$ (between the altitudes where $\Delta N_e/N_{e0}$ is maximum to 5 km above this altitude), to estimate the recovery time for each of the three cases yields results consistent with the qualitative predictions above. As shown in the top panel of Figure 4.4e, for every ambient profile the predicted recovery times for $\varphi_1^{\mathbf{N}}$ (ranging from 14 s to 72 s) are consistently shorter than the predicted recovery times for $\varphi_2^{\mathbf{N}}$ (ranging from 14 s to 108 s), and consistently longer than the predicted recovery times for $\varphi_2^{\mathbf{S}}$ (ranging from 13 s to 50 s).

It is clear that due to differences in initial values of $\Delta N_e/N_{e0}$, the variation of recovery time among different ambient profiles (N_{e0}) is significantly larger than the recovery time variation of the different deposition profiles (ΔN_e). It is therefore important to compare recovery times for the same ambient profile, and not to compare recovery times among profiles. It is also useful to compare the relative differences among the recovery times (for each separate ambient electron density profile). For the five ambient electron density profiles investigated, the recovery at $\varphi_2^{\mathbf{N}}$ is an average of 28% longer than at $\varphi_2^{\mathbf{S}}$, and 14% longer than at $\varphi_1^{\mathbf{N}}$, while the recovery at $\varphi_1^{\mathbf{N}}$ is an average of 13% longer than at $\varphi_2^{\mathbf{S}}$. This data is shown graphically for the five profiles in the bottom panel of Figure 4.4e, where despite the variation, the relative length of recovery time is consistently shorter for deposition which occurs at lower altitudes.

Finally as a single number with which to compare to data, it is interesting to note that for the Amb 1 profile shown in Figure 4.4d (and used extensively in past work as Profile 1 [e.g., *Inan et al.*, 1992; *Pasko and Inan*, 1994; *Peter and Inan*, 2007]), the calculated recovery times for the three longitudes are 52 s, 43 s, and 37 s for $\varphi_2^{\mathbf{N}}$, $\varphi_1^{\mathbf{N}}$, and $\varphi_2^{\mathbf{S}}$, respectively. Also shown for reference in Figure 4.5 is the total event magnitude, recovery curvature and recovery time for each of the three locations.

Chapter 5

Comparison of Model and Observations

5.1 Ground-based Observations of VLF Transmitter Signals

The previous chapter laid out the methodology for calculating LEP event characteristics and predicted results at three separate longitudes/hemispheres. It is now possible to compare the predicted characteristics of LEP events to those observed in data. The challenge in this comparison is that characteristics of LEP events vary widely on an individual basis due to the number of variables which contribute to their creation. For example, the peak current of the lightning flash relates to the amplitude and frequency spectrum of the whistler wave in the magnetosphere [e.g., *Bortnik et al.*, 2006a,b]. The whistler wave amplitude and frequency spectrum in turn affects the number and energy of electrons scattered into the loss cone [*Chang and Inan*, 1983], as does the flux of trapped particles available for scattering [*Peter and Inan*, 2004]. In addition, the magnetospheric cold plasma density can affect the individual ray-paths, thus changing the location of the precipitation footprint on the ionosphere [*Peter and Inan*, 2007]. Finally, the electron density of the ambient ionosphere affects the modal composition of the subionospheric VLF waves [e.g., *Poulsen et al.*, 1993b;

Lehtinen and Inan, 2007], which can affect the amount of scattering observed from any disturbance region on a subionospheric VLF signal for a given GCP.

With all of these variables affecting the characteristics of LEP events, the most tractable way to separate the longitudinal dependence from the variation among individual events is with a statistical analysis of event characteristics. To create this statistical database it is necessary to examine LEP events from transmitter to receiver GCPs which are as close to north-south as possible to limit the measured longitudinal extent. As discussed in Section 2.3.2 and shown in Figure 2.4, the paths chosen for this study are at geographic longitudes (φ) of 260° **E/N**, 290° **E/N** and at 295° **E/S**. The selected data sets came from a cursory search of several years of data to identify time periods (at each location) in which a large number of LEP events occurred. The spring (April and May) and autumn months (September and October) from the years of 2005, 2006 and 2008 provided the best data for this study. Each data set was then analyzed in detail, with every LEP event large enough to be observed above the noise floor counted for the statistics with a standard set of criteria used to characterize the events.

The definitions of LEP event characteristics laid out in Section 2.1 are repeated briefly here for convenience. The LEP event amplitude (ΔA) is calculated as the total deviation (in dB) in the signal amplitude of the recorded VLF signal. The onset duration (t_{d}) is defined as the time over which the amplitude change occurs (taken to be from from the 10% to 90% amplitude change). The recovery time is defined as the time between the end of the onset of the event (time of maximal deviation from ambient conditions) to when the signal amplitude returns to a value within 10% of the initial (unperturbed) value that it would have had in the absence of the event. Finally, the onset delay (Δt) is defined as the time between the causative lightning flash to when the onset of the event begins (the 10% change point). The time of the lightning flash was determined by identifying the causative sferic (signature of a lightning strike in the frequency band of the VLF transmitter signal and observed in the same VLF data [*Inan et al.*, 1996, and references therein]).

Due to varying signal-to-noise ratios (SNR) throughout the observation periods and between different observation sites, some parameters were not always discernible.

While the amplitude change and onset duration time are (nearly) always well defined and easily identifiable, the recovery time and specifically the onset delay are sometimes obscured. Identification of the onset delay can often be very difficult, primarily due to the large occurrence rate of lightning relative to the number of LEP events. On some occasions there are several possible causative lightning flashes identified in the data and in still others the SNR is low enough that it is impossible to identify any causative lightning flash. In the cases where no lightning flash could be identified the event was removed from the statistics entirely because the causative mechanism could not conclusively be attributed to lightning. In the cases where it is clear that the perturbation of the VLF signal is caused by lightning, but there are multiple possible causative flashes, then the onset delay is considered unknown but the other characteristics of the event are recorded. The measurements of recovery time are also treated in this manner. Typically lasting many tens of seconds, the recovery time can be interrupted on occasion by the natural variation of the ionosphere or by a subsequent LEP event (or other sudden ionospheric disturbance). In these cases (since the classification of the event is not based upon the recovery time), the recovery time is listed as unknown, but the other characteristics are recorded.

These complications are reflected in the number of events (n) included in the statistical analysis as shown in Figure 5.1 (a), (b), and (c). As can be surmised by the number of events with some unidentified characteristics, the NPM signal received at Palmer ($\varphi_2^{\mathbf{S}}$) had an excellent SNR and all characteristics could be identified for each event. The paths from the NML transmitter to the HAIL Array ($\varphi_1^{\mathbf{N}}$) and those comprising the paths off the East Coast of the U. S. ($\varphi_2^{\mathbf{N}}$) had a lower SNR resulting in greater difficulty identifying all event characteristics. In addition, the large number of lightning flashes in the vicinity of these two regions further complicated the identification of the causative sferic.

The results of the statistical data analysis are summarized in Figure 5.1 and though there is an obvious spread in each of the observed characteristics (due to factors described above) it is useful to look at the mean value of each characteristic at each location. Each panel's legend displays the mean and standard deviation for the plotted histogram. Taking this mean value to represent a 'typical' LEP event
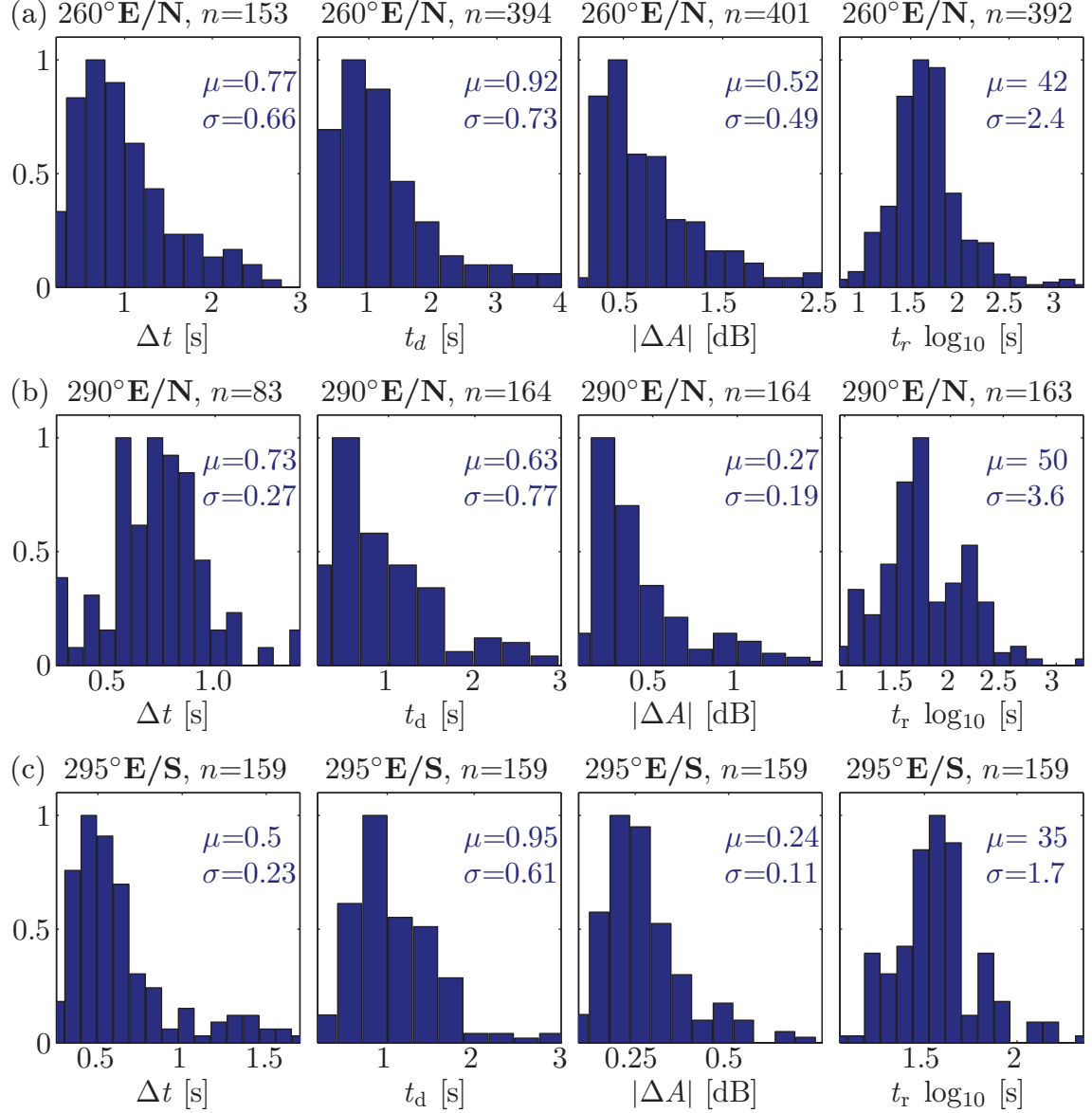
Figure 5.1: Statistically identified characteristics of LEP events at different longitudes. Each panel above is a histogram (with peak normalized to unity) for each of the four LEP characteristics: onset delay (Δt), onset duration (t_d), amplitude ($|\Delta A|$), and recovery time (t_r). (a) Characteristics of LEP events observed at $\varphi_1^{\mathbf{N}}$=260° $\mathbf{E/N}$. (b) Characteristics of LEP events observed at $\varphi_2^{\mathbf{N}}$=290° $\mathbf{E/N}$. (c) Characteristics of LEP events observed at $\varphi_2^{\mathbf{S}}$=295° $\mathbf{E/S}$.

at the specified location, it is clear that the prediction of a longitudinal variation is borne out in the data and that it is now possible to evaluate the ABS model results discussed in Section 4.3. Table 5.1 shows the comparison between the modeled LEP characteristics and those observed in the data. The table is divided up into the predictions which come directly from the ABS model (onset delay and onset duration) and the predictions which require further modeling and unknowns (amplitude change and recovery time).

The amplitude predictions match the measurements very well with the exception of the predicted amplitude change for the southern hemispheric path (i.e., $\varphi_2^{\mathbf{S}}$). Even expecting the linearity of the Integrated Line Density Enhancement approximation [*Peter and Inan*, 2007] to fail when extended to such a long path, it is still surprising that the mean amplitude change of events at $\varphi_2^{\mathbf{S}}$ is smaller than at either $\varphi_1^{\mathbf{N}}$ or $\varphi_2^{\mathbf{N}}$. One possible explanation for this discrepancy is that on such a long over-sea path there is likely only a single dominant subionospherically propagating mode [*Inan and Carpenter*, 1987]. The presence of only a single mode can contribute to generally smaller signal perturbations in a couple of ways. Since there is only a single mode, it may be that the disturbance region does not have significant ionization in the altitude range where the electric field of the mode is large, resulting in a small scattering [e.g., *Lehtinen and Inan*, 2007]. In addition, as shown by *Marshall* [2009, Figure 4.5], the presence of interference nulls in the ground amplitude of subionospheric wave propagation can contribute to the observation of larger signal perturbations. Since there are no modal interference nulls for only a single subionospherically propagating mode it may be that the signal perturbations due to ionospheric disturbances are generally smaller than on shorter paths. It is useful to note here that VLF phase perturbations associated with LEP events may, in contrast, be much more clearly observable on all-sea-based paths such as that from NPM to Palmer, as was previously noted [*Wolf and Inan*, 1990; *Inan and Carpenter*, 1987]. Phase perturbation events are indeed much more numerous in data sets on this path; however, phase perturbations are not used in the current work since data from other longitudes have many more amplitude events.

The observed mean of all remaining LEP characteristics match the predicted values quite closely. The prediction of recovery time based upon the atmospheric chemistry model match well with the observed results where, in general, the mean recovery time observed at $\varphi_2^{\mathbf{S}}$ is the shortest followed by $\varphi_1^{\mathbf{N}}$, and the longest mean recovery time is observed at $\varphi_2^{\mathbf{N}}$. Additionally, for one ambient electron density profile (Amb 1) used extensively in previous work [e.g., *Pasko and Inan*, 1994; *Peter and Inan*, 2007], the match between observed and predicted recovery is rather exceptional. For $\varphi_1^{\mathbf{N}}$ the mean observed and predicted recovery times are 42 s and 43 s, respectively. For $\varphi_2^{\mathbf{N}}$ the mean observed and predicted recovery times are 52 s and 50 s, respectively and for $\varphi_2^{\mathbf{S}}$ the mean observed and predicted recovery times are 35 s and 37 s, respectively. The recovery calculation is strengthened by noting that even within the wide range of recovery times predicted using different ambient profiles, the relative differences among the recovery times are consistent. These results are summarized in the bottom section of Table 5.1 in which the average percent difference calculated by the recovery model is compared with the average differences observed in data. For all three cases the results are quite similar, giving further confidence in the model results.

The two timing characteristics (onset delay and onset duration) which are most closely tied to the results of the ABS model (i.e., they need no further modeling in contrast to the amplitude change and recovery time) are in good agreement with the mean observed LEP characteristics. The predicted onset delay for all three cases is within 10% of the mean observed onset delay and the predicted onset duration matches well with the lower bound of the predicted range for the onset duration. The fact that the mean observed onset duration is consistently at the lower bound of the predicted results indicates that the higher energy electrons (0.3 MeV) likely play a more important role in determining the onset duration of the LEP event. This can be explained in terms of Figure 3.3 by noting that (for grazing incidence i.e., $\alpha_{200\text{km}} \geq 70°$) while the altitude of peak deposition for precipitating 0.3 MeV electrons is at ∼75 km and the altitude of peak deposition for 0.1 MeV electrons is at ∼85 km, the amount of ionization created by the 0.3 MeV electrons at 85 km is still larger than the peak deposition due to 0.1 MeV electrons. Additionally, the 0.3 MeV electrons create more

than twice the amount of total ionization created by the 0.1 MeV electrons. The result of this is an onset duration which is likely dominated by the 0.3 MeV electrons with a shorter bounce-period.

While the mean observed characteristics match the typical events modeled in Section 4.1, Figure 5.1 shows that for each characteristic there is considerable spread around the mean. This spread is expected due to the large number of variables which contribute to the production of an LEP event. Most of the variation can be easily explained by the variation in the peak current and frequency content of the causative lightning flash. In the case of a strong lightning flash the generated whistler also has a large magnetic field component and likely scatters electrons more effectively into the loss cone. In such a case it is plausible that the scattering is of sufficient magnitude to scatter electrons deep enough into the loss cone that observable levels of precipitation can occur without the necessity of atmospheric backscatter. Likewise, if the scattering is very large, then a larger number of electrons are scattered into the loss cone and the deposition profile for subsequent atmospheric interactions (beyond the κ=6 or 7 scattering for the Southern or Northern Hemisphere respectively) may be above the minimum detectability threshold. In the case of very weak scattering it is possible that the deposition profile only remains above the minimum detectability threshold for one atmospheric interaction. Additionally, differences in the frequency content of the whistler wave can result in variations in the energy of precipitated electrons [e.g., *Lauben et al.*, 2001], which can in turn affect the characteristic magnitude, onset duration and recovery time of observed events. Finally, a long onset delay can be explained by the possibility of lightning at lower latitudes, which can cause precipitation at higher latitudes due to scattering by magnetospherically reflecting whistlers [*Bortnik et al.*, 2006a,b]. In such a case the whistler wave energy reflects several times in the magnetosphere (moving in a poleward direction) before it reaches the latitude of observation, each whistler bounce taking ∼0.8 seconds between equatorial crossings.

Location	Characteristic	Model	Data (μ)
	Δt	0.7 s	0.77 s
	t_{d}	$0.9 - 1.3$ s	0.92 s
$\varphi_1^{\mathbf{N}}$			
	ΔA	0.57 dB	0.52 dB
	t_{r}	43 s*	42 s
	Δt	0.7 s	0.73 s
	t_{d}	$0.6 - 0.9$ s	0.63 s
$\varphi_2^{\mathbf{N}}$			
	ΔA	0.22 dB	0.27 dB
	t_{r}	52 s*	50 s
	Δt	0.55s	0.5 s
	t_{d}	$0.9 - 1.3$ s	0.95 s
$\varphi_2^{\mathbf{S}}$			
	ΔA	1.5 dB	0.24 dB
	t_{r}	37 s*	35 s
$\varphi_2^{\mathbf{N}}$ vs. $\varphi_2^{\mathbf{S}}$	$\Delta t_{\mathrm{r}13}/t_{\mathrm{r}1}$	28%	30%
$\varphi_2^{\mathbf{N}}$ vs. $\varphi_1^{\mathbf{N}}$	$\Delta t_{\mathrm{r}12}/t_{\mathrm{r}1}$	14%	18%
$\varphi_1^{\mathbf{N}}$ vs. $\varphi_2^{\mathbf{S}}$	$\Delta t_{\mathrm{r}23}/t_{\mathrm{r}2}$	13%	15%

Table 5.1: Comparison of model predictions (Section 4.1) and observations (Section 5.1) for the three longitudes considered. The first three sections compare each longitude separately. The last section compares the relative recovery times between the longitudes. *For Amb 1 profile.

5.2 Satellite Observations of Backscattering Electrons

The accuracy and validity of the ABS model can be further evaluated by comparison with in-situ observations of electrons scattered into the bounce loss cone as reported by *Voss et al.* [1984, 1998]. This rare and impressive data set shows the detailed evolution of electrons scattered into the bounce loss cone by lightning, and tracks the backscattered electrons as they bounce between hemispheres. These events were recorded by a number of particle detectors on-board the low-altitude (200 km) S81-1/SEEP satellite. The two detectors most important for comparison with this work are the TE2 and ME1 detectors, oriented at 90° and 0° from zenith, respectively, as shown graphically in Figure 5.2a. The best-defined of the recorded events [*Voss et al.*, 1998, Figure 5b] was recorded at an altitude of 200 km at L=2.23 and a geographic longitude of φ=277° **E/N**. For this case the magnetic field had a magnetic dip angle of ∼65°, meaning that the TE2 detector was oriented to detect precipitating electrons at grazing incidence (high pitch angles of $45° \lesssim \alpha_{200km} \lesssim 85°$), and the ME1 detector was oriented to detect backscattered electrons with pitch angles deep inside the loss cone ($\alpha_{200km} \lesssim 55°$).

To compare to this data set, it is necessary to model the physical conditions under which the observations by *Voss et al.* [1998] were made as closely as possible. This matching is accomplished using the same pitch angle scattering calculation shown in Figure 4.1a but limiting the input distribution of electrons to between 0.1 MeV and 0.2 MeV as shown in *Voss et al.* [1998, Plate 1]. This distribution is then transformed to a 200 km altitude at φ=277° **E/N** for input into the ABS model.

Because the ABS model calculates only the total incident and backscattered fluence from each hemisphere it is necessary to make assumptions as to the shape and duration of the incident pulse. Consistent with previous work [*Lauben et al.*, 1999], the chosen pulse shape is Gaussian with a standard deviation of 0.5 s. To calculate the time of arrival for each pulse on the atmosphere, a mean bounce period τ_b=330 ms (corresponding roughly to the bunching time of a backscattered distribution incident at the intermediate energy of 150 keV) is used. The results of this analysis are shown

(a)

(b)

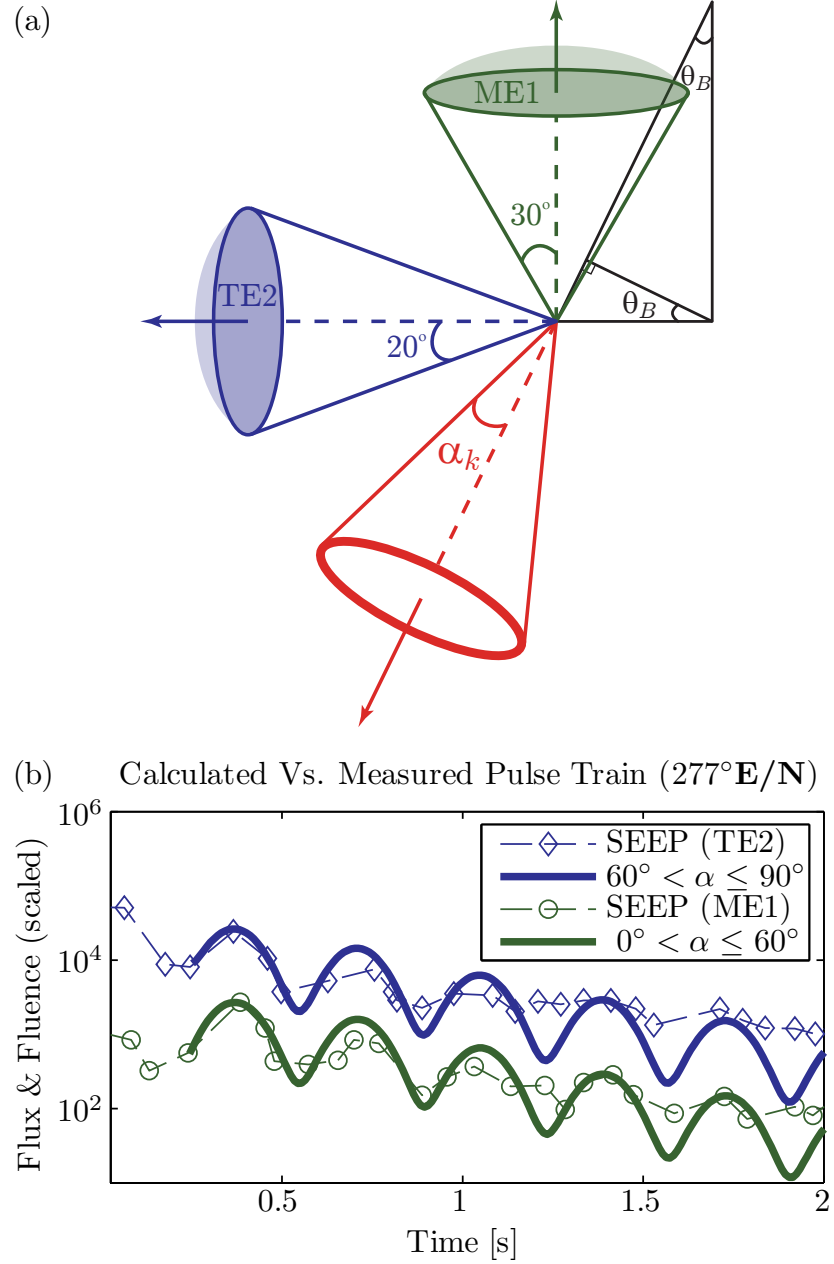**Figure 5.2:** (a) Illustration of the detector setup on-board the SEEP satellite show-ing the TE2 and ME1 detectors, as well as their approximate orientation relative to the magnetic field (θ_B) and precipitating electrons of initial pitch angle α_i. (b) Com-parison of the ABS model and data from the SEEP satellite [*Voss et al.*, 1998, Figure 5b] showing the evolution of backscattered electrons in data.

in Figure 5.2b overlaid upon the original data points from [*Voss et al.*, 1998, Figure 5] for the TE2 and ME1 detectors. Note that the range of pitch angles included in the two curves (grazing incidence and deep incidence) match closely to those detected by the respective detectors. Because the number of precipitating electrons is primarily determined by the lightning peak current and the background density of electrons in the magnetosphere available for scattering, the ABS model results are normalized such that the first backscattered peak (green curve at $\sim$0.4 s) is equal in magnitude to the first backscattered peak observed in data. Figure 5.2b shows excellent agreement between the ABS model and the observed backscatter distribution. In particular the number of electrons observed on the TE2 detector relative to that on the ME1 detector is in excellent agreement (i.e., $\sim$10 times larger) with the predicted ratio. Furthermore the rate of decay predicted for both the TE2 and ME1 detector match well through κ=7 backscatters before the remaining distribution is comparable to the noise floor of the measurements. It is also important to note that this same calculation carried out at other longitudes (e.g., φ=260° $\mathbf{E/N}$, not shown) does not match the data presented by *Voss et al.* [1998] (at φ=277° $\mathbf{E/N}$) in terms of either relative backscatter magnitude, or in decay rates of the two curves.

The excellent agreement between the ABS model and the observed distribution provides further confidence in the accuracy of the ABS model and indicate its usefulness for in-situ as well as ground-based predictions.

Chapter 6

Summary and Future Work

6.1 Summary

This dissertation details a novel method for predicting the characteristics of LEP events at any longitude and mid-latitude L-shell by accounting for the effects of precipitating electrons which are backscattered from the atmosphere. As detailed in Chapter 3, the model of atmospheric backscatter is based upon the calculation of an atmospheric backscatter response for ~16,000 individual monoenergetic electron beams with a single incident pitch angle using the Monte Carlo model detailed in *Lehtinen et al.* [1999]. Treating the backscatter from the atmosphere as a linear system, each of these backscatter responses can be thought of as an atmospheric response to an input pair $(\mathcal{E}_0, \alpha_0)$. In this way, not only can these backscatter responses be used to determine the backscatter of any arbitrary input electron distribution, but looking at the characteristics of the individual atmospheric responses reveals insight into the previously undervalued importance of incident pitch angle on deposited and backscattered electron characteristics.

The next major component of the Atmospheric Backscatter model is the inclusion of Earth's asymmetric magnetic field in calculations of backscattered electron pitch angle entering the conjugate hemisphere. The varying magnetic field strength at conjugate points of the same field line causes an expansion or contraction of the flux tube in the conjugate hemisphere. An electron just inside the local loss cone in

one hemisphere may therefore be either deep inside the loss cone in the conjugate hemisphere or conversely may be so far above the loss cone that it cannot reach the conjugate atmosphere at all. The ABS model accounts for these differences through use of the first adiabatic invariant and by scaling the distribution in each hemisphere (using a factor of $\cos\alpha\cos\theta_B$) to conserve the total horizontal input energy in transferring the electron bunch from one hemisphere to the other. These calculations are critical, especially because the difference between hemispheric loss cones means that for many longitudes (especially near the South Atlantic Anomaly), backscatter from the Southern Hemisphere is the only explanation which can account for LEP events observed in the Northern Hemisphere without exceptionally large equatorial pitch angle scattering (of $\sim4°$), much larger than predicted in the literature [*Chang and Inan*, 1983; *Lauben et al.*, 1999; *Bortnik et al.*, 2006a,b].

The final step for predicting the characteristics of LEP events using the ABS model is to create a realistic distribution of precipitating electrons as input. As detailed in Chapter 4 this is done using the WIPP model of *Bortnik et al.* [2006a,b] which calculates the equatorial pitch angle change for magnetospheric electrons. This scattering is combined with a realistic sinusoidal pitch-angle distribution and scaled by the AE8 MAX trapped flux model to produce the final number density (and pitch angle distribution) of precipitating electrons. This distribution is then converted to the specified longitude and altitude for input into the ABS model.

Using the above methodology to calculate deposition profiles and backscatter distributions, Chapter 5 discusses the comparison between predicted LEP characteristics at three longitudes and those observed in data. The model predictions match data quite well in each case.

Confirming the prediction of *Peter and Inan* [2007], there is a one bounce-period delay in the Northern Hemisphere, and a corresponding one-half bounce period advance in the Southern Hemisphere in the observed onset delay (Δt) at the longitudes investigated which was previously undocumented. The onset duration of LEP events also exhibit a longitudinal and hemispheric variation based upon the number of times an incident distribution of electrons can backscatter and still create atmospheric ionization above a minimum detectability threshold. At the longitudes investigated, the

three bounce-period duration predicted by the ABS model matches well with observations over the Central United States and in the Southern Hemisphere near Antarctica. Likewise, the prediction of a two bounce-period duration for LEP events observed off the East Coast of the United States is also observed in the data.

The longitudinal and hemispheric variation of LEP event amplitude change occurs due to the difference between the northern and southern hemispheric loss cones, $\Delta\alpha_{\mathrm{eq}}^{\mathrm{lc}}$. However, the ABS model provides only atmospheric deposition profiles which must be further modeled using other methods [e.g., *Peter and Inan*, 2007; *Lehtinen et al.*, 2010] to quantify the exact variation in amplitude. A preliminary investigation using the integrated line density enhancement approximation of *Peter and Inan* [2007] yields results which are consistent with observations on paths of similar length and location (in the Northern Hemisphere), but as expected do not match well with the long distance path in the Southern Hemisphere.

The recovery time also requires significant modeling beyond the scope of the ABS model to compare with observed results. However, a first-order approximation of the recovery time using a 5-species model of atmospheric chemistry to calculate the change in electron density relative to the ambient ($\Delta N_{\mathrm{e}}/N_{\mathrm{e0}}$) yields results which are qualitatively consistent over a range of different ambient ionospheric profiles. Furthermore, for the ambient ionosphere Amb 1, used extensively in past work, the quantitative predictions for all three longitudes match exceptionally well with the mean recovery time observed in the data.

The preceding chapters have shown the importance of atmospheric backscatter in determining the characteristics of LEP events. By accounting for atmospheric backscatter it is possible to accurately predict all the observable characteristics of LEP events. Furthermore, by combining the effects of atmospheric backscatter with previously calculated radiation belt electron loss rates due to lightning at a single longitude [*Peter and Inan*, 2007] it is possible to develop a global estimation of radiation belt electron loss due to lightning. Finally, by accounting for the asymmetry of the Earth's magnetic field in backscatter calculations it is possible to link the total electron precipitation at conjugate points of the same field line and to estimate radiation belt electron loss rates due to lightning even in remote portions of the world

where there are few VLF receivers and even fewer VLF transmitters (e.g., over much of Africa).

6.2 Suggestions for Future Work

Over the previous decade the Stanford VLF group has made tremendous advances in understanding the removal of energetic electrons from the radiation belts by lightning. Building on these contributions, this dissertation serves as one of the final pieces necessary in formulating a global estimate of radiation belt electron loss due to lightning. It is to this end that much of the suggestions for future work is geared.

Working together at Stanford University as graduate students, Dave Lauben and Mike Johnson determined for the first time that obliquely propagating whistlers dominate the observation of LEP events and that a single lightning flash can precipitate electrons over thousands of square kilometers of the atmosphere [*Johnson et al.*, 1999; *Lauben et al.*, 2001]. Building upon this work, Bill Peter determined the spatial displacement of LEP from a causative lightning discharge [*Peter and Inan*, 2004] and using theoretical models developed (during their Ph.D. studies at Stanford) by Mike Chevalier, Jacob Bortnik, and Nikolai Lehtinen [*Chevalier et al.*, 2007; *Bortnik et al.*, 2006a,b; *Lehtinen et al.*, 1999], formulated a comprehensive methodology for relating the number and energy of precipitating electrons to the observed amplitude and phase of two characteristic LEP events in the Central United States [*Peter and Inan*, 2007].

Motivation for the current dissertation came out of this work when the predicted amplitude change matched observations exceptionally well, but the onset delay was consistently observed to be significantly longer than model predictions. The ABS model addressed this discrepancy but in doing so also shed light on the fact that the characteristics of LEP events (and hence the likely role of lightning in the removal of radiation belt electrons) show a strong longitudinal and hemispheric dependence.

A global measure of the effect of lightning on radiation belt electron loss therefore needs to incorporate the effects of the asymmetric geomagnetic field and account for the discovery that conjugate observations are directly linked by the backscattering process.

6.2.1 Global Extension of the ABS Model

The first study which needs to be undertaken is assessment of the global applicability of the results described in this dissertation. To do so it is necessary to evaluate the predictions at other longitudes and under the varying effects of the asymmetric geomagnetic field. As can be seen from Figure 6.1, both of the locations investigated in the current dissertation lie in the portion of the globe where (i) the southern hemispheric loss cone is larger and (ii) the drift loss cone is narrowing, meaning that there are eastward-drifting electrons continuously filling the near-loss cone portion of the radiation belts.

In order to finally quantify the global contribution of LEP to radiation belt electron loss it is therefore necessary to compile statistical measurements of LEP event characteristics at a number of different locations, characterized by their geographic longitude (φ) in the $L = 2$–3 interval. First, φ_{f_1} has the same value of $\Delta\alpha_{eq}^{lc} = \alpha_{eq,\mathbf{S}}^{lc} - \alpha_{eq,\mathbf{N}}^{lc}$ as φ_2 so based only upon the atmospheric backscatter model, LEP event characteristics should be very similar. However, φ_{1_f} is located where the drift-loss cone is expanding and therefore the continuous filling of the near-loss cone portion of the radiation belts is absent. Quantifying the effect this gradient in $\Delta\alpha_{eq}^{lc}$ has on LEP event characteristics is necessary.

Second, the locations φ_{f_2} and φ_{f_3} are at the respective global maximum and minimum of $\Delta\alpha_{eq}^{lc}$ and assessing LEP event characteristics at these two longitudes provides a bound on the maximum effects of backscatter on LEP events for each extreme case. Finally, locations φ_{f_4} and φ_{f_5} are also important because they lie at the longitudes where $\Delta\alpha_{eq}^{lc} = 0$. Both locations are important because φ_{f_4} represents a transition from a Southern-to-Northern Hemisphere dominated loss cone while φ_{f_5} represents the opposite transition. Observations in both hemispheres at these locations should be similar because the loss cones are so close together, but it is necessary to quantify the effects of Southern-to-Northern dominated loss cone compared to a Northern-to-Southern dominated loss cone in order to quantitatively assess the global role of lightning in radiation belt electron loss.
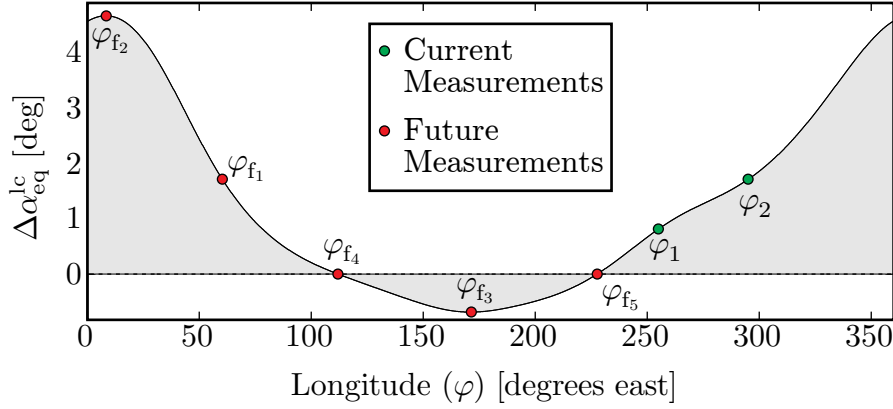
Figure 6.1: Suggested future observation sites based upon the varying equatorial loss cone. Current observation sites are shown at: φ_1, and φ_2 while suggested future sites are shown at: φ_{f_1}, φ_{f_2}, φ_{f_3}, φ_{f_4} and φ_{f_5}. $L = 2.5$.

6.2.2 Model Improvements

As discussed in Chapter 3 the primary sources of error in the ABS model are due to differences in the backscatter population of different magnetic dip angles and the interpolation between results not specifically simulated by the Monte Carlo model. Though these errors are $\leq 10\%$ it is possible to improve the results of the ABS model by simulating inputs at more energies and also at a wider range of intermediate magnetic dip angles.

A more important improvement to the ABS model is to specifically incorporate time into the backscatter simulation so that it is not necessary to assume a temporal profile for the precipitation. This inclusion can be accomplished within the current ABS framework by incorporating a third dimensional 'time bin' into each of the $\mathcal{E}$–α bins. The evolution of each $\mathcal{E}$–α bin would then be temporally independent from the others and the backscatter distribution and deposition profiles could be calculated specifically as a function of time. The improvement using this methodology would, however, come at the cost of significantly increased computational requirements. Using Figure 3.15 as a baseline with which to compare, it is clear that to maintain good temporal accuracy within the ABS model requires sufficient time sampling for electrons with bounce periods of 300–500 ms. Above and below this regime there is a

limited contribution to the overall backscatter and deposition and it may be possible
to limit the required temporal sampling to this range. Relatively coarse temporal
sampling (e.g., 20 ms bins) would result in computational requirements increasing
by approximately one order of magnitude while better temporal sampling (e.g., 5 ms
bins) would require substantially more (up to two orders of magnitude or more).

In addition to improvements to the ABS model itself it is also necessary to im-
prove the accuracy of the predicted event magnitude and recovery time. While the
methodology herein gives a good first-order approximation of both parameters it is
possible for significant improvements to be made in both cases. As shown in Fig-
ure 4.4 and discussed in Sections 2.2 and 4.3 the ambient electron density profile can
significantly affect the amplitude of an observed LEP event and is the dominant factor
in determining the recovery time. In order to address these problems it is necessary
to determine the ambient electron density profile along the perturbed GCP.

Two methods have been proposed to answer this question. The first relies on the
deployment of many receivers along the GCP to isolate the modal structure of the
subionospherically propagating VLF signal to calculate the ambient electron density
profile [*Bainbridge and Inan*, 2003]. The second is based upon knowing the location
of lightning flashes and taking advantage of their consistent source characteristics to
determine the ambient density profile [*Cummer et al.*, 1998]. It is impractical to de-
ploy sufficient receivers in every location to decompose the transmitter propagating
modes; however, a new global lightning detection network based upon the work of
Said et al. [2010] will eventually provide the necessary lightning location for consis-
tently determining the ambient electron density profile. Once the ambient electron
density profile is known it is possible to follow the methodology of *Peter and Inan*
[2007] combined with the ionospheric chemistry model of *Lehtinen and Inan* [2007]
to determine the magnitude and recovery time of LEP events.

6.2.3 Diffusion of Radiation Belt Electrons

In addition to its direct application to studying LEP events the ABS model may
additionally be used to quantify the role of atmospheric backscatter (or atmospheric

Coulomb scattering) in filling the near loss cone population of radiation belt electrons. Investigating a diffusion coefficient which describes this filling process can be undertaken by simulating the evolution of a monoenergetic beam of electrons which is initially incident upon the atmosphere at a pitch angle far outside the loss cone (e.g., $\alpha_{200\mathrm{km}}=90°$). As discussed briefly in Section 3.3.1 the ABS model predicts that such a beam of electrons loses only 0.0011% of the total incident energy. However this energy loss also corresponds to a finite change (or diffusion) in pitch angle. Recognizing that this same bunch of electrons is incident many hundreds of times upon the atmosphere the slow but steady rate of diffusion into the loss cone may become evident. Additionally, due to the asymmetry of the geomagnetic field there may be a longitudinal dependence to this diffusion coefficient. At locations where $\Delta\alpha_{\mathrm{eq}}^{\mathrm{lc}}$ is very small the diffusion rate may be higher and likewise in regions where $\Delta\alpha_{\mathrm{eq}}^{\mathrm{lc}}$ is very large the diffusion rate may be lower. Such predictions could then be used to compare to or even to improve past work in which the contribution of magnetospheric plasma waves was applied to assess the loss of radiation belt electrons on a global scale [*Abel and Thorne*, 1998a,b].

Appendix A

Interpolating Techniques

A.1   Interpolation Between $\Psi_0(\mathcal{E}_0,\,\alpha_0|\mathcal{E},\alpha)$ Pairs

As discussed at the beginning of Chapter 3, the complete set of specifically calculated backscatter distributions is represented by $\Psi_{\mathbf{M}}(\mathcal{E}_0,\,\alpha_0|\,\mathcal{E},\alpha)$. Interpolating between these distributions is the key for applying the ABS model to any arbitrary distribution of precipitating electrons and Section 3.4.3 discusses the differences between two interpolation methods. One interpolation is carried out with the backscatter distribution, $\Psi^{\mathrm{norm}}(\mathcal{E}_0,\,\alpha_0|x,\alpha)$, evaluated on a normalized energy grid using the dimensionless parameter $x = \mathcal{E}/\mathcal{E}_0 \in [0,1]$, and one in which the interpolation is carried out with $\Psi_0(\mathcal{E}_0,\,\alpha_0|\mathcal{E},\alpha)$ evaluated on an absolute (keV) energy grid $\mathcal{E}$ (0–$\mathcal{E}_0$). This Appendix shows how calculation of the two methods differ mathematically.

   The interpolation of a new distribution is designated $\Psi(\mathcal{E}_0',\,\alpha_0'|\mathcal{E},\alpha)$ where $\mathcal{E}_0'$ and α_0' are the respective energy and pitch angle of the interpolated distribution and (as before) the distribution is evaluated on the energy and pitch angle grid $(\mathcal{E},\alpha)$.

   In practice, $\mathcal{E}_0'$ is between the $\mathcal{E}_i$ and $\mathcal{E}_{i+1}$ energies of $\Psi_{\mathbf{M}}(\mathcal{E}_0,\,\alpha_0|\,\mathcal{E},\alpha)$ and the interpolation of $\Psi(\mathcal{E}_0',\,\alpha_0'|\mathcal{E},\alpha)$ is calculated using the surrounding tabulated distributions $\Psi_0(\mathcal{E}_i,\,\alpha_j|\mathcal{E},\alpha)$ and $\Psi_0(\mathcal{E}_{i+1},\,\alpha_j|\mathcal{E},\alpha)$. The differences between the two interpolation methods deal with the grid, $(\mathcal{E},\alpha)$, upon which the surrounding distributions are evaluated. One method is to interpolate based on surrounding distributions evaluated on an absolute energy grid: $\Psi_0(\mathcal{E}_i,\,\alpha_j|\mathcal{E}_i,\alpha_j)$ and $\Psi_0(\mathcal{E}_{i+1},\,\alpha_j|\mathcal{E}_{i+1},\alpha_j)$. The

other method is to interpolate using a normalized energy grid $\mathcal{E}/\mathcal{E}_0$, which requires the definition of an auxiliary function:

$$\Psi^{\mathrm{norm}}(\mathcal{E}_0,\ \alpha_0|\mathcal{E}/\mathcal{E}_0, \alpha) \equiv \Psi(\mathcal{E}_0',\ \alpha_0'|\mathcal{E}, \alpha) \tag{A.1}$$

which contains the same information as $\Psi(\mathcal{E}_0',\ \alpha_0'|\mathcal{E}, \alpha)$, but is a function of a different variable (normalized energy). The surrounding functions are then specified $\Psi^{\mathrm{norm}}(\mathcal{E}_i,\ \alpha_j|\mathcal{E}/\mathcal{E}_i, \alpha_j)$ and $\Psi^{\mathrm{norm}}(\mathcal{E}_{i+1},\ \alpha_j|\mathcal{E}/\mathcal{E}_{i+1}, \alpha_j)$.

Interpolation using an absolute energy grid is represented as

$$\Psi(\mathcal{E}_0',\ \alpha_0'|\mathcal{E}, \alpha) = \mathrm{INTERP}\left\{[\mathcal{E}_0,\ \alpha_0], \Psi_0(\mathcal{E}_0,\ \alpha_0|\mathcal{E}, \alpha)\,, [\mathcal{E}_0', \alpha_0']\right\}, \tag{A.2}$$

where $[\mathcal{E}_0',\alpha_0']$ specifies the energy and pitch angle of the desired distribution, $[\mathcal{E}_0,\ \alpha_0]$ represents the closest input to this desired input and $\Psi_0(\mathcal{E}_0,\ \alpha_0|\mathcal{E}, \alpha)$ represents the set of calculated distributions evaluated on an absolute energy grid (i.e., 0–$\mathcal{E}_0$). Additionally, as can be seen from $\Psi(\mathcal{E}_0',\ \alpha_0'|\mathcal{E}, \alpha)$, the resultant distribution is evaluated on the same grid, $(\mathcal{E}, \alpha)$, as the calculated profiles of $\Psi_0(\mathcal{E}_0,\ \alpha_0|\mathcal{E}, \alpha)$.

The same distribution can be interpolated using a normalized energy scale from 0–1. This normalized energy scale is equivalent (for a single distribution) to $\mathcal{E}/\mathcal{E}_0$ and is represented below by $x = \mathcal{E}/\mathcal{E}_0'$. Using the normalized energy grid the interpolation calculation is written using the auxiliary function as

$$\Psi^{\mathrm{norm}}(\mathcal{E}_0',\ \alpha_0'|x, \alpha) = \mathrm{INTERP}\left\{[\mathcal{E}_0,\ \alpha_0], \Psi^{\mathrm{norm}}(\mathcal{E}_0,\ \alpha_0|x, \alpha), [\mathcal{E}_0', \alpha_0']\right\}, \qquad x \in [0, 1] \tag{A.3}$$

where $[\mathcal{E}_0',\alpha_0']$ and $[\mathcal{E}_0,\ \alpha_0]$ are defined as above and $\Psi^{\mathrm{norm}}(\mathcal{E}_0,\ \alpha_0|x, \alpha)$ represents the surrounding distributions evaluated on a normalized energy grid (i.e., 0–1). Writing Equation (A.3) in terms of Ψ_0 instead of Ψ^{norm} is equivalent to:

$$\Psi(\mathcal{E}_0',\ \alpha_0'|\mathcal{E}, \alpha) = \mathrm{INTERP}\left\{[\mathcal{E}_0, \alpha_0], \Psi_0(\mathcal{E}_0,\ \alpha_0|\mathcal{E}\mathcal{E}_0/\mathcal{E}_0', \alpha_0'), [\mathcal{E}_0', \alpha_0']\right\}. \tag{A.4}$$

A.2 Interpolation Using a Cumulative Distribution Function $\Gamma(\mathcal{E}, \Omega)$

In the case where several $\Psi_0(\mathcal{E}_0, \alpha_0 | \mathcal{E}, \alpha)$ distributions need to be combined into a single distribution (as is the case for the backscatter of an arbitrary incident distribution of electrons), it is necessary to interpolate each distribution onto the same grid. This is accomplished much the same as the interpolation in Equation (A.2) where the input grid must be in terms of absolute energy and the output energy grid must be specified as the largest energy, designated $\mathcal{E}_{\max}$. Using this notation, the interpolation calculation is represented by

$$\Psi_0(\mathcal{E}_0, \alpha_0 | \mathcal{E}_{\max}, \alpha) = \text{INTERP} \left\{ [\mathcal{E}_0, \alpha_0], \Psi_0(\mathcal{E}_0, \alpha_0 | \mathcal{E}, \alpha), [\mathcal{E}_{\max}, \alpha] \right\}. \tag{A.5}$$

The challenge is that the grid $(0\text{–}\mathcal{E}_{\max})$ is sampled more coarsely (i.e., a down-sampled grid) in the area of interest, $0\text{–}\mathcal{E}_0$, where $\mathcal{E}_0 \leq \mathcal{E}_{\max}$. This means that in a strict linear interpolation the interpolated value will be correct, but the bin size will be altered and can lead to errors in the conservation of energy between the two distributions: $\Psi_0(\mathcal{E}_0, \alpha_0 | \mathcal{E}, \alpha)$, and $\Psi_0(\mathcal{E}_0, \alpha_0 | \mathcal{E}_{\max}, \alpha)$. This problem is addressed by interpolating the cumulative distribution function (CDF) of the backscatter distribution.

The CDF of two variables $(\mathcal{E}, \Omega)$, i.e., the backscattered energy and solid angle is defined as

$$\Gamma(\mathcal{E}, \Omega) = \int_{\mathcal{E}_{\min}}^{\mathcal{E}} \int_{\Omega_{\min}}^{\Omega} \Psi_0(\mathcal{E}_0, \Omega_0 | \mathcal{E}', \Omega') \, d\Omega' \, d\mathcal{E}', \tag{A.6}$$

and the corresponding Ψ_0 can be found from

$$\Psi_0(\mathcal{E}_0, \Omega_0 | \mathcal{E}, \Omega) = \left. \frac{\partial^2 \Gamma}{\partial \mathcal{E} \, \partial \Omega} \right|_{\mathcal{E}, \Omega} \tag{A.7}$$

The CDF of the backscatter distribution can therefore be used to perform the interpolation calculation in Equation (A.5) because it can represent the average value

of Ψ_0 on a small enclosing interval $\mathcal{E} \in [\mathcal{E}_1, \mathcal{E}_2]$, $\Omega \in [\Omega_1, \Omega_2]$:

$$\Psi_0(\mathcal{E}_0, \Omega_0 | \mathcal{E}, \Omega) \approx \frac{1}{\Delta\mathcal{E} \, \Delta\Omega} \int_{\mathcal{E}_1}^{\mathcal{E}_2} \int_{\Omega_1}^{\Omega_2} \Psi_0(\mathcal{E}_0, \Omega_0 | \mathcal{E}', \Omega') \, d\mathcal{E}' \, d\Omega' \qquad (A.8)$$

where $\Delta\mathcal{E} = \mathcal{E}_2 - \mathcal{E}_1$, and $\Delta\Omega = \Omega_2 - \Omega_1$. Using $\Gamma(\mathcal{E}, \Omega)$, the last equation is equivalent to

$$\Psi_0(\mathcal{E}_0, \Omega_0 | \mathcal{E}, \Omega) \approx \frac{1}{\Delta\mathcal{E} \, \Delta\Omega} \left[\Gamma(\mathcal{E}_1, \Omega_1) + \Gamma(\mathcal{E}_2, \Omega_2) - \Gamma(\mathcal{E}_1, \Omega_2) - \Gamma(\mathcal{E}_2, \Omega_1) \right]. \qquad (A.9)$$

The actual implementation of Equation (A.5) is therefore best accomplished by first calculating the CDF of $\Psi_0(\mathcal{E}_0, \alpha_0 | \mathcal{E}, \alpha)$, as described by Equation (A.6), interpolating $\Gamma(\mathcal{E}, \Omega)$ onto the down-sampled energy grid $[\mathcal{E}_{\max}, \Omega]$:

$$\Gamma(\mathcal{E}_0, \Omega_0 | \mathcal{E}_{\max}, \Omega) = \text{INTERP} \left\{ [\mathcal{E}_0, \Omega_0], \Gamma(\mathcal{E}_0, \Omega_0 | \mathcal{E}, \Omega), [\mathcal{E}_{\max}, \Omega] \right\}. \qquad (A.10)$$

and calculating the new distribution Ψ_0 from the new Γ using Equation (A.9). The resulting 'downsample-interpolation' is denoted

$$\Psi_0(\mathcal{E}_0, \Omega_0 | \mathcal{E}_{\max}, \Omega) = \text{INTERP}_{DS} \left\{ [\mathcal{E}_0, \Omega_0], \Psi_0(\mathcal{E}_0, \Omega_0 | \mathcal{E}, \Omega), [\mathcal{E}_{\max}, \Omega] \right\}. \qquad (A.11)$$

Appendix B

Combining Backscatter Distributions

B.1 Example Backscatter Calculation

Appendix A explained the methodology for interpolating between specifically calculated Monte Carlo backscatter distributions as well as the best method for interpolating profiles of different energies onto the same (coarser) energy grid. Figure B.1 demonstrates graphically the process involved in calculating $\Psi(\mathcal{E}, \alpha)$ for a simple example distribution of precipitating electrons. This specific example contains the backscatter distribution for three separate incident distributions $(\mathcal{E}_0, \alpha_0)$: $(\mathcal{E}_0=0.1\,\mathrm{MeV}, \alpha_0=70°)$, $(\mathcal{E}_0=0.2\,\mathrm{MeV}, \alpha_0=70°)$, and $(\mathcal{E}_0=0.3\,\mathrm{MeV}, \alpha_0=70°)$.

It is important to understand the process of combining the backscatter distributions for an arbitrary input because it is a key component necessary for calculating the backscatter from a realistic distribution of incident electrons due to LEP (as discussed in Chapter 4). Mathematically, it can be expressed by interpreting Ψ_0 as the Green's function applied to the initial distribution of particles $\Psi_{\mathrm{incident}}(\mathcal{E}, \alpha)$:

$$\Psi(\mathcal{E}, \alpha) = \iint \Psi_{\mathrm{incident}}(\mathcal{E}_0, \alpha_0)\Psi(\mathcal{E}_0, \alpha_0|\mathcal{E}, \alpha)\, d\mathcal{E}_0\, d\Omega_0.$$

where the above expression is repeated from Equation (3.1). The process of combining

different backscatter distributions is shown graphically in Figure B.1 with panels (a) through (c) corresponding to $\mathcal{E}_0$=0.1, 0.2, and 0.3 MeV, respectively. Formally, this means that

$$\Psi_{\text{incident}}(\mathcal{E}, \alpha) = \delta(\Omega - \Omega_0) \sum_{k=1}^{3} \delta(\mathcal{E} - \mathcal{E}_{0k})$$

with $\mathcal{E}_{01} = 0.1$ MeV, $\mathcal{E}_{02} = 0.2$ MeV, $\mathcal{E}_{03} = 0.3$ MeV, $\Omega = 2\pi(1 - \cos\alpha)$, $\Omega_0 = 2\pi(1 - \cos\alpha_0)$, $\alpha_0 = 70°$. The energy bins are spaced linearly in $x = \mathcal{E}/\mathcal{E}_0 \in [0, 1]$, but the abscissae are displayed in units of keV for easy comparison to the subsequent panels.

As mentioned above, the default sampling grid in backscattered variables $(\mathcal{E}, \alpha)$ for calculating $\Psi_{\mathbf{M}}(\mathcal{E}_0, \alpha_0 | \mathcal{E}, \alpha)$ is always the same and is linearly spaced in solid angle (Ω, as discussed in Section 3.3.1) and in normalized energy ($x = \mathcal{E}/\mathcal{E}_0$, as discussed in Section 3.4.3) so that many distributions can be interpolated simultaneously in a computationally efficient manner. The initial backscatter distribution for each of the three example inputs can then be written $\Psi_0(\mathcal{E}_0, \alpha_0 | \mathcal{E}, \alpha)$, representing the 2-D distribution of backscattered electron fluence sampled on the grid of $\mathcal{E}$, and α.

To combine the three backscatter distributions in panels (a) through (c) into a single $\Psi_{\text{bs}}(\mathcal{E}, \alpha | \mathcal{E}, \alpha)$ requires that each be placed on the same sampling grid. This is accomplished by selecting the grid spanning the largest input (0.3 MeV in this case) and interpolating each backscattered distribution onto the corresponding energy grid: $\Psi_0(\mathcal{E}'_0, \alpha'_0 | \mathcal{E}_{\max}, \alpha)$. As discussed in Appendix A.2 this calculation is most accurate when computed using the CDF of the input function, $\Gamma(\mathcal{E}, \Omega)$, as shown by Equation (A.11).

The result of the downsample interpolation for each respective input is shown in Figure B.1, panels (d) through (f). With all the individual backscatter distributions evaluated on the same grid, the total backscatter distribution, $\Psi_{\text{bs}}(\mathcal{E}_{\text{bs}}, \alpha_{\text{bs}} | \mathcal{E}_{\max}, \alpha)$, is easily calculated as the superposition of the individual $\Psi_0(\mathcal{E}_0, \alpha_0 | \mathcal{E}_{\max}, \alpha)$ distributions. This total backscatter distribution is shown in Figure B.1g with the abscissa corresponding to the maximum energy range (0–0.3 MeV), and the ordinate showing the same pitch angle range of (0°–90°). Equally important is the total deposition, $N_{\text{e,Tot}}(\mathcal{E}, \alpha | h)$, corresponding to the sum of each of the individual $N_{\text{e0}}(\mathcal{E}_0, \alpha_0 | h)$.
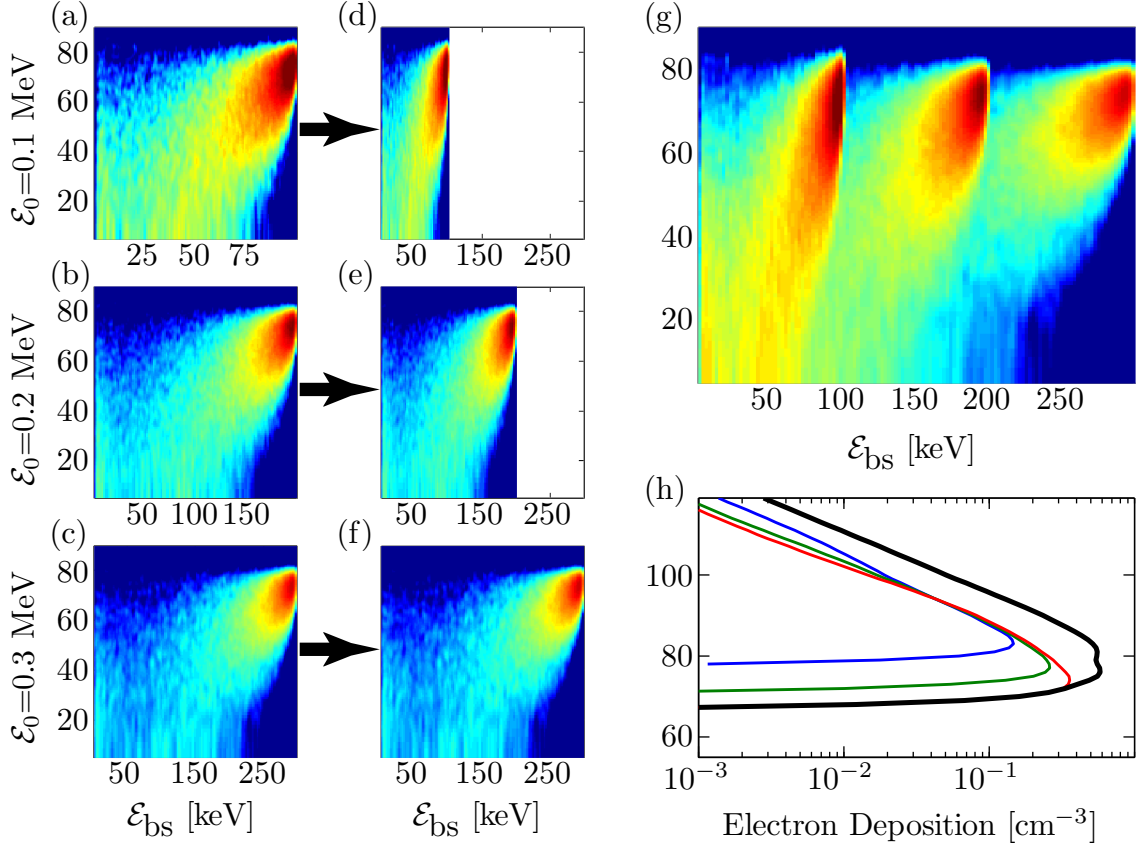
Figure B.1: Hypothetical example with an incident distribution of three monoenergetic beams of electrons: $(\mathcal{E}_0 = 0.1\,\mathrm{MeV}, \alpha_0 = 70°)$, $(\mathcal{E}_0 = 0.2\,\mathrm{MeV}, \alpha_0 = 70°)$, and $(\mathcal{E}_0 = 0.3\,\mathrm{MeV}, \alpha_0 = 70°)$, illustrating the convolution-like process of calculating the backscatter due to any arbitrary input distribution. Panels (a) through (c) show $\Psi^{\mathrm{norm}}(\mathcal{E}_0, \alpha_0 | x, \alpha)$ while panels (d) through (f) show $\Psi_0(\mathcal{E}_0, \alpha_0 | \mathcal{E}_{\max}, \alpha)$. Panel (g) shows the combination of the three distributions shown in panels (d) through (f) on the largest sampling grid $[\mathcal{E}_{\max}, \alpha]$ and panel (h) shows $N_{\mathrm{e}0}(\mathcal{E}_0, \alpha_0 | h)$ as a function of altitude corresponding to each $\Psi^{\mathrm{norm}}(\mathcal{E}_0, \alpha_0 | x, \alpha)$ shown in (a) through (c) as well as the sum of the deposition profiles.

B.2   Generalizing the Backscatter Calculation

Generalizing the above methodology to any arbitrary input distribution is accomplished as follows. Let $\Psi_{\text{in}}(\mathcal{E}_{\text{in}},\ \alpha_{\text{in}}|\mathcal{E},\alpha)$ be the distribution of electrons input into the atmosphere as a function of energy and pitch angle, and evaluated on an arbitrary grid $[\mathcal{E},\ \alpha]$, and let $\Psi_{\text{in}}[i,\ j]$ be the number of electrons (per unit area) contained in the corresponding i^{th} energy, and j^{th} pitch angle bin. Then the backscatter from the atmosphere due to this input is $\Psi_{\text{bs}}(\mathcal{E}_{\text{bs}},\ \alpha_{\text{bs}}|\mathcal{E},\alpha)$, and can be calculated from

$$\Psi_{\text{bs}}(\mathcal{E}_{\text{bs}},\ \alpha_{\text{bs}}|\mathcal{E}_{\text{max}},\alpha) = \sum_{i,j} \Psi_{\text{in}}\,[i,j]\cdot\Psi(\mathcal{E}_i,\ \alpha_j|\mathcal{E}_{\text{max}},\alpha). \tag{B.1}$$

The first step to performing this calculation is identifying and interpolating any input pair $(\mathcal{E}_i,\alpha_j)$ which is not specifically tabulated in $\Psi_{\mathbf{M}}(\mathcal{E}_0,\ \alpha_0|\,\mathcal{E},\alpha)$. Interpolating between the tabulated distributions is accomplished by:

$$\Psi(\mathcal{E}_i,\ \alpha_j|\mathcal{E},\alpha) = \text{INTERP}\left\{[\mathcal{E}_i,\alpha_j], \Psi_0(\mathcal{E}_0,\ \alpha_0|\mathcal{E}\mathcal{E}_0/\mathcal{E}_i,\alpha_j), [\mathcal{E}_i,\alpha_j]\right\} \tag{B.2}$$

as discussed in Equation (A.4).

The final step is to interpolate each of these distributions using the cumulative distribution function as shown in Equation (A.11) and repeated below.

$$\Psi_0(\mathcal{E}_i,\Omega_j|\mathcal{E}_{\text{max}},\Omega) = \text{INTERP}_{DS}\left\{[\mathcal{E}_i,\Omega_j], \Psi_0(\mathcal{E}_i,\Omega_j|\mathcal{E},\Omega), [\mathcal{E}_{\text{max}},\Omega]\right\}. \tag{B.3}$$

The three primary equations detailing the calculation of an arbitrary backscatter distribution are repeated together in Equations (B.4) where the final backscatter distribution in general consists of a different set of energies and pitch angles $(\mathcal{E}_{\text{bs}},\alpha_{\text{bs}})$ than the input $(\mathcal{E}_{\text{in}},\alpha_{\text{in}})$. This is due to the fact that during the atmospheric backscatter

process electrons of new energies and pitch angles are created which are not necessarily part of the incident distribution.

$$\Psi_{\text{bs}}(\mathcal{E}_{\text{bs}},\, \alpha_{\text{bs}}|\mathcal{E}_{\max}, \alpha) \;=\; \sum_{i,j} \Psi_{\text{in}}\,[i,j] \cdot \Psi(\mathcal{E}_i,\, \alpha_j|\mathcal{E}_{\max}, \alpha) \tag{B.4a}$$

$$\Psi(\mathcal{E}_i, \Omega_j|\mathcal{E}_{\max}, \Omega) \;=\; \text{INTERP}_{DS}\,\{[\mathcal{E}_i, \Omega_j], \Psi(\mathcal{E}_i, \Omega_j|\mathcal{E}, \Omega), [\mathcal{E}_{\max}, \Omega]\} \tag{B.4b}$$

$$\Psi(\mathcal{E}_i,\, \alpha_j|\mathcal{E}, \alpha) \;=\; \text{INTERP}\,\{[\mathcal{E}_i, \alpha_j], \Psi_0(\mathcal{E}_0,\, \alpha_0|\mathcal{E}\mathcal{E}_0/\mathcal{E}_i, \alpha_j), [\mathcal{E}_i, \alpha_j]\} \tag{B.4c}$$

Bibliography

Abel, B., and R. M. Thorne (1998a), Electron scattering loss in Earth's inner magnetosphere 1. Dominant physical processes, *J. Geophys. Res.*, *103*, 2385–2396, doi:10.1029/97JA02919.

Abel, B., and R. M. Thorne (1998b), Electron scattering loss in Earth's inner magnetosphere 2. Sensitivity to model parameters, *J. Geophys. Res.*, *103*, 2397–2408, doi:10.1029/97JA02920.

Alexandrov, N. L., E. M. Bezalyan, I. V. Kochetov, and N. A. Dyatko (1997), The ionization kinetics and electric field in the leader channel in long air gaps, *J. Phys. D: Appl. Phys.*, *30*, 1616–1624, doi:10.1088/0022-3727/30/11/011.

Arnold, F., and G. Henschen (1978), First mass analysis of stratospheric negative ions, *Nature*, *275*, 521–522, doi:10.1038/275521a0.

Bainbridge, G., and U. S. Inan (2003), Ionospheric D region electron density profiles derived from the measured interference pattern of VLF waveguide modes, *Radio Science*, *38*, 1077, doi:10.1029/2002RS002686.

Baker, D. N., S. G. Kanekal, X. Li, S. P. Monk, J. Goldstein, and J. L. Burch (2004), An extreme distortion of the Van Allen belt arising from the 'Hallowe'en' solar storm in 2003, *Nature*, *432*, 878–881, doi:10.1038/nature03116.

Banks, P. M., C. R. Chappell, and A. F. Nagy (1974), A new model for the interaction of auroral electrons with the atmosphere: Spectral degradation, backscatter, optical emission, and ionization, *J. Geophys. Res.*, *79*, 1459–1470, doi:10.1029/JA079i010p01459.

Bell, T. F. (1984), The nonlinear gyroresonance interaction between energetic electrons and coherent VLF waves propagating at an arbitrary angle with respect to the Earth's magnetic field, *J. Geophys. Res.*, *89*, 905–918, doi:10.1029/ JA089iA02p00905.

Berger, M., S. Seltzer, and K. Maeda (1974), Some new results on electron transport in the atmosphere, *J. Atmos. Terr. Phys.*, *36*(4), 591–617, doi:10.1016/0021-9169(74) 90085-3.

Bethe, H. A., and J. Ashkin (1953), Passage of radiation through matter, in *Experimental Nuclear Physics*, vol. 1, edited by E. Segr'e, John Wiley, New York.

Blake, J. B., U. S. Inan, M. Walt, T. F. Bell, J. Bortnik, D. L. Chenette, and H. J. Christian (2001), Lightning-induced energetic electron flux enhancements in the drift loss cone, *J. Geophys. Res.*, *106*, 29,733–29,744, doi:10.1029/2001JA000067.

Bortnik, J., U. S. Inan, and T. F. Bell (2006a), Temporal signatures of radiation belt electron precipitation induced by lightning-generated MR whistler waves: 1. Methodology, *J. Geophys. Res., (Space Physics)*, *111*, A02,204–+, doi:10.1029/ 2005JA011182.

Bortnik, J., U. S. Inan, and T. F. Bell (2006b), Temporal signatures of radiation belt electron precipitation induced by lightning-generated MR whistler waves: 2. Global signatures, *J. Geophys. Res., (Space Physics)*, *111*, A02,205–+, doi:10.1029/ 2005JA011398.

Botev, Z. I. (2006), A novel nonparametric density estimator, *Tech. rep.*, The University of Queensland.

Budden, K. G. (1953), The propagation of very low frequency radio waves to great distances, *Philosophical Magazine Series 7*, *44*, 504–513.

Budden, K. G. (1985), *The Propagation of Radio Waves*, Cambridge University Press.

Carpenter, D. L. (1963), Whistler evidence of a 'knee' in the magnetospheric ionization density profile, *J. Geophys. Res.*, *68*, 1675–1682, doi:10.1029/JZ068i006p01675.

Chang, H. C., and U. S. Inan (1983), Quasi-relativistic electron precipitation due to interactions with coherent VLF waves in the magnetosphere, *J. Geophys. Res.*, *88*, 318–328.

Chang, H. C., and U. S. Inan (1985), Lightning-induced electron precipitation from the magnetosphere, *J. Geophys. Res.*, *90*, 1531–1541.

Chevalier, M. W., W. B. Peter, U. S. Inan, T. F. Bell, and M. Spasojevic (2007), Remote sensing of ionospheric disturbances associated with energetic particle precipitation using the south pole VLF beacon, *J. Geophys. Res., (Space Physics)*, *112*, A11,306–+, doi:10.1029/2007JA012425.

Christian, H. J., et al. (2003), Global frequency and distribution of lightning as observed from space by the optical transient detector, *J. Geophys. Res., (Atmospheres)*, *108*, 4005–+, doi:10.1029/2002JD002347.

Cohen, M., U. Inan, and E. Paschal (2010), Sensitive broadband ELF/VLF radio reception with the AWESOME instrument, *IEEE Trans. Geosci. Remote Sensing*, *48*(1), 3 –17, doi:10.1109/TGRS.2009.2028334.

Cummer, S. A. (1997), Lightning and ionospheric remote sensing using VLF/ELF radio atmospherics, Ph.D. Thesis, Stanford University.

Cummer, S. A., and U. S. Inan (2000), Modeling ELF radio atmospheric propagation and extracting lightning currents from ELF observations, *Radio Science*, *35*, 385–394, doi:10.1029/1999RS002184.

Cummer, S. A., U. S. Inan, and T. F. Bell (1998), Ionospheric D region remote sensing using VLF radio atmospherics, *Radio Science*, *33*(6), 1781–1792, doi:10.1029/98RS02381.

Dingle, B., and D. L. Carpenter (1981), Electron precipitation induced by VLF noise bursts at the plasmapause and detected at conjugate ground stations, *J. Geophys. Res.*, *86*, 4597–4606.

Dowden, R., C. Rodger, J. Brundell, and M. Clilverd (2001), Decay of whistler-induced electron precipitation and cloud-ionosphere electrical discharge Trimpis: Observations and analysis, *Radio Science*, *36*, 151–170, doi:10.1029/1999RS002297.

Dowden, R. L., and C. D. D. Adams (1988), Phase and amplitude perturbations on subionospheric signals explained in terms of echoes from lightning-induced electron precipitation ionization patches, *J. Geophys. Res.*, *93*, 11,543–11,550, doi:10.1029/88JA03092.

Dowden, R. L., and C. D. D. Adams (1989), Phase and amplitude perturbations on the NWC signal at Dunedin from lightning-induced electron precipitation, *J. Geophys. Res.*, *94*, 497–503, doi:10.1029/JA094iA01p00497.

Dungey, J. W. (1963), Loss of Van Allen electrons due to whistlers, *Planetary and Space Science*, *11*, 591–595, doi:10.1016/0032-0633(63)90166-1.

Ferguson, E. E. (1979), Ion chemistry of the middle atmosphere, in *Middle Atmosphere Electrodynamics*, edited by N. C. Maynard, pp. 71–88.

Ferguson, J. A., and F. P. Snyder (1987), The segmented waveguide program for long wavelength propagation calculations, *Tech. rep.*, Naval Ocean Systems Center, San Diego, CA.

Fraser-Smith, A. C. (1987), Centered and eccentric geomagnetic dipoles and their poles, 1600–1985, *Reviews of Geophysics*, *25*, 1–16, doi:10.1029/RG025i001p00001.

Gibby, A. R., U. S. Inan, and T. F. Bell (2008), Saturation effects in the VLF-triggered emission process, *J. Geophys. Res., (Space Physics)*, *113*, A11,215, doi:10.1029/2008JA013233.

Glukhov, V. S., V. P. Pasko, and U. S. Inan (1992), Relaxation of transient lower ionospheric disturbances caused by lightning-whistler-induced electron precipitation bursts, *J. Geophys. Res.*, *97*, 16,971–16,979.

Goldberg, R. A., S. A. Curtis, and J. R. Barcus (1987), Detailed spectral structure of magnetospheric electron bursts precipitated by lightning, *J. Geophys. Res.*, *92*, 2505–2513, doi:10.1029/JA092iA03p02505.

Gołkowski, M., U. S. Inan, A. R. Gibby, and M. B. Cohen (2008), Magnetospheric amplification and emission triggering by ELF/VLF waves injected by the 3.6 MW HAARP ionospheric heater, *J. Geophys. Res., (Space Physics)*, *113*, A10,201, doi: 10.1029/2008JA013157.

Gustafsson, G., N. Papitashvili, and V. Papitashvili (1992), A revised corrected geomagnetic coordinate system for epochs 1985 and 1990, *J. Atmos. Terr. Phys.*, *54*(11–12), 1609–1631, doi:10.1016/0021-9169(92)90167-J.

Helliwell, R. (1965), *Whistlers and Related Ionospheric Phenomena*, Stanford Univ. Press, Stanford, California.

Helliwell, R., J. P. Katsufrakis, and M. Trimpi (1973), Whistler-induced amplitude perturbation in VLF propagation, *J. Geophys. Res.*, *78*, 4679–4688.

Herzenberg, A. (1969), Attachment of slow electrons to oxygen molecules, *J. Chem. Phys*, *51*, 4942–4950, doi:10.1063/1.1671887.

Imhof, W. L., et al. (1985), Results from the seep active space plasma experiment - effects on the ionosphere, *Radio Science*, *20*, 511–518, doi:10.1029/RS020i003p00511.

Inan, U. S., and T. F. Bell (1977), The plasmapause as a VLF wave guide, *J. Geophys. Res.*, *82*, 2819–2827.

Inan, U. S., and D. L. Carpenter (1987), Lightning-induced electron precipitation events observed at L of about 2.4 as phase and amplitude perturbations on subionospheric VLF signals, *J. Geophys. Res.*, *92*, 3293–3303.

Inan, U. S., and A. S. Inan (2000), *Electromagnetic Waves*, Prentice Hall.

Inan, U. S., T. F. Bell, and R. A. Helliwell (1978), Nonlinear pitch angle scattering of energetic electrons by coherent VLF waves in the magnetosphere, *J. Geophys. Res.*, *83*, 3235–3253, doi:10.1029/JA083iA07p03235.

Inan, U. S., D. L. Carpenter, R. A. Helliwell, and J. P. Katsufrakis (1985a), Subiono-spheric VLF/LF phase perturbations produced by lightning-whistler induced parti-cle precipitation, *J. Geophys. Res.*, *90*, 7457–7469, doi:10.1029/JA090iA08p07457.

Inan, U. S., H. C. Chang, R. A. Helliwell, W. L. Imhof, J. B. Reagan, and M. Walt (1985b), Precipitation of radiation belt electrons by man-made waves a comparison between theory and measurement, *J. Geophys. Res.*, *90*, 359–369, doi:10.1029/ JA090iA01p00359.

Inan, U. S., D. C. Shafer, W. Y. Yip, and R. E. Orville (1988a), Subionospheric VLF signatures of nighttime D region perturbations in the vicinity of lightning discharges, *J. Geophys. Res.*, *93*, 11,455–11,472.

Inan, U. S., W. C. Burgess, T. G. Wolf, D. C. Shater, and R. E. Orville (1988b), Lightning-associated precipitation of MeV electrons from the inner radiation belt, *Geophys. Res. Lett.*, *15*, 172–175.

Inan, U. S., T. G. Wolf, and D. L. Carpenter (1988c), Geographic distribution of lightning-induced electron precipitation observed as VLF/LF perturbation events, *J. Geophys. Res.*, *93*, 9841–9853.

Inan, U. S., M. Walt, H. D. Voss, and W. L. Imhof (1989), Energy spectra and pitch angle distributions of lightning-induced electron precipitation - analysis of an event observed on the S81-1 (SEEP) satellite, *J. Geophys. Res.*, *94*, 1379–1401.

Inan, U. S., J. V. Rodriguez, S. Lev-Tov, and J. Oh (1992), Ionospheric modifica-tion with a VLF transmitter, *Geophys. Res. Lett.*, *19*, 2071–2074, doi:10.1029/ 92GL02378.

Inan, U. S., S. C. Reising, G. J. Fishman, and J. M. Horack (1996), On the association of terrestrial gamma-ray bursts with lightning and implications for sprites, *Geophys. Res. Lett.*, *23*, 1017–1020, doi:10.1029/96GL00746.

Inan, U. S., N. G. Lehtinen, R. C. Moore, K. Hurley, S. Boggs, D. M. Smith, and G. J. Fishman (2007), Massive disturbance of the daytime lower ionosphere by the giant

γ-ray flare from magnetar SGR 1806-20, *Geophys. Res. Lett.*, *34*(8), 8103–8106, doi:10.1029/2006GL029145.

Jackson, J. D. (1998), *Classical Electrodynamics*, third ed., Wiley.

Johnson, M. P., U. S. Inan, and D. S. Lauben (1999), Subionospheric VLF signatures of oblique (nonducted) whistler-induced precipitation, *Geophys. Res. Lett.*, *26*, 3569–3572, doi:10.1029/1999GL010706.

Kozlov, S. I., V. A. Vlaskov, and N. V. Smirnova (1988), Specialized aeronomic model for investigating artificial modification of the middle atmosphere and lower ionosphere. 1. Requirements of the model and basic concepts of its formation, *Cosmic Res., Engl. Transl.*, *26*, 635642.

Kulkarni, P., U. S. Inan, T. F. Bell, and J. Bortnik (2008), Precipitation signatures of ground-based VLF transmitters, *J. Geophys. Res., (Space Physics)*, *113*, A07,214–+, doi:10.1029/2007JA012569.

Lauben, D. S., U. S. Inan, and T. F. Bell (1999), Poleward-displaced electron precipitation from lightning-generated oblique whistlers, *Geophys. Res. Lett.*, *26*, 2633–2636, doi:10.1029/1999GL900374.

Lauben, D. S., U. S. Inan, and T. F. Bell (2001), Precipitation of radiation belt electrons induced by obliquely propagating lightning-generated whistlers, *J. Geophys. Res.*, *106*, 29,745–29,770, doi:10.1029/1999JA000155.

Lehtinen, N. G. (2000), Relativistic runaway electrons above thunderstorms, Ph.D. Thesis, Stanford University.

Lehtinen, N. G., and U. S. Inan (2007), Possible persistent ionization caused by giant blue jets, *Geophys. Res. Lett.*, *34*, L08,804, doi:10.1029/2006GL029051.

Lehtinen, N. G., and U. S. Inan (2009), Full-wave modeling of transionospheric propagation of VLF waves, *Geophys. Res. Lett.*, *36*, 3104–+, doi:10.1029/2008GL036535.

Lehtinen, N. G., T. F. Bell, and U. S. Inan (1999), Monte Carlo simulation of runaway mev electron breakdown with application to red sprites and terrestrial gamma ray flashes, *J. Geophys. Res.*, *104*, 24,699–24,712, doi:10.1029/1999JA900335.

Lehtinen, N. G., R. A. Marshall, and U. S. Inan (2010), Full-wave modeling of "early" VLF perturbations caused by lightning electromagnetic pulses, *J. Geophys. Res., (Space Physics)*, *115*(A14), A00E40, doi:10.1029/2009JA014776.

Lev-Tov, S. J., U. S. Inan, and T. F. Bell (1995), Altitude profiles of localized *D* region density disturbances produced in lightning-induced electron precipitation events, *J. Geophys. Res.*, *100*, 21,375–21,384, doi:10.1029/95JA01615.

Li, X., et al. (1997), Multisatellite observations of the outer zone electron variation during the November 3-4, 1993, magnetic storm, *J. Geophys. Res.*, *102*, 14,123–14,140, doi:10.1029/97JA01101.

Lyons, L. R., and R. M. Thorne (1973), Equilibrium structure of radiation belt electrons, *J. Geophys. Res.*, *78*, 2142–2149, doi:10.1029/JA078i013p02142.

Marshall, R. A. (2009), Very low frequency radio signatures of transient luminous events above thunderstorms, Ph.D. Thesis, Stanford University.

McIlwain, C. E. (1961), Coordinates for mapping the distribution of magnetically trapped particles, *J. Geophys. Res.*, *66*, 3681–3691, doi:10.1029/JZ066i011p03681.

Mitra, A. P. (1975), D-region in disturbed conditions, including flares and energetic particles, *J. Atmos. Terr. Phys.*, *37*, 895–913, doi:10.1016/0021-9169(75)90005-7.

Mitra, A. P. (1981), Chemistry of middle atmospheric ionization - a review, *J. Atmos. Terr. Phys.*, *43*, 737–752, doi:10.1016/0021-9169(81)90050-7.

Mitra, A. P., and J. N. Rowe (1972), Ionospheric effects of solar flares-VI. Changes in *D*-region ion chemistry during solar flares, *J. Atmos. Terr. Phys.*, *34*, 795–806, doi:10.1016/0021-9169(72)90112-2.

Moore, R. C., C. P. Barrington-Leigh, U. S. Inan, and T. F. Bell (2003), Early/fast VLF events produced by electron density changes associated with sprite halos, *J. Geophys. Res., (Space Physics)*, *108*, 1–1, doi:10.1029/2002JA009816.

Morgan, R. R. (1968), World-wide VLF effective conductivity map, *Tech. Rep. Report 8013F-1*, Westinghouse Electric Corporation Report 8013F-1.

Nagai, T. (1988), "Space weather forecast" - Prediction of relativistic electron intensity at synchronous orbit, *Geophys. Res. Lett.*, *15*, 425–428, doi:10.1029/ GL015i005p00425.

Omura, Y., H. Matsumoto, D. Nunn, and M. J. Rycroft (1991), A review of observational, theoretical and numerical studies of VLF triggered emissions, *J. Atmos. Terr. Phys.*, *53*, 351–368, doi:10.1016/0021-9169(91)90031-2.

Papitashvili, V. O., N. E. Papitashvili, and J. H. King (1997), Magnetospheric geomagnetic coordinates for space physics data presentation and visualization, *Advances in Space Research*, *20*(4-5), 1097–1100.

Pappert, R. A., and F. P. Snyder (1972), Some results of a mode-conversion program for VLF, *Radio Science*, *7*, 913–+, doi:10.1029/RS007i010p00913.

Pasko, V. P., and U. S. Inan (1994), Recovery signatures of lightning-associated VLF perturbations as a measure of the lower ionosphere, *J. Geophys. Res.*, *99*, 17,523–17,538, doi:10.1029/94JA01378.

Pasko, V. P., U. S. Inan, T. F. Bell, and Y. N. Taranenko (1997), Sprites produced by quasi-electrostatic heating and ionization in the lower ionosphere, *J. Geophys. Res.*, *102*, 4529–4562, doi:10.1029/96JA03528.

Peter, B., W. (2007), Quantitative measurement of lighting-induced electron precipitation using VLF remote sensing, Ph.D. Thesis, Stanford University.

Peter, W. B., and U. S. Inan (2004), On the occurrence and spatial extent of electron precipitation induced by oblique nonducted whistler waves, *J. Geophys. Res., (Space Physics)*, *109*, A12,215, doi:10.1029/2004JA010412.

Peter, W. B., and U. S. Inan (2007), A quantitative comparison of lightning-induced electron precipitation and VLF signal perturbations, *J. Geophys. Res., (Space Physics)*, *112*, 12,212–+, doi:10.1029/2006JA012165.

Poulsen, W. L. (1991), Modeling of very low frequency wave propagation and scattering within the Earth-ionosphere waveguide in the presence of lower ionospheric disturbances, Ph.D. Thesis, Stanford University.

Poulsen, W. L., U. S. Inan, and T. F. Bell (1993a), A multiple-mode three-dimensional model of VLF propagation in the Earth-ionosphere waveguide in the presence of localized *D* region disturbances, *J. Geophys. Res.*, *98*, 1705–1717, doi:10.1029/92JA01529.

Poulsen, W. L., T. F. Bell, and U. S. Inan (1993b), The scattering of VLF waves by localized ionospheric disturbances produced by lightning-induced electron precipitation, *J. Geophys. Res.*, *98*, 15,553–+, doi:10.1029/93JA01201.

Rasmussen, J. E., P. A. Kossey, and E. A. Lewis (1980), Evidence of an ionospheric reflecting layer below the classical *D* region, *J. Geophys. Res.*, *85*(A6), 3037–3044.

Ratcliffe, J. A. (1959), *Magneto-Ionic Theory and its Applications to the Ionosphere - A Monograph*, Cambridge University Press.

Rees, M. H. (1963), Auroral ionization and excitation by incident energetic electrons, *Planetary and Space Science*, *11*, 1209–+, doi:10.1016/0032-0633(63)90252-6.

Reid, C. G. (1979), The middle atmosphere, *Tech. rep.*, NASA: Middle Atmosphere Electrodynamics.

Rodger, C. J., O. A. Molchanov, and N. R. Thomson (1998), Relaxation of transient ionization in the lower ionosphere, *J. Geophys. Res.*, *103*, 6969–6976, doi:10.1029/98JA00016.

Rosenberg, T. J., R. A. Helliwell, and J. P. Katsufrakis (1971), Electron precipitation associated with discrete very-low-frequency emissions, *J. Geophys. Res.*, *76*, 8445–8452, doi:10.1029/JA076i034p08445.

Rowe, J. N., A. P. Mitra, A. J. Ferraro, and H. S. Lee (1974), An experimental and theoretical study of the *D*-region - II. A semi-empirical model for mid-latitude *D*-region, *J. Atmos. Terr. Phys.*, *36*(5), 755–785, doi:10.1016/0021-9169(74)90023-3.

Said, R. K., U. S. Inan, and K. L. Cummins (2010), Long-range lightning geo-location using a VLF radio atmospheric waveform bank, *J. Geophys. Res., (Atmospheres)*, *115*, D23,108, doi:10.1029/2010JD013863.

Salby, M. L. (1996), *Fundamentals of atmospheric physics*, Academic Press Inc.

Selesnick, R. S., J. B. Blake, and R. A. Mewaldt (2003), Atmospheric losses of radiation belt electrons, *J. Geophys. Res., (Space Physics)*, *108*, 1468–+, doi:10.1029/2003JA010160.

Sheather, S. J., and M. C. Jones (1991), A reliable data-based bandwidth selection method for kernel density estimation, *J. Royy Stat. Soc. Series B (Methodological)*, *53*(3), 683–690.

Stadsness, J., and B. Maehlum (1965), Scattering and absorption of fast electrons in the upper atmosphere, *Tech. rep.*, Forsvarets Forskningsinstitutt, Norwegian Defense Research Establishment.

Storey, L. R. O. (1953), An investigation of whistling atmospherics, *Phil. Trans. R. Soc. A*, *246*, 113–141.

Tarcsai, G., P. Szemerdy, and L. Hegymegi (1988), Average electron density profiles in the plasmasphere between $L = 1.4$ and 3.2 deduced from whistlers, *J. Atmos. Terr. Phys.*, *50*(7), 607 – 611, doi:10.1016/0021-9169(88)90058-X.

Tascione, T. F. (1988), *Introduction to the space environment.*, Krieger Publishing Company, Malabar, Florida.

Thorne, R. M., and C. F. Kennel (1971), Relativistic electron precipitation during magnetic storm main phase., *J. Geophys. Res.*, *76*, 4446–4453, doi:10.1029/JA076i019p04446.

Turunen, E., H. Matveinen, J. Tolvanen, and Ranta (1996), *D-Region Ion Chemistry Model*, chap. 1, pp. 1–25, STEP Handbook of Ionospheric Models, SCOSTEP Secretariat, Boulder, Colorado, USA,1996.

Van Allen, J. A., C. E. McIlwain, and G. H. Ludwig (1959), Radiation observations with satellite 1958ε, *J. Geophys. Res.*, *64*, 271–286, doi:10.1029/JZ064i003p00271.

Verronen, P. T., E. Turunen, T. Ulich, and E. Kyrl (2002), Modelling the effects of the October 1989 solar proton event on mesospheric odd nitrogen using a detailed ion and neutral chemistry model, *Annales Geophysicae*, *20*(12), 1967–1976, doi: 10.5194/angeo-20-1967-2002.

Vette, J. I. (1991), The AE-8 trapped electron model environment, *NASA STI/Recon Technical Report N*, *92*, 24,228–+.

Voss, H. D., et al. (1984), Lightning-induced electron precipitation, *Nature*, *312*, 740–742, doi:10.1038/312740a0.

Voss, H. D., M. Walt, W. L. Imhof, J. Mobilia, and U. S. Inan (1998), Satellite observations of lightning-induced electron precipitation, *J. Geophys. Res.*, *103*, 11,725–11,744, doi:10.1029/97JA02878.

Walt, M. (2005), *Introduction to Geomagnetically Trapped Radiation*, Cambridge University Press.

Webb, D., and J. Allen (2004), Spacecraft and ground anomalies related to the October-November 2003 solar activity, *Space Weather*, *2*, S03,008, doi:10.1029/2004SW000075.

Wedde, T. (1971), Effect of the auroral electrojet on the scattering and absorption of fast electrons in the upper atmosphere, *J. Atmos. Terr. Phys.*, *33*, 547–+.

Wolf, T. G., and U. S. Inan (1990), Path-dependent properties of subionospheric VLF amplitude and phase perturbations associated with lightning, *J. Geophys. Res.*, *95*, 20,997–21,005, doi:10.1029/JA095iA12p20997.

Wulff, A., and J. A. Gledhill (1974), Atmospheric ionization by precipitated electrons, *J. Atmos. Terr. Phys.*, *36*(1), 79–91, doi:10.1016/0021-9169(74)90068-3.